OPTICAL PROPERTIES OF SOLID THIN FILMS BY SPECTROSCOPIC REFLECTOMETRY AND SPECTROSCOPIC ELLIPSOMETRY

by

DIONNE A. MILLER

A dissertation submitted to the Graduate Faculty in Chemistry in partial fulfillment of the requirements for the degree of Doctor of Philosophy, The City University of New York

2008

UMI Number: 3310748

Copyright 2008 by
Miller, Dionne A.

All rights reserved

INFORMATION TO USERS

The quality of this reproduction is dependent upon the quality of the copy submitted. Broken or indistinct print, colored or poor quality illustrations and photographs, print bleed-through, substandard margins, and improper alignment can adversely affect reproduction.

In the unlikely event that the author did not send a complete manuscript and there are missing pages, these will be noted. Also, if unauthorized copyright material had to be removed, a note will indicate the deletion.

UMI®

UMI Microform 3310748
Copyright 2008 by ProQuest LLC
All rights reserved. This microform edition is protected against unauthorized copying under Title 17, United States Code.

ProQuest LLC
789 East Eisenhower Parkway
P.O. Box 1346
Ann Arbor, MI 48106-1346

© 2008

DIONNE A. MILLER

All Rights Reserved

This manuscript has been read and accepted for the
Graduate Faculty in Chemistry in satisfaction of the
dissertation requirement for the degree of Doctor of Philosophy.

Dr. Daniel L. Akins

Date

Chair of Examining Committee

Dr. Glen R. Kowach

Date

Co-Chair of Examining Committee

Dr. Gerald Koeppl

Date

Executive Officer

Dr. Maria Tamargo

Dr. Chwen-Yang Shew

Supervisory Committee

THE CITY UNIVERSITY OF NEW YORK

ABSTRACT

OPTICAL PROPERTIES OF SOLID THIN FILMS BY REFLECTOMETRY
AND SPECTROSCOPIC ELLIPSOMETRY

by

Dionne A. Miller

Advisers: Professor Glen R. Kowach
Professor Daniel L. Akins

The intense focus on the development of practical optoelectronic and photonic devices demands accurate characterization of the optical properties of the materials of interest. Some of these materials include zinc oxide (ZnO), strontium titanate (STO) and gold nanoparticles. It is envisioned that these materials will be best utilized in thin film technology. Spectroscopic reflectometry (SR) and spectroscopic ellipsometry (SE) are uniquely powerful tools for accurately characterizing the optical properties, structure and thicknesses of thin films. Combining both techniques in one measurement offers many advantages, not the least of which is reduced systematic errors from the simultaneous analysis of multiple data sets.

We report for the first time, the use of SR and SE concurrently (SRSE), to successfully develop optical models, and determine the variation in refractive index, n and extinction coefficient, k above and below the band edge of ZnO, for thin films deposited on silicon and platinum substrates at various deposition temperatures. For the

first time, a graded layer model is used to model the surface roughness layers to give extremely accurate fits to the data on Pt substrates.

We also report the development of an optical model based on reflectometry data, for STO films deposited on silicon and platinum at various substrate temperatures. The analysis reveals an index gradient in STO deposited on silicon and no interface layer as reported in other publications. Finally, we were able to successfully model, using SRSE data, the optical properties of molecularly mediated, self-assembled gold nanoparticle thin films. The analysis reveals that *n* and *k* increase with the thickness of the thin films with the same linking molecule and that for similarly sized Au nanoparticles, the decrease in the chain length of the linker molecules results in higher values of *n* and *k*.

Dedicated in loving memory of

Hermine Naomi Robinson

1938 - 2004

ACKNOWLEDGEMENTS

It has been a long road. But as the writer of Ecclesiastes says "Two are better than one... If the one falls, the other will lift up his companion." God has richly blessed me with companions to share the journey with, and so now it is incumbent on me to thank the many persons who have helped me to arrive successfully at my destination.

I first must thank my mother, to whom this manuscript is dedicated. Unfortunately, she was not able to see me complete the doctorate but I know that up in heaven, she is smiling and proud of me. I thank her for instilling in me a love of books, a love of learning and love of knowledge.

To the one my heart loves: my husband Fitzroy, whose love, support and patience approaches saintly proportions. Never has a woman felt more loved and supported.

I would like to thank my family, whose relentless encouragement and faith in me never waned even when I doubted myself. So to my brother Maurice, my sister Angela, my nieces Kerese and Kalisia (who could never quite understand an adult being in school), thank you from the bottom of my heart for your love and support.

I am grateful for my friends in New York – Glen Brown, Dominique Jenkins, Daniel Kirk-Foster, Patrick Mattis, Larry Spain – who made sure I acclimatized and felt at home in a big city. Thank you – your friendship has been a great joy and blessing to me.

To my friends and church family at the Church of Reconciliation in Jamaica and St Nicholas of Tolentine in the Bronx: you have helped me mourn and helped me celebrate and you will always have a special place in my heart.

No one quite understands your journey like the man who has walked a mile in your shoes. To Fleumingue Jean-Mary, Philippe Mercier, and Amanda Pustam, fellow graduate students who have also successfully completed the program, I owe a great debt. We have encouraged, motivated, scolded and generally been a huge support system for each other. I know your futures will be filled with even greater achievements. Chun-Min Feng and Julieth Ballesteros, members of the Kowach research group, have been incredibly generous with their friendship and in helping me to fit in seamlessly into the Kowach research group. Thank you, Chun-Min, for all the afternoon coffee and all the lunch orders. Thank you Julieth for spoiling me rotten at every opportunity – bringing me lunch, little treats and in general, doing everything you could to make life pleasant. My best wishes to both of you as you complete your respective graduate programs.

My thanks also go to Mrs. Sandra Smith, the former administrative assistant of CASI and Ms. Diane Beckford, the current CASI administrator for all they have done to support the work of the graduate students in the CASI program. A big thank you also goes to Mrs. Diane Adebowale, the administrator of the Chemistry program at the Graduate Center – without her, I am sure we would all grind to a halt.

My thanks to Prof. Gerald Koeppl, the Executive Officer of the Chemistry Program at the Graduate Center who does a marvelous job and is so very attuned to the needs of the students in the program. Thank you for all your advice, fatherly wisdom and concern.

I am indebted to Prof. Maria Tamargo and Prof. Chwen-Yang Shew, members of my thesis committee. They have always been a source of encouragement, insightful comments and guidance. Thank you to Prof. Shew who was always the first to respond

to emails and the first to arrive for meetings, often half an hour early, undertaking the long journey from Staten Island to City College without murmur.

My thanks also go to Prof. Daniel L. Akins, who gave me the opportunity to study at CUNY and supported me through most of my graduate studies. Your message of academic independence is not lost on me.

And lastly, to Prof. Glen R. Kowach, with whom I worked for the final two years of the program on the work presented in this manuscript, thank you is woefully inadequate. I was privileged to work with you and to learn from you and to have your unwavering support and encouragement of my efforts. Your enthusiasm for your work and your students certainly made the lab a supportive and fun place to be and I know without your input, this final step might never have happened.

TABLE OF CONTENTS

ABSTRACT iv

ACKNOWLEDGEMENTS vii

TABLE OF CONTENTS x

LIST OF TABLES xiv

LIST OF FIGURES xv

Chapter 1 Optical Properties of Materials 1

1.1 Introduction 1

1.2 Interaction of Light with Matter 2

1.3 Optical Processes: Reflection and Refraction 3

1.4 The Optical Constants 6

1.5 Survey of the Theory of Optical Properties 11

1.6 Optical Spectra of Materials 21

1.7 Optical Properties of Solid Thin Films 27

Chapter 1 References 32

Chapter 2 Synthesis, Structure and Fabrication of Thin Films 33

2.1 Introduction 33

2.2 Thin Film Growth Processes 33

2.3 Physical Structure of Thin Films 35

2.4 Thin Film Technology 39

Chapter 2 References 47

Chapter 3 Reflectometry and Ellipsometry 48

3.1 Introduction 48

3.2 Applications of Reflectometry and Spectroscopic Ellipsometry 49

3.3 Principles of Reflectometry and Spectroscopic Ellipsometry 51

3.4 Data Analysis 54

Chapter 3 References 58

Chapter 4 Optical Properties of Zinc Oxide Thin Films 59

4.1 Introduction 59

4.2 Structure and Properties of Zinc Oxide 61

4.3 Experimental 63

4.4 Results 65

4.4.1 Reflectometry and Ellipsometry Data 66

4.4.2 Atomic Force Microscopy (AFM) Data 72

4.4.3 Scanning Electron Microscopy (SEM) Data 75

4.5 Discussion 76

4.6 Conclusions 91

Chapter 4 References 92

Chapter 5 Optical Properties of Strontium Titanate Thin Films 97

5.1 Introduction 97

5.2 Structure and Properties of Strontium Titanate 98

5.3 Experimental 100

5.4 Results 102

5.4.1 Description of Optical Model 102

5.4.2 Reflectometry Data 103

5.4.3 X-Ray Diffraction (XRD) 110

5.5 Discussion 112

5.6 Conclusions 119

Chapter 5 References 120

Chapter 6 Assessment of Morphological and Optical Properties of Molecularly Mediated Thin Film Assembly of Gold Nanoparticles 122

6.1 Abstract 122

6.2 Introduction 123

6.3 Experimental 125

6.4 Results and Discussion 129

6.4.1 Morphological Properties 129

6.4.2 Optical Properties 135

6.5 Conclusion 144

Chapter 6 References 146

Appendix A 149

Appendix B 169

Bibliography 193

LIST OF TABLES

Table 4.1	Regression Parameter Data and Optical Constants for Figure 4.4	69
Table 4.2	Summary of Results for ZnO Thin Films on Silicon Substrate	69
Table 4.3	Regression Parameter Data and Optical Constants for Figure 4.4	71
Table 4.4	Summary of Results for ZnO Thin Films on Platinum Substrate	71
Table 4.5	Comparison of RMSE for Various Optical Models of ZnO	72
Table 4.6	Roughness Analysis of AFM Data of ZnO Thin Films on Platinum	74
Table 4.7	Summary of Previous Studies on the Optical Properties of ZnO Single Crystals and Thin Films	84
Table 5.1	Regression Parameter Data and Optical Constants for Figure 5.2	105
Table 5.2	Summary of Results for STO Thin Films on Silicon Substrate	106
Table 5.3	Regression Parameter Data and Optical Constants for Figure 5.3	108
Table 5.4	Summary of Results for STO Thin Films on Platinum Substrate	109
Table 6.1	XRD Results of Thin Film Assemblies of Au Nanoparticles	132
Table 6.2	Comparison of *d*-spacing Values for Thin Film Assemblies of Au Nanoparticles	135
Table 6.3	Optical Constants of NDT- and PDT-Au 2 nm Thin Film Assemblies	141

LIST OF FIGURES

Figure 1.1	Reflection and Refraction of Light at an Interface	4
Figure 1.2	Frequency Dependency of the Reflectivity of Metals in the Infrared Spectral Region	12
Figure 1.3	Frequency Dependency of the Reflectivity of Metals in the Visible Spectral Region	13
Figure 1.4	Frequency Dependency of the Dielectric Constant according to the Lorentz Approach	14
Figure 1.5	One Dimensional Periodic Potential According to Kronig-Penny Model	16
Figure 1.6	Energy Bands in Solids	18
Figure 1.7	Energy Diagram showing Direct Interband Transitions	19
Figure 1.8	Optical Functions for a Typical Insulator	23
Figure 1.9	Optical Functions for a Typical Semiconductor	25
Figure 1.10	Optical Functions for a Typical Metal	26
Figure 1.11	Light Interacting with a Film on a Substrate	28
Figure 1.12	Comparison of Reflectance of Thinner vs. Thicker Films	30
Figure 3.1	Measurement Principle of Ellipsometry	53
Figure 3.2	Optical Configuration of Rotating Compensator Ellipsometer	53
Figure 3.3	Data Analysis Flowchart for SRSE	57
Figure 4.1	Structure of Zinc Oxide	61
Figure 4.2	Schematic of the Anelva SPF-332H sputtering system	64
Figure 4.3A	Optical Model for the Analysis of ZnO Thin Films	65
Figure 4.3B	Optical Model for the Analysis of the EMA layer of ZnO Thin Films	66
Figure 4.4	Sample Reflectance and Ellipsometry Spectra and Data for	67

	ZnO Thin Films on Silicon Substrate	
Figure 4.5	Sample Reflectance and Ellipsometry Spectra and Data for ZnO Thin Films on Platinum Substrate	70
Figure 4.6	AFM Images of ZnO Thin Films on Platinum Substrate	73
Figure 4.7	SEM Images of ZnO Thin Films on Platinum Substrate	75
Figure 4.8	Refractive Index and EMA Layer Thickness vs. Deposition Temperature for ZnO Films on Silicon Substrate	77
Figure 4.9	Refractive Index and EMA Layer Thickness vs. Deposition Temperature for ZnO Films on Platinum Substrate	78
Figure 4.10	AFM Roughness Average vs. Deposition Temperature for ZnO Films on Platinum Substrate	80
Figure 4.11	The Optical Indicatrix for a Positive Uniaxial Crystal	88
Figure 4.12	Comparison of Refractive Index vs. Deposition Temperature for ZnO Thin Films on Silicon and Platinum Substrates	90
Figure 5.1	Crystal Structure of Strontium Titanate	99
Figure 5.2	Sample Reflectance Spectra and Data for STO Thin Films on Silicon Substrate	104
Figure 5.3	Sample Reflectance Spectra and Data for STO Thin Films on Platinum Substrate	107
Figure 5.4	Comparison of X-Ray Diffraction Spectra for STO on Silicon Substrate at Two Different Deposition Temperatures	110
Figure 5.5	Comparison of X-Ray Diffraction Spectra for STO on Silicon Substrate and Platinum Substrate at the same Deposition Temperature	111
Figure 5.6	Comparison of Optical Constant Dispersion of STO Single Crystal and Thin Film	113
Figure 5.7	Refractive Index vs. Substrate Deposition Temperature for STO Thin Films on Silicon Substrate	115
Figure 5.8	Refractive Index vs. Substrate Deposition Temperature for STO Thin Films on Silicon and Platinum Substrate	116

Figure 5.9	Schematic of STO on Silicon Film Structure	117
Figure 6.1	AFM Images of Au Nanoparticle Films on Various Substrates	131
Figure 6.2	Small Angle XRD Data for Various Thin Film Assemblies of Au Nanoparticles	129
Figure 6.3	TEM of MUA-Au 6 nm Thin Film Assembly	133
Figure 6.4	UV-Vis Spectra of Thin Film Assemblies of Au Nanoparticles of Various Sizes on Glass Substrates	136
Figure 6.5	Plot of Surface Plasmon Band vs. Chain Length for Thin Films of Different Particle Sizes	137
Figure 6.6	Simulation of SP Band for Thin Film Assemblies of Au Nanoparticles	138
Figure 6.7	Simulation of SP Band for Thin Film Assemblies of ADT-Au Nanoparticles	139
Figure 6.8	Optical Constants of NDT- and PDT-Au 2nm Thin Films	142
Figure 6.9	Optical Constant Dispersion Spectra for MUA-Au 6 nm Thin Film	143

CHAPTER 1: Optical Properties of Materials

1.1. Introduction

In recent years, there has been an immense focus on the development of practical optoelectronic and photonic devices to replace conventional silicon-based electronics. The driving force for this research effort is of course the need to reduce dependence on fossil fuel based energy. Critical to this effort is an accurate characterization of the optical properties of the materials being investigated as alternatives. Spectroscopic reflectometry and spectroscopic ellipsometry (SRSE) are optical techniques that use light to elucidate the optical constants, thickness and structure of thin film materials. They offer unique advantages individually and more so when employed concurrently, in the analysis of such materials.

In this study, the optical properties of zinc oxide, strontium titanate and molecularly mediated, self-assembled gold nanoparticle thin films are determined using SRSE. These materials are all of interest in optoelectronic device applications. The study therefore begins with a brief review of the interaction of light with matter, the nature of the optical constants and the optics of thin film materials. Chapter 2 reviews thin film technology, while chapter 3 introduces the principles and instrumentation of SRSE. Chapters 4, 5 and 6 examine in detail the analysis by SRSE of zinc oxide, strontium titanate and gold nanoparticle thin films, respectively.

1.2. The Interaction of Light with Matter

When light interacts with matter, several processes are possible. These include the absorption and emission of photons and several phenomena related to light scattering such as reflection, refraction and diffraction. Light scattering may be thought of as the redirection of light that takes place when an electromagnetic wave encounters an obstacle (the scattering particle), and occurs when the energy of the incident photon is too small to cause a transition to a higher energy excited state. Instead, the electromagnetic field of the radiation causes the electron cloud to oscillate with respect to the positive nucleus. This perturbation of the electron cloud results in a periodic separation of charge in the molecule called an induced dipole moment. This oscillating induced dipole moment manifests as a source of electromagnetic radiation, thereby resulting in scattered light. The majority of the scattered light is emitted at the same frequency as the incident radiation: this is termed elastic scattering. If the frequency of the scattered light is different from that of the incident radiation then an inelastic scattering event has occurred: this is termed Raman scattering. This interpretation of the light scattering event is based on the model of Lorentz (1878), which treats the atom as a dipole oscillator.[1-3]

Formal light scattering theory may be categorized in terms of two theoretical frameworks. The first, Rayleigh scattering, is applicable to small, dielectric, spherical particles whose size is much smaller than the wavelength of the incident radiation. This corresponds to the assumption that the particle is sufficiently small that it encounters a uniform electric field at any moment so that the time of penetration of the electric field is much less than the frequency of the

electromagnetic wave. The second approach is the theory of Mie scattering (after Gustav Mie) which encompasses the general spherical scattering solution (absorbing or non-absorbing particle) with no bound on particle size. Since Mie scattering theory has no size limitations, it may be used for describing most spherical particle scattering systems, including Rayleigh scattering and converges to the limit of geometric optics for large particles.[3]

1.3. Optical Processes: Reflection and Refraction

Reflection is the change in direction of a wavefront at an interface between two dissimilar media, so that the wavefront returns to the medium in which it originated. The direction of the incident and reflected rays at a smooth interface between two optical materials can be described in terms of the angles they make with the normal to the surface at the point of incidence as shown in Figure 1. If the interface is rough, light is scattered in various directions and there is no single angle of reflection; this is termed diffuse reflection. If the surface is very smooth, light will be reflected at a definite angle: this is called specular reflection.

Refraction occurs when light incident at an interface between two optical materials is transmitted into the second material. When light is incident on an interface it is generally partly reflected and partly refracted (see Figure 1). Refraction causes the ray to be bent away from or towards the normal: this is due to the difference in the speed of the wave in both materials. An important parameter therefore is the index of refraction n of an optical material. It is defined

as the ratio of the speed of light c in a vacuum to the speed of light ν in the material:

$$n = c/\nu \quad (1.1)$$

The value of n depends not only on the material but also on the wavelength of the light[1]. The index of refraction is a very important optical constant and will be discussed in further detail.

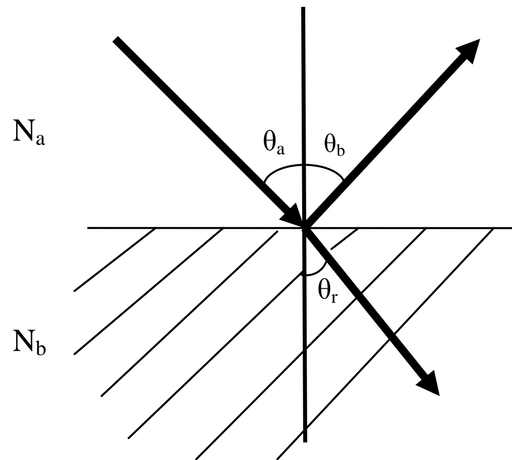

Figure 1.1: Light interacting with a plane parallel interface between two materials with complex index of refraction N_a and N_b.

Several defined relationships exist between the incident, reflected and refracted rays at a smooth interface between two optical materials. Firstly, the incident, reflected and refracted rays and the normal to the surface all lie in the same plane. The plane of these three rays is always perpendicular to the plane of the boundary surface between the two materials. Secondly, the angle of reflection is equal to the angle of incidence for all wavelengths and for any pair of materials. This is generally expressed as:

$$\theta_b = \theta_a \qquad \text{(Law of reflection)} \qquad (1.2)$$

where θ_b and θ_a are the angle of reflection and angle of incidence, respectively. The third relationship is known as the law of refraction. It states that for monochromatic light and for a given pair of materials, *a* and *b* on opposite sides of an interface, the ratio of the sines of the angles θ_a and θ_b, where both angles are measured from the normal to the surface, is equal to the inverse ratio of the two indices of refraction:

$$n_a \sin \theta_a = n_b \sin \theta_b \quad \text{(Law of refraction or Snell's Law)} \quad (1.3)$$

Even though the laws of reflection and refraction can be obtained as an empirical result, they can also be derived from Maxwell's equations using a wave model.

The reflectance (R) is the ratio of the intensity of the outgoing light to the incoming light. Since intensity is proportional to the square of the amplitude of the wave, reflectance can be defined based on amplitude ratios. When only one interface is considered, this ratio is called the Fresnel reflection coefficient and is different for waves whose electric vector lies parallel (*p*-waves) and perpendicular (*s*-waves) to the plane of incidence. The coefficients are as follows:

$$r_p = \frac{n_b \cos\theta_a - n_a \cos\theta_r}{n_b \cos\theta_a + n_a \cos\theta_r} \qquad r_s = \frac{n_a \cos\theta_a - n_b \cos\theta_r}{n_a \cos\theta_a + n_b \cos\theta_r} \quad (1.4)$$

where n_a and n_b are the refractive indices of the first and second media respectively, θ_a is the angle of incidence the beam makes to the normal and θ_r is the angle of refraction in the second medium. A similar pair of ratios can be written for the transmission to incident amplitudes.

For a single interface, the reflectance is the square of the Fresnel reflection coefficients. At the angle of incidence where $r_p = 0$, the reflectance R_p is also zero and all of the reflected light is polarized perpendicular to the plane of incidence

(*s*-polarized). The angle of incidence at which this occurs is called the Brewster angle. The transmitted light still has components of both polarizations.

1.4. The Optical Constants

The optical constants are in fact far from constant: the index of refraction, the extinction coefficient and the dielectric function all depend on wavelength as well as temperature. Therefore, in the spectroscopic range that includes the ultraviolet, visible and infrared light, and if metals, semiconductors and dielectrics are included, the spectra of the optical constants are quite complex. It is this complexity and variation that allows techniques such as ellipsometry and reflectometry to be successful.[4]

1.4.1. Index of Refraction, *n*

As mentioned in the previous section, when light is incident on an interface between two optical materials, some of the light is transmitted into the second medium, or refracted. Starting from the Maxwell equations, it is possible to derive the electromagnetic wave equation that describes the propagation of light in a medium (see references 4 and 5). If the discussion is limited to a plane polarized wave that propagates in the positive *z*-direction and vibrates in the *x*-direction, the equation has the form

$$c^2 \frac{\partial^2 E_x}{\partial z^2} = \varepsilon \frac{\partial^2 E_x}{\partial t^2} + 4\pi\sigma \frac{\partial E_x}{\partial t}, \tag{1.5}$$

where E_x is the *x*-component of the electric field strength, ε is the dielectric constant and σ is the conductivity. The solution to this equation yields

$$\tilde{N}^2 = \varepsilon - \frac{4\pi\sigma}{\omega} i = \varepsilon - \frac{2\sigma}{v} i \qquad (1.6)$$

where $\tilde{N}$ represents the index of refraction and is seen to be a complex quantity and $\omega = 2\pi\nu$ is the angular frequency. Since all complex quantities have a real and imaginary part, $\tilde{N}$ can be written as

$$\tilde{N} = n - ik \qquad (1.7)$$

where n is the real index of refraction, k is the imaginary part of the index of refraction, usually called the extinction coefficient and i is the imaginary number. The index of refraction (n) is an inverse measure of the phase velocity of light in the material, related to the speed of light in free space according to

$$n = \mathrm{c/v}$$

where c is the speed of light. When a wave passes from material "a" to material "b" having a larger index of refraction ($n_b > n_a$), the wave slows down and the angle of refraction will be smaller than the angle of incidence; hence the ray is bent toward the normal. If $n_a > n_b$ then the wave moves faster through the second material and the angle of refraction is greater than the angle of incidence; hence the ray is bent away from the normal.[4,5]

The magnitude of the refractive index depends on the wavelength of the incident light: this property is called dispersion. Historically, the dispersive power of a material was the difference in the index of refraction for the extreme violet ray and the extreme red ray. In metals, the index of refraction varies in addition with the angle of incidence. This is especially true when n is small. Therefore, when

light passes from a vacuum into a medium, its velocity as well as its wavelength decrease in order to keep the frequency, and thus the energy, constant.[4, 5]

1.4.2. Extinction Coefficient, *k*

The extinction coefficient k is a measure of how rapidly the intensity decreases as the light passes through the material. For this reason, k is sometimes called the damping constant. In an absorbing medium, the decrease in intensity I per unit length z is given by

$$\frac{dI(z)}{dz} = -\alpha I(z) \tag{1.8}$$

where α is the absorption coefficient. The solution to this equation is

$$I(z) = I_0 e^{-\alpha z} \tag{1.9}$$

where I_0 is the intensity of light just inside the material of interest and α is dependent on the loss of intensity due to absorption only. The extinction coefficient is related to the absorption coefficient by

$$k = \frac{\lambda}{4\pi}\alpha \tag{1.10}$$

The curve defined by equation (1.9) approaches zero but never gets there and is characterized by a quantity called the "penetration depth". When the quantity αz is equal to 1.0, the intensity will have decreased by a factor of e^{-1} or about 37% of its original value. The penetration depth is defined as the depth at which this occurs and is denoted D_p.[4] It is given by

$$D_p = \frac{\lambda}{4\pi k} \tag{1.11}$$

1.4.3. Dielectric Function, ε

When an electromagnetic wave with field strength E interacts with an atom or molecule that is part of a material, the local field strength at the atom or molecule is different from the field strength in free space because of interactions that occur at the molecular level. This difference is a material property that can be understood in terms of the dipole moment, atomic polarizability, macroscopic polarization and the displacement.

The dipole moment p can be defined by

$$\overline{p} = e\overline{r} \tag{1.12}$$

where e is the electronic charge. If the displacement is sufficiently small, it can be assumed that a linear relationship exists between the dipole moment and the field. This relationship can be expressed as

$$\overline{p} = \overline{\alpha}(\omega)\overline{E} \tag{1.13}$$

where $\overline{\alpha}(\omega)$ is defined as the frequency dependent atomic polarizability. The microscopic field at the location of the atom or molecule is called the displacement field $\overline{D}$ and is given by

$$\overline{D} = \overline{E} + 4\pi\overline{P} \tag{1.14}$$

where $\overline{P}$ is called the macroscopic polarization. Therefore, the displacement field is made up of the external field plus the additional contribution induced by the interaction of the external field with the bulk material. Since $\overline{P}$ is also a function of $\overline{E}$, we can rewrite equation (1.14) as

$$\overline{D} = \overline{E} + 4\pi N\tilde{\alpha}\overline{E} = (1 + 4\pi N\tilde{\alpha})\overline{E} \tag{1.15}$$

In this expression, *N* is the number of oscillators per unit volume and the quantity inside the parentheses is defined as the dielectric function, $\tilde{\varepsilon}$. It represents the degree to which the material may be polarized by an applied external electric field and is itself a complex quantity. It is related to the complex index of refraction by the relationship

$$\tilde{\varepsilon} = \tilde{N}^2 \tag{1.16}$$

and as a complex quantity can also be expressed as

$$\tilde{\varepsilon} = \varepsilon_1 + i\varepsilon_2 \tag{1.17}$$

The real and imaginary part of the dielectric function can be expressed in terms of *n* and *k*:

$$\varepsilon_1 = n^2 - k^2 \tag{1.18}$$

$$\varepsilon_2 = 2nk \tag{1.19}$$

ε_1 is the polarization and ε_2 is the absorption (sometimes called the absorption product) of the material.

Thus the dielectric constant is another parameter that can be used to describe the optical properties of a material.[4]

1.5. Survey of the Theory of Optical Properties

1.5.1. Classical Treatment

In the classical domain, the optical constants and their relationship to electrical constants can be obtained by employing the continuum theory, that is, by considering only macroscopic quantities and empirical data. The validity of the equations derived by this manner holds in the far infrared region but begins to break down at higher frequencies. As an example, the experimentally observed reflectivity of metals decreases faster than would be predicted by the well-known Hagen-Rubens equation. Thus it became apparent that the atomic structure of metals needed to be taken into account in order to explain the optical properties of metals.[5]

1.5.1.1. *Drude Formulation: Free Electron Model*

In the early 20th century, Drude postulated that the valence electrons of a metal can be considered free, that is, they could move independently of their respective nuclei. Further, he assumed that these delocalized electrons could be accelerated by an applied external electric field such as light. The free electrons were thus thought to perform periodic motions or oscillations in the alternating electric field of the light. The model was further refined by considering the electron motion as being restrained by collisions with the atoms of a non-ideal lattice. Using the equations for vibrations with a damping term to take into account the interaction of the electrons with the atoms of the lattice, the frequency dependence of the optical constants can be calculated. The Drude theory correctly reproduces the empirical findings of the dependence of spectral reflectivity on

frequency up to the visible region of the spectrum. By contrast, the Hagen-Rubens relation is correct only up to 10^{13} s^{-1} (i.e., classical infrared absorption). A schematic representation of the frequency dependency of the reflectivity for metals and dielectrics as determined by experiment and according to the Hagen-Rubens and Drude models is shown in Figure 1.2.[5]

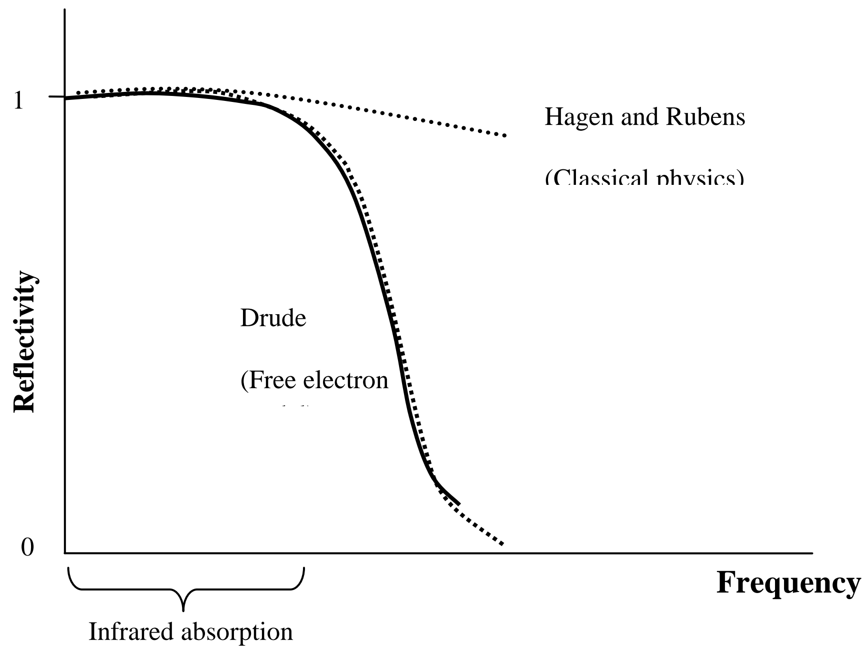

Figure 1.2: Frequency dependence of the reflectivity of metals experimentally (solid line) and according to Hagen and Rubens model and Drude free electron model (dotted lines).

1.5.1.2. *The Lorentz Model*

In the violet to ultraviolet region of the spectrum of metals, an absorption band appears in the reflectivity spectrum (see Figure 1.3) that cannot be explained by the Drude formulation. To interpret the absorption bands that occurred in the reflectivity spectra at higher frequencies, Lorentz postulated that the electrons are in fact bound to their respective nuclei. Under the influence of an

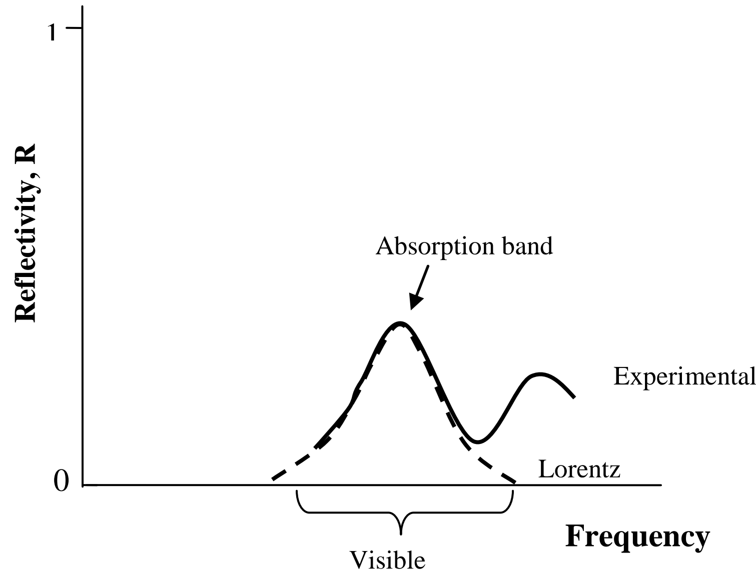

Figure 1.3: Reflectivity of metals in the visible region experimentally (solid line) and according to the Lorentz model (dotted line).

external electric field, the positively charged nucleus and the negative electron cloud are displaced with respect to each other. An electrostatic force tries to counteract this displacement. If the negative charge of the electrons is considered to be a point charge, then the atom in an electric field can be described as a positively charged core bound quasi-elastically to one electron, i.e., it can be considered to be a dipole. Thus, the well-known harmonic oscillator equations of mechanics can be applied if a bound electron is considered a mass suspended from a spring that performs forced vibrations under the influence of an alternating electric field.

$$m\frac{d^2x}{dt^2} + \gamma' \frac{dx}{dt} + \kappa x = eE_0 \exp(i\omega t) \qquad (1.20)$$

Here, the expression on the right hand side represents the force of an external electric field that periodically displaces an electron from its rest position by a distance x. This displacement is resisted by a restoring force $\kappa \cdot x$, where κ, the

spring constant, determines the binding strength between the atom and the electron. Each vibrating dipole loses energy by radiation: thus, the second term in the equation represents the damping of the oscillator by radiation.

As a result of this approach, the dielectric constant can be expressed in terms of a damping factor (energy loss through radiation) and the resonance frequency of the vibration, ν_0. Figure 1.4 shows the frequency dependence of ε_1 and ε_2 for dielectrics calculated according to the Lorentz approach. Except for a narrow region near the resonance frequency, ε_1 increases with increasing frequency. This is called the normal dispersion; the anomalous dispersion is the region near ν_0 where ε_1 decreases with increasing frequency. Figure 1.4 also shows that ε_2 is always positive and approaches zero for frequencies far from ν_0, whereas ε_1 may be either positive or negative and approaches the value of 1 at frequencies far from ν_0.

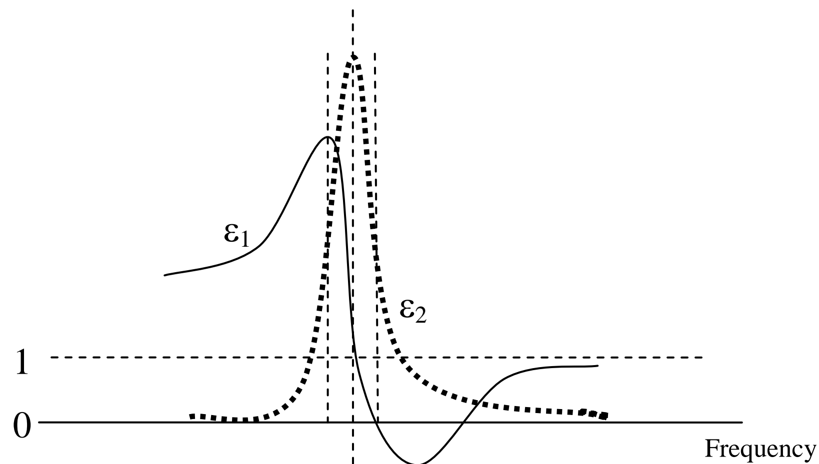

Figure 1.4: Frequency dependence of ε_1 and ε_2 for dielectrics calculated according to

The optical properties of metals can be modeled as a combination of the Drude and Lorentz models: at low frequencies, electrons behave as if they were free and at higher frequencies as if they were bound. By combining the two approaches, the experimentally found frequency dependence of ε_1 and ε_2 can be successfully predicted. Insulators and semiconductors are modeled by harmonic oscillators only. It can be shown that the Lorentz equations reduce to the Drude equations for $\nu_0 \rightarrow 0$ (no oscillators).[4]

1.5.2. Quantum Mechanical Treatment

In the classical approach, electrons are postulated to behave like particles which at small frequencies are essentially free whereas at higher frequencies they behave like harmonic oscillators. The reasons for the division are not immediately obvious however, and a quantum mechanical approach is necessary to avoid this dichotomy.

1.5.2.1. ***Band Structure of Solids***

From high resolution transmission electron microscopy and X-ray diffraction studies, it is known that atoms in a crystal are arranged periodically. Thus a suitable potential distribution for an electron in a solid is a periodic arrangement of potential wells and potential barriers, such as the Kronig-Penney model shown in Figure 1.5 below. The discussion that follows is based on that of Hummel.[6] This model features potential wells of length a separated by potential barriers of height V_0 and width b, where V_0 is assumed to be larger than the energy of the electron, E. This model is a simplification of the actual potential in a crystal: it does not take into account that the potential function of a point charge varies as

1/*r* or that the individual potentials from each lattice point overlap.

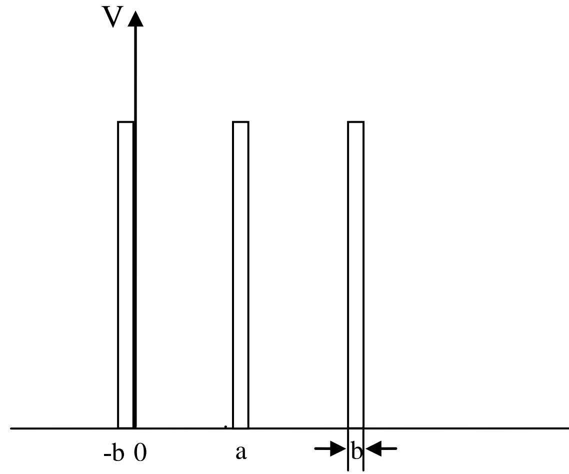

Figure 1.5: A simplified one-dimensional periodic potential distribution after the Kronig-Penney model.

The Schrödinger equation for the potential well and barrier can be written respectively as:

$$\frac{d^2\psi}{dx^2} + \frac{2m}{\hbar^2}E\psi = 0 \qquad \text{and} \qquad (1.21)$$

$$\frac{d^2\psi}{dx^2} + \frac{2m}{\hbar^2}(E - V_0)\psi = 0 \qquad (1.22)$$

The solution to the above equations is the well-known Bloch function:

$$\psi(x) = u(x).e^{ikx} \qquad (1.23)$$

where *u(x)* is a periodic function that possesses the periodicity of the lattice in the *x* direction. The function *u(x)* does not have a constant amplitude; it changes periodically with increasing *x* (modulated amplitude) and is also different for various directions in the crystal lattice. The relation that provides allowed solutions to equations 1.21 and 1.22 is of the form

$$P\frac{\sin \alpha a}{\alpha a} + \cos \alpha a = \cos ka \tag{1.24}$$

where $P = \frac{maV_0 b}{\hbar^2}$ and $\alpha^2 = \frac{2m}{\hbar^2}E$

Because of the trigonometric relation, only certain values of α and thus E are allowed. The important result here is that since αa is a function of the energy, an electron that moves in a periodically varying potential field can only occupy certain allowed energy zones; energies outside these allowed zones or "bands" are prohibited. The size of the allowed and forbidden energy bands varies with P: four special cases can be distinguished.

1. If the potential barrier strength $V_0 b$ is large, P is also large and the allowed bands are narrow.

2. If the potential barrier strength $V_0 b$ and therefore P is small, the allowed bands are wider.

3. If the potential barrier strength becomes smaller and smaller and finally disappears completely, P goes toward zero and from equation 1.24, the result

$$\cos \alpha a = \cos ka \quad \text{or} \quad \alpha = k$$

is obtained. This result gives the energy of the electron as identical to the free electron case.

4. If the potential barrier strength is very large, P approaches infinity. However, since the left hand side of equation 1.24 has to remain finite (between the limits ± 1), then $\sin \alpha a \to 0$. This results in energies identical to the bound electron case.

The preceding discussion can be summarized as follows: if the electrons are strongly bound, i.e., the potential barrier is very large, one obtains sharp energy

levels (electrons in the potential field of one ion). If the electron is not bound, one obtains a continuous energy region (free electron). If the electron moves in a periodic potential field, one obtains energy bands (solid). The widening of the energy levels into energy bands and the transition into a quasi-continuous energy region is shown in Figure 1.6. This widening occurs because the atoms increasingly interact as the interatomic separation decreases.[7, 8]

Band structures for solid materials (crystals) show characteristic features. In metals, the individual energy bands overlap in different directions in *k*-space so that as a whole, no band gap exists. In semiconductors, a region where there are no energy bands exists. This energy gap, or band gap, is responsible for the well-known properties of semiconductors. Insulators are characterized by completely filled valence bands and empty "conduction" bands. The gap energy is fairly large, typically greater than 5 eV.[6, 8]

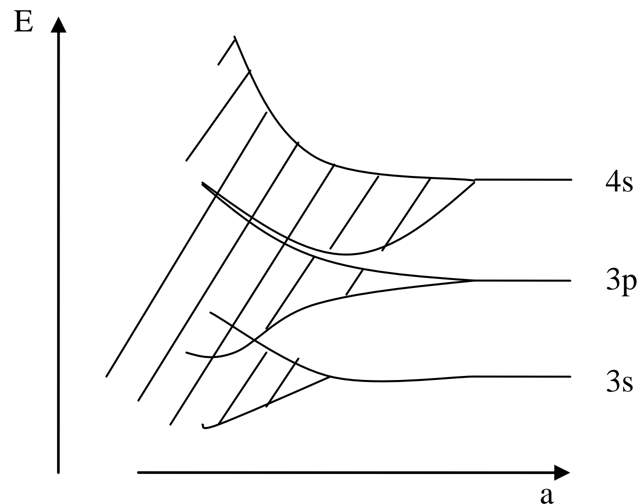

Figure 1.6: The widening of the energy levels into energy bands and the transition into

1.5.2.2. ***Absorption of Light by Interband and Intraband Transitions***

When light having sufficiently large energy impinges on a solid, the electrons in the crystal are excited into a higher energy level depending on the availability of higher unoccupied energy levels. For these transitions, the total momentum of the electrons and photons must be conserved. Electron transitions at which the wave vector of the photon, **k** remains constant (vertical transitions) are called direct interband transitions (Figure 1.7). Optical spectra for metals are dominated by direct interband transitions. Between any two bands in a metal, several transitions of varying energies are possible; as well, interband transitions are also possible by skipping one or more bands. Thus, a multitude of absorption bands are possible, which may partially overlap.[6]

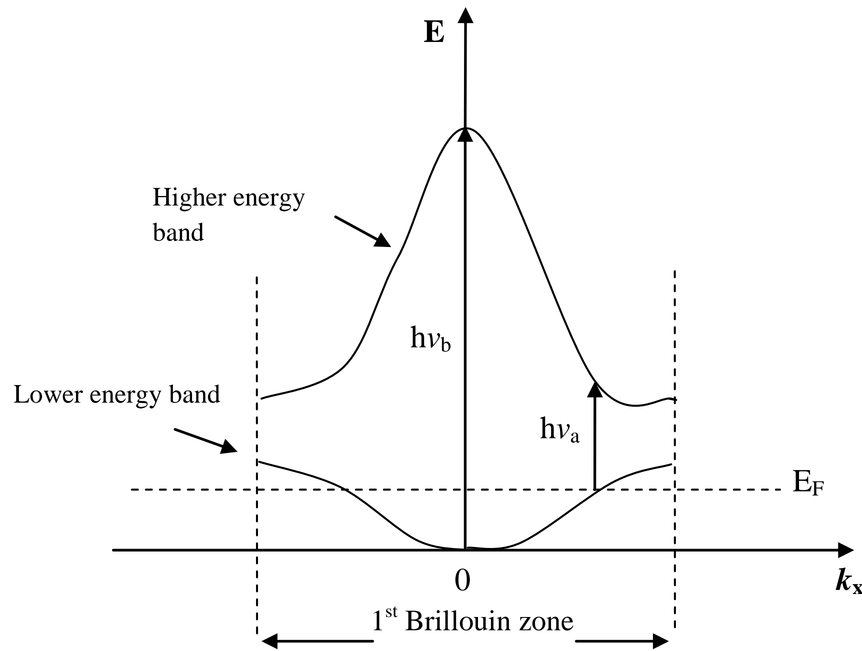

Figure 1.7: Scheme showing direct interband transitions: $h\nu_a$ and $h\nu_b$ illustrate two such possible transitions. E_F is the Fermi level energy.

Another type of interband transition, called an indirect interband transition, is possible: it involves the absorption of a light quantum under participation of a phonon (lattice vibration quantum). Phonons can absorb only very small energies but can absorb a large momentum comparable to that of the electron. During an indirect interband transition, the excess momentum is transferred to or from the lattice, i.e., a phonon is exchanged with the solid. Indirect interband transitions are not important for metal spectra because they are weaker by several orders of magnitude and are only observed in the absence of direct transitions. They are however important for semiconductors.

Under certain conditions, a photon may excite an electron into a higher energy level within the same band. This occurs with participation of a phonon and is called an intraband transition. These transitions are mainly observed in metals because metals have unfilled electrons bands. Semiconductors with high doping levels or which are kept at high temperatures may also show these transitions because of partially filled conduction bands.

Intraband transitions are equivalent to the behavior of free electrons in classical physics. Insulators and semiconductors have no classical infrared absorption because their bands are either completely filled or completely empty. The largest photon energy that can be absorbed by means of an intraband transition corresponds to an excitation from the lower to the upper band edge; all energies lower than this maximum value are absorbed continuously.

In summary, at low photon energies, intraband transitions, if possible, are the prevailing absorption mechanism. Intraband transitions are not quantized and

occur essentially in metals only. Above a critical light energy interband transitions predominate. Only certain energies or energy intervals are absorbed, dependent on the energy difference between the bands involved. Interband transitions occur in metals, semiconductors and insulators and are analogous to optical excitations in solids with bound electrons. In an intermediate frequency range, both types of transitions can occur simultaneously.[6]

1.6. Optical Spectra of Materials

1.6.1. Dispersion Relationships

The term dispersion was originally used to describe how far a prism of a material will separate the extreme colors from the mean ray. Dispersion relationships are used to describe the optical constants of a material and are simply equations which give the values of n and k as functions of wavelength. Some of these relationships are strictly empirical but most are based on physical principles.

The best-known dispersion relationship was developed by L. Cauchy (1830). He observed that for most transparent materials, the index n decreased with increasing wavelength in the visible range and could be expressed approximately as

$$n(\lambda) = n_0 + \frac{n_1}{\lambda^2} + \frac{n_2}{\lambda^4}$$

where n_0, n_1 and n_2 are parameters known as the Cauchy coefficients. n_0 gives the constant value at long wavelengths, $n_1$controls the curvature in the middle of the visible spectrum and n_2 influences the spectrum to a greater extent at shorter

wavelengths. The Cauchy relationship is usually used as an empirical method. The extinction coefficient is usually described with a similar expression to *n* and the coefficients are called the Cauchy extinction coefficients.

Another dispersion relationship frequently used is the oscillator model. An example is the Lorentz oscillator model described in section 1.4. There are several other mathematical descriptions that are frequently used to model oscillators but the Lorentz model is the most commonly used and is useful to illustrate the qualitative aspects of insulators, semiconductors and metals by observing where the resonant frequency lies in the spectral range. Real materials correspond to a collection of oscillators grouped together in the ultraviolet, visible and/or infrared range.[4]

1.6.1.1. ***Dielectrics (Insulators)***

The resonant frequency, ω_0, is related to the bandgap energy, E_g, for the material: $E_g \approx \hbar\omega_0$. For materials considered as insulators or dielectrics, such as SiO_2 and KCl, the value of the resonant frequency ω_0 lies well into the ultraviolet range, i.e., the band gap is high. If one is only observing the visible region, the value of *n* decreases slightly as the wavelength increases and the value of *k* is essentially zero. The dispersion of *n* can be modeled using a three parameter Cauchy function in the visible region; if the ultraviolet range is included, this may no longer be sufficient as the value of *k* may be no longer negligible. Figure 1.8 shows the optical functions for a typical insulator.

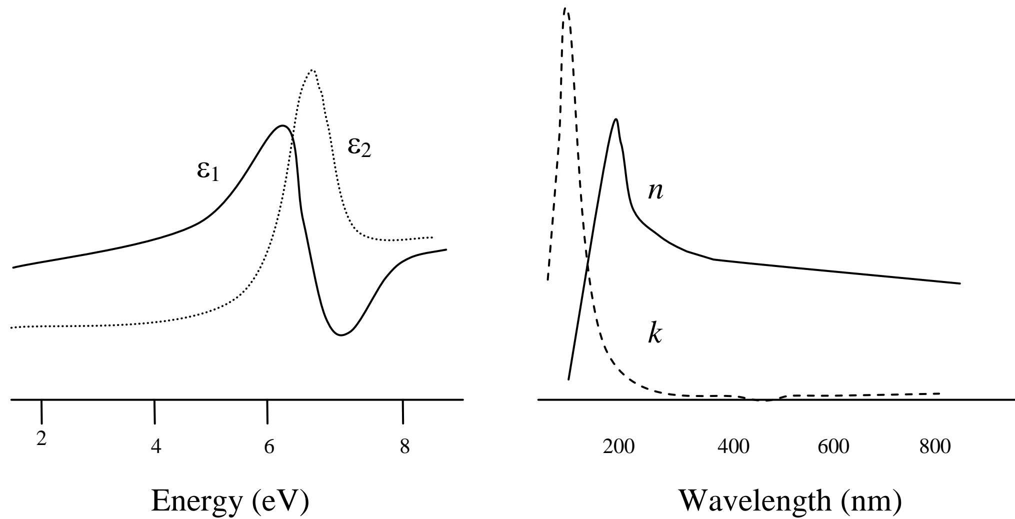

Figure 1.8: Optical functions for a typical insulator

In the infrared region of the spectrum, another absorption mechanism, caused by the light-induced vibrations of the lattice atoms, may occur. This is termed phonon excitation and is the collective vibration of the lattice atoms about their equilibrium locations. The situation can be modeled similarly to that of the Lorentz oscillator, which describes the electron as being bound quasi-elastically to the nucleus. In this case, the vibrations are damped due to interactions of the phonons with lattice defects, the external surfaces of the crystal and with other phonons. The oscillator possesses one or several resonance frequencies, which depend on the mass of the atoms and the vibrational modes, as well as the restoring force.[4]

1.6.1.2. ***Semiconductors***

Intrinsic semiconductors have, at low temperatures, a completely filled valence band and an empty conduction band. Consequently, no intraband transition, or classical infrared absorption is possible. Semiconductors are usually

modeled using oscillators; usually, as many as three are required to accurately reproduce their optical behavior. The resonant frequency is close to, or in the visible range since the band gap (0.2 – 3.5 eV) is smaller than it would be for an insulator. The extinction coefficient is small but nonzero. Figure 1.9 shows the optical spectra for a typical semiconductor.[4]

Indirect interband transitions may also be observed in semiconductor spectra. As mentioned before, these are due to phonon-assisted transitions between the top of the valence band and the bottom of the conduction band and are generally very weak. Several other absorption mechanisms are possible: the most important of these is the Frenkel exciton absorption. This is observed as absorption slightly below the band gap energy. It is postulated that the photon is able to excite an electron so that it remains in the vicinity of its nucleus, thus forming an electron-hole pair, the exciton. The exciton is thought to be bound together by electrostatic forces and revolve around their mutual centre of mass. The exciton absorption is represented by introducing “exciton levels” into the band gap region; they are separated from the conduction region by the binding energy, which is usually quite small, around 0.01 eV. Exciton levels may be further broadened by interactions with phonon or impurities.[6]

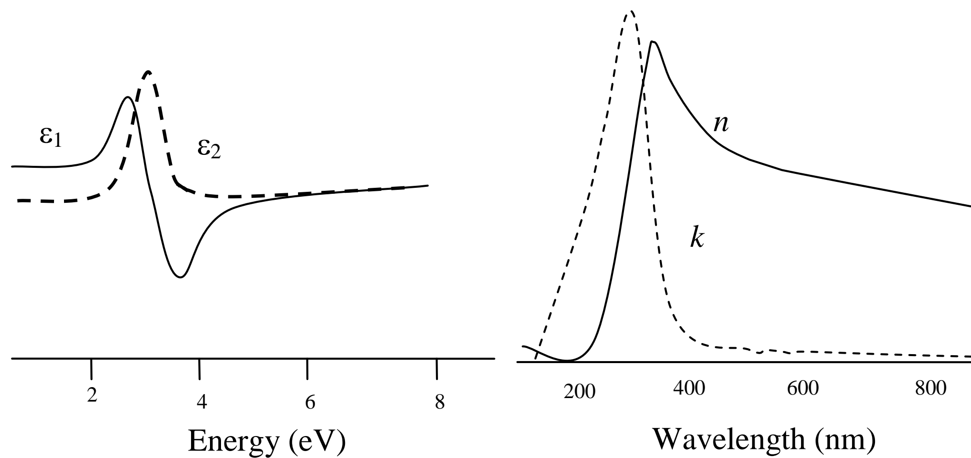

Figure 1.9: Optical functions for a typical semiconductor

1.6.1.3. ***Metals***

Metals can be described by the Drude model, which is a modification of the Lorentz oscillator. Since the free electrons in a metal are not bound, the restoring force is considered to be zero, which is equivalent to setting ω_0 to zero. The damping force is still present and represents the ordinary scattering of electrons associated with lattice collisions. This free electron model can adequately describe the behavior of aluminum. For other metals, such as silver, the optical spectra have to be explained using a combination of free and bound electrons (classical approach) or interband and intraband transitions (quantum mechanical approach). The dominant feature of the optical constant spectra is that as the wavelength increases, the values of both n and k increase (Figure 1.10). Additionally, as discussed earlier, most metals have some structure in the visible range; some have indices of refraction that are less than 1.0 in part of the spectral range.[4]

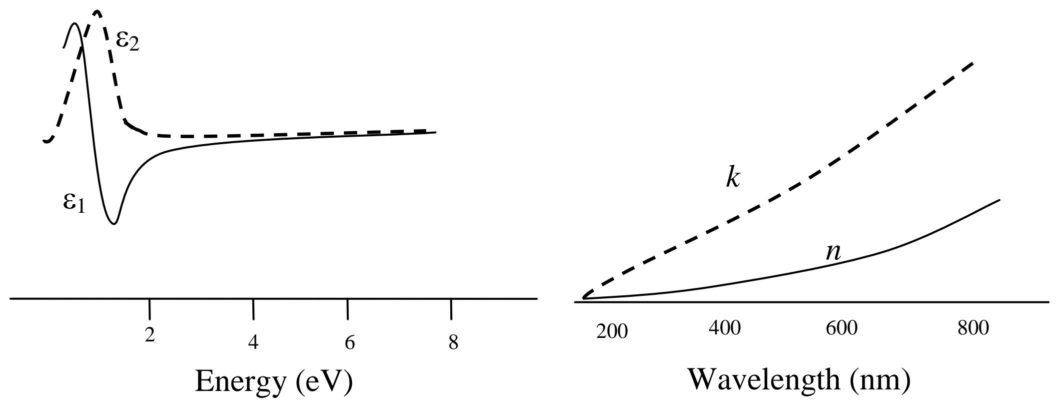

Figure 1.10: Optical functions for a typical metal

1.7. Optical Properties of Solid Thin Films

1.7.1. Importance of Thin Films

A solid material is said to be in thin film form when it is built up, as a thin layer on a solid support, called a substrate, by controlled condensation of the individual atomic, molecular, or ionic species, either directly by a physical process, or via a chemical and/or electrochemical reaction. It is not just simply the small thickness that endows thin films with special and distinctive properties, but rather the microstructure resulting from their unique formation process, that is, by the addition of basic building blocks one by one. In thin films, deviations from the properties of corresponding bulk materials because of their small thickness, large surface-to-volume ratio, and unique physical structure is a direct consequence of the growth process. Some of the phenomena arising as a natural consequence of small thickness are optical interference, electronic tunneling through an insulating layer, high resistivity and low temperature coefficient of resistance and planar magnetization.[9]

1.7.2. Thin Film Optics

1.7.2.1. *Reflection and Transmission of Light By A Single Film*

As described earlier in Section 1.1, if a beam of light is incident at an angle φ_1 at a plane interface between two isotropic media of uniform refractive indices n_0 and n_1, and is refracted at an angle φ_0 in the second medium, then the ratios of the incident to reflected radiation (r_1) and transmitted to incident radiation (t_1) amplitudes are given by the Fresnel coefficients (equation 1.4).

For a parallel-sided, isotropic film of refractive index n_1 between media of

indices n_0 and n_2 (Figure 1.11), the amplitude reflectance and transmittance may be obtained by summing multiply-reflected beams. The resulting expression is:

$$\Re = \frac{r_2 + r_1 \exp(-2i\delta_1)}{1 + r_2 r_1 \exp(-2i\delta_1)} \quad (1.21) \quad \text{and} \qquad \mathrm{T} = \frac{\hat{t}_1 \hat{t}_2 \exp(-2i\delta_1)}{1 + r_2 r_1 \exp(-2i\delta} \quad (1.22)$$

where r_1, r_2, $\hat{t}_1$ *and* $\hat{t}_2$ are the Fresnel coefficients at the n_0/n_1 and n_1/n_2 interfaces, $\delta_1 = (2\pi/\lambda)n_1 t \cos \varphi_1$ is the phase thickness of the film and λ is the wavelength in vacuo. Equation 1.21 and 1.22 are valid for either the *p* or *s* directions of polarization provided that the correct values of *r* and *t* are used consistently.

The reflectivity and transmissivity are given by

$$R = \frac{r_1^2 + r_2^2 + 2r_1 r_2 \cos 2\delta_1}{1 + r_1^2 r_2^2 + 2r_1 r_2 \cos 2\delta_1} \tag{1.23a}$$

$$T = \frac{n_0}{n_2} \frac{\hat{t}_1^2 \hat{t}_2^2}{1 + 2r_1 r_2 \cos 2\delta_1 + r_1^2 r_2^2} \tag{1.23b}$$

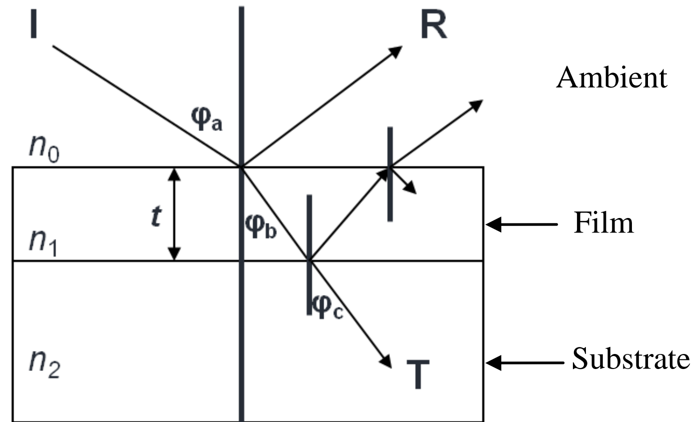

Figure 1.11: Ray diagram of light interacting with a parallel-sided, isotropic film

These general expressions can be written in terms of the refractive indices but are extremely long and cumbersome; a manageable expression is obtained only for the special case of normal incidence and transparent media, under which condition n is real. The normal reflectance exhibits oscillatory variation as illustrated in Figure 1.12 by the plot of $\Re$ vs. wavelength for two films of different thicknesses. The reflectance at the maxima and minima are as follows:

For $n_0 \leq n_1 \leq n_2$,

$$R_{\max} = \left(\frac{n_2 - n_0}{n_2 + n_0} \right)^2 \quad \text{at} \quad \lambda_{\max} = \frac{2n_1 t}{m} \tag{1.24a}$$

and

$$R_{\min} = \left(\frac{n_1^2 - n_0 n_2}{n_1^2 + n_0 n_2} \right)^2 \quad \text{at} \quad \lambda_{\min} = \frac{4n_1 t}{2m+1} \tag{1.24b}$$

where m is an integer. If $n_0 \leq n_1 \geq n_2$, then the expression for $R_{\min}$ becomes the expression for $R_{\max}$ and vice versa. These expressions indicate that by a suitable choice of the film index, we can either enhance (reflection coating) or diminish (antireflection coating) the reflectance of a given substrate. Further, the oscillatory behavior of R may be utilized as a spectrophotometric method for monitoring the thickness of single or multilayer films during deposition, as well as for determining the optical constants of thin films.

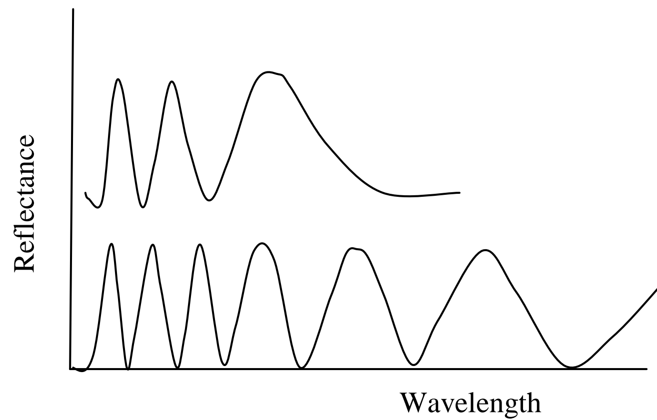

Figure 1.12: Reflectance vs. wavelength for thinner (top) and thicker (bottom) film of the same material

Equations 1.23a and 1.23b are general and valid for any type of film and substrate media. The algebraic expressions are however cumbersome for different combinations of absorbing (complex *n*) and non-absorbing (real *n*) media. A point to note however is that the *p* and *s* components of a reflected beam, in general, have different amplitudes for non-normal incidence. For reflection from a transparent medium, the *p* component goes through a minimum of amplitude and a phase change of π at an angle of incidence greater than ϕ_p. This angle is called the polarizing angle because unpolarized light will be reflected at this angle to become plane-polarized. At this angle ϕ_p,

$$n_0 = n_1 \tan \phi_p \qquad \text{(Brewster's Law)}$$

For reflection from an absorbing surface, both the amplitudes and the phases of the *s* and *p* components are different; thus, the resultant reflected light is elliptically polarized. The ratio of the amplitudes of reflectance of the *p* and *s* component can be written in a generalized form as

$$\frac{\Re_p}{\Re_s} = e^{i\Delta} \tan\psi \tag{1.25}$$

where Δ is the relative phase difference and ψ is the azimuth, the ratio of the reflection amplitudes of the p and s components. Since Δ and ψ are related to the optical constants, a measurement of ψ and Δ should in principle yield the value of the constants – this is the basis of the spectroscopic ellipsometry technique, which will be discussed in detail in chapter 3.[4, 10]

1.7.2.2. ***Reflection and Transmission of Light by Multiple Layers***

A multilayer film is a finite combination of single layers having different optical constants and film thicknesses. Because a wide variety of applications of thin film optics are based on a multilayer thin film, the calculations of reflection, transmission and absorption properties of a multilayer as a function of wavelength of light for any arbitrary angle of incidence is an important problem. The treatment of such a problem is computationally tedious and various mathematical formulations have been devised for computer computations.[9] Some of the most widely used methods are those developed by P. Rouard, A.W. Crook and A. Vasicek. A single film bounded by two surfaces possesses an effective reflection coefficient and accompanying phase changes, and may be replaced by a single film with these properties. Thus, starting with the film nearest the substrate (or the top layer of the multilayer), and moving step by step through the intervening layers, an expression for the reflectivity of the system may be obtained. Methods are also available for dealing with multilayers of absorbing films at normal and non-normal incidence: the latter can be treated with the method of Abeles.[10]

References

1. Young, H. D.; Freedman, R. A., *University Physics*. 9th Ed. ed.; Addison-Wesley Publishing Company: 1996; Vol. Vol. 2.

2. Kerker, M., *The scattering of light and other electromagnetic radiation*. Academic, New York: 1969.

3. Hulst, H. C. v. d., *Light Scattering by Small Particles*. Dover Publications, New York: 1981.

4. Tompkins, H. G.; McGahan, W. A., *Spectroscopic Ellipsometry and Reflectometry: A User's Guide*. John Wiley and Sons, Inc.: 1999.

5. Hecht, E., *Optics*. 2nd Ed. ed.; Addison-Wesley: 1987.

6. Hummel, R. E., *Electronic Properties of Materials*. 3 ed.; Springer-Verlag: 2001.

7. Azaroff, L. V., *Introduction to Solids*. Tata McGraw-Hill Publishing Company Limited: 1977; p 460.

8. West, A. R., *Solid State Chemistry and its Applications*. John Wiley and Sons: 1984.

9. Chopra, K. L., *Thin Film Phenomena*. McGraw-Hill: 1969.

10. Heavens, O. S., *Optical Properties of Thin Solid Films*. Dover Publications Inc.: 1991.

CHAPTER 2: Synthesis, Structure and Fabrication of Thin Films

2.1. Introduction

Thin films first came to prominence as reflective and anti-reflective coatings in optical devices. Since the development of vacuum evaporation systems, the number and diversity of thin film applications have increased considerably. These now include evaporated electrodes in electrical applications, electronic components as layers of insulators, semiconductors and conductors to form integrated circuits, and as multilayer filters: low and high pass, low-reflecting to highly reflecting. Specialized filters, comprising many layers, can be fabricated to specifications with little or no difficulty using modern deposition techniques.[1-3]

2.2. Thin Film Growth Process

A thin film deposition process involves three main steps: (1) production of the appropriate atomic, molecular, or ionic species, (2) their transport to the substrate through a medium, and (3) condensation on the substrate, either directly or via a chemical and/or electrochemical reaction, to form a solid deposit. Formation of a thin film takes place via nucleation and growth processes. From various experimental and theoretical studies, the process can be outlined as follows:

1. The chemical species, on impinging the substrate, lose their velocity component normal to the substrate and are physically adsorbed on the substrate surface.
2. The adsorbed species are not in thermal equilibrium with the substrate initially and move over the surface. During this process, they interact with each other,

forming bigger clusters. The clusters, or nuclei as they are called, are thermodynamically unstable and tend to desorb in a time depending on the deposition parameters. If the deposition parameters are such that a cluster collides with other adsorbed species before getting desorbed, it starts growing in size. After a certain critical size is reached, the cluster becomes thermodynamically stable and the nucleation barrier is said to have been overcome. This step involving the formation of stable, chemisorbed, critical-sized nuclei is called the nucleation stage.

3. The critical nuclei grow in number as well as in size until a saturation nucleation density is reached. The nucleation density and the average nucleus size depend on a number of parameters such as the energy of the impinging species, the rate of impingement, the activation energies of adsorption, desorption and thermal diffusion, and the temperature, topography and chemical nature of the substrate. A nucleus can grow both parallel to the substrate by surface diffusion of the adsorbed species, as well as perpendicular to it by direct impingement of the incident species. In general, however, the rate of lateral growth at this stage is much higher than the perpendicular growth. The grown nuclei are called islands.

4. The next stage in the process of film formation is the coalescence stage, in which the islands start coalescing with each other in an attempt to reduce the surface area. This tendency to form bigger islands is called agglomeration and is enhanced by increasing the surface mobility of the adsorbed species, as for example, by increasing the substrate temperature. In some cases, formation of new nuclei may occur on the areas freshly exposed as a consequence of coalescence.

5. Larger islands grow together, leaving channels and holes of uncovered substrate.

The structure of the films at this stage changes from discontinuous island type to porous network type. A completely continuous film is formed by filling of the channels and holes.[2]

The growth process may thus be summarized as consisting of a statistical process of nucleation, surface-diffusion controlled growth of the three-dimensional nuclei, and formation of a network structure and its subsequent filling to give a continuous film. Depending on the thermodynamic parameters of the deposit and the substrate surface, the initial nucleation and growth stages may be described as a layer type, island type or mixed type (called Stranski-Krastanov type). In almost all practical cases, the growth takes place by island formation.[2]

2.3. Physical Structure of Thin Films

The microstructural and topographical details of a thin film of a given material depend on the kinetics of growth and hence on the substrate temperature, source temperature, chemical nature and topography of the substrate and gas ambients. The parameters influence the surface mobility of the adsorbed species, kinetic energy of the incident species, deposition rate, vapor pressure and solution concentration required for condensation to the solid phase under thermodynamic equilibrium conditions, the condensation or sticking coefficient and the level of impurities. Each of these parameters affects the physical structure of the film.[2]

2.3.1. Crystallographic Orientation

Except under special conditions, the crystallographic orientation and the topographical details of different islands are randomly distributed, such that when

they touch each other during growth, grain boundaries and various point and line defects are incorporated into the film due to mismatch of geometrical configurations and crystallographic orientations. If the grains are randomly oriented, the films show a ring-type diffraction pattern indicative of a polycrystalline structure. If the grain size is small (< ~20 Å), the films show halo-type diffraction patterns consistent with highly disordered, amorphous structures. If the film consists of single-crystal grains oriented parallel to each other and connected by low-angle grain boundaries then the films shows a diffraction pattern similar to those of single crystals and are called epitaxial or single-crystal films.[2]

Besides grain boundaries, dislocations of density are the most frequently encountered defects in polycrystalline films and are largely incorporated during the network and hole stages, due to orientation or displacement misfits between different islands. Epitaxial films may contain structural defects such as dislocation lines, stacking faults and minor defects caused by aggregation of point defects. Some other mechanisms which may give rise to dislocations in thin films are lattice mismatch between substrate and film, the presence of inherent large stresses in thin films and incorporation of substrate defects into the growing film.[2]

2.3.2. Grain Size

After a continuous film is formed, the anisotropic growth takes place normal to the substrate in the form of cylindrical columns. The lateral grain or crystallite size of a film is largely determined by the initial nucleation density. The grain size normal to the substrate is essentially equal to the film thickness for small (<1 μm) thicknesses. For thicker films, re-nucleation takes place at the surface of the previously grown

grains, and each vertical column grows multigranularly with possible deviations from normal growth.

The lateral grain size is expected to increase with decreasing supersaturation and increasing surface mobility of the adsorbed species. Therefore, at high substrate and source temperatures, well-defined large grains are formed as a result of high surface mobility under those conditions. However, increasing the kinetic energy of the incident species is not without limit: at sufficiently high energies, surface mobility is reduced due to the penetration into the substrate, resulting in smaller grain size. The effect on grain size of increasing substrate temperature and kinetic energy of impinging species is more pronounced for relatively thicker films.

Grain size may also be modified by post-deposition annealing at temperatures higher than the original deposition temperature. The higher the annealing temperature, the larger the grain size obtained; again, the effect is more pronounced for thicker films. The grain growth obtained is significantly reduced from that which could be obtained during deposition at the annealing temperature; this is due to the much higher energy activation process employed during post-deposition annealing.[2]

2.3.3. Surface Roughness

Fine-grained, smooth deposits which become continuous at small thicknesses are usually formed under conditions where there is a low nucleation barrier and high supersaturation. This is due to the high initial nucleation density and the small size of the critical nucleus. If the opposite situation exists, then large

but few nuclei are formed which result in coarse-grained, rough films which only become continuous at relatively large thicknesses. High surface mobility generally increases surface smoothness by filling in the valleys except in special cases where the material grows preferentially along certain crystal faces. A further enhancement in surface roughness occurs in the impinging species are incident at oblique angles instead of normally. This may be due to the shadowing effect of the neighboring columns oriented towards the direction of the incident species.[2]

2.3.4. Density

It is generally observed that density decreases with decreasing film thickness. Higher substrate temperatures result in the thin film density approaching the bulk values more quickly. Again, the density values are very dependent on deposition conditions.[2]

2.3.5. Metastable Structures

In general, departures from bulk values of lattice constants are found only in ultrathin films. The lattice constants may increase or decrease, depending on whether the surface energy is negative or positive, respectively. As the thickness of the film increases, the lattice constants approach the corresponding bulk values.
A large number of materials exhibit new metastable structures, not found in the corresponding bulk materials, when prepared as thin films. These new structures may be either due purely to deposition conditions or may be impurity/substrate stabilized. Some common examples of such abnormal structures found in thin films are amorphous Si, Ge, Se, Te and As; face-centered cubic (fcc) Mo, Ta, W, Co due to deposition conditions; fcc Cr/Ni and Co/Cu due to substrate influence. These

abnormal metastable structures all transform to the stable, normal structures upon annealing.[2]

2.3.6. Solubility Relaxation

Solubility relaxation is a phenomenon attributable to the thin film growth process. The atomistic process of growth during co-deposition allows doping and alloying of films. Since thin films are formed from individual atomic, ionic or molecular species which have no solubility restrictions in the vapor phase, the solubility conditions between different materials on co-deposition are considerably relaxed. This allows the preparation of multi-component materials, such as alloys and compounds, over an extended range of compositions as compared to the corresponding bulk materials: it is thus possible to tailor-make materials for technology applications. An example is the formation of hydrogenated silicon films for use in solar cells: hydrogenation makes varying the band gap, as well as doping of the material possible.[2]

2.4. Thin Film Technology

Thin films are usually formed by deposition – the main methods can be classified as either physical or chemical deposition processes. Physical deposition processes are much more widely used and will be considered in more detail.

2.4.1. Chemical Deposition

Here, a fluid precursor undergoes a chemical change at a solid surface, leaving a solid layer. Since the fluid surrounds the solid object, deposition happens

on every surface, with little regard to direction; thin films from chemical deposition techniques tend to be conformal, rather than directional. This technique can be further classified by the phase of the precursor.

(a) Plating – this process starts with liquid precursors, often an aqueous solution of a salt of the metal to be deposited. This process can be reaction driven (for noble metals) but commercially, electroplating is much more commonly used.

(b) Chemical vapor deposition (CVD) uses a gas-phase precursor, usually a halide or hydride of the metal to be deposited.

(c) Plasma-enhanced CVD uses an ionized vapor or plasma as the precursor. The plasma is generated by the use of an electric current or microwave excitation.[1, 2]

2.4.2. Physical Deposition

The most important characteristic feature of this technique is that the transport of vapors from the source to the substrate occurs by physical means. This is achieved by carrying out the deposition in high vacuum conditions so that the mean free path of the ambient gas molecules is greater than the dimensions of the deposition chamber and the source to substrate distance. Under such low pressure ambient conditions, the transport of the material from the source to the substrate occurs by molecular beams.[2] Since particles tend to follow a straight path, films deposited by physical means are commonly directional, rather than conformal. Physical deposition uses mechanical (knocking out the atoms or molecules from the surface by using energetic heavy particles) or thermodynamic (evaporation) means to produce a thin film of solid. The latter is known as thermal evaporation and the former as sputtering. These two will be considered in more detail.

2.4.2.1. ***The Thermal Evaporation Process***

This method has been extensively developed, mostly due to the ease of control of the process. Films of high purity can be readily produced. The process is not however universally applicable – for instance, high melting point materials cannot readily be deposited without significant heating of the receiving substrate, whose temperature during deposition significantly affects the resulting film structure.[1]

The technique consists of vaporization of the solid material by heating it to a sufficiently high temperature and then allowing it to condense onto a cooler surface (the substrate) to form a film. Heating of the material can be carried out directly or indirectly by a variety of methods. The simplest and most common method is to support the material in a filament basket or boat which is then heated electrically. If the material is available in the form of a thin foil, it may be supported directly on the wire by wrapping. The use of the basket and wire-type sources is only possible in cases where the material sublimes or wets the support in melted form. Evaporation sources are usually made of refractory materials such as tungsten, molybdenum, tantalum and niobium with or without a ceramic coating. Crucibles of insulating materials such as quartz, graphite, alumina, berrylia and zirconia are heated indirectly by supporting them in a metal cradle. The choice of the filament or boat is determined by the evaporation temperature required and the resistance to alloying and/or chemical reaction with the evaporant. Direct heating of the material can be accomplished electrically or by focusing an electron or laser beam on it.[2]

The evaporated species, in the case of elements, consist of neutral single

atoms except for sulfur, selenium, tellurium, bismuth and arsenic which vaporize in the form of polyatomic clusters. In the case of alloys and compounds, vaporization is usually accompanied by dissociation and/or decomposition because of differences in the vapor pressures of the various constituents or because of thermal instability. If the constituents are equally volatile, congruent evaporation occurs. The compositions of the vapor and the condensate differ from that of the source is the evaporation is not congruent – this difference is aggravated if the condensation coefficients of the constituents differ from one another. The tendency to dissociate is also increased at high evaporation temperatures and low pressures. Very few compounds, such as magnesium fluoride, calcium fluoride, silicon oxide, germanium oxide and tin (II) oxide evaporate directly without dissociation.[2]

According to the Langmuir-Dushman theory of the kinetics of evaporation, the rate of free evaporation of atoms or molecules from a clean surface of unit area in vacuum is given by

$$N_e = 3.513 \times 10^{22}\ p_e\ (1/MT)^{1/2} \text{ molecules cm}^{-2}\ \text{s}^{-1}$$

where p_e is the equilibrium vapor pressure in torr of the evaporant under saturated vapor conditions at temperature T, and M is the molecular weight of the vapor species. The rate of condensation (deposition rate) of the vapors depends not only on the evaporation rate but also on the source geometry, its position relative to the substrate and the condensation coefficient.[2]

Because of collisions with ambient gas molecules, a fraction of the vapors, proportional to exp $(-d/\lambda)$, is scattered and hence randomized in direction within a distance d during their transfer through the gas. The mean free path λ for air at 25

°C and pressures of 10^{-4} torr and 10^{-6} torr is about 45 and 4500 cm respectively. Thus, pressures lower than 10^{-5} torr are necessary to ensure a straight line path for most of the evaporated species and for substrate to source distances of approximately 10 – 50 cm in a vacuum chamber.[2]

Good vacuum is also necessary to producing contamination-free films. A parameter of interest in this regard is the impingement rate of the ambient gas molecules. Besides the molecules of interest, the substrate is also impinged by the ambient gas molecules. Studies of residual air show that at the vacuum conditions (10^{-5} torr) and deposition rates (~ 1 Å sec^{-1}) commonly employed, the impingement rate of the ambient gas molecules is quite large, so that if the sticking coefficient of the gas is relatively large, a significant amount of gas sorption could occur. It turns out however that the sticking coefficient of the gas molecules at elevated temperatures is negligibly small making it possible to deposit clean films under those conditions with the exception of materials that are readily oxidizable, in which case, better vacuum conditions are required.[2]

Other variations of the vacuum evaporation technique are flash evaporation and molecular beam epitaxy (MBE). Flash evaporation is useful for multi-component deposition of materials having widely different vapor pressures. A single source is used at a temperature high enough to evaporate the least volatile material: small amounts of the material are continuously dropped into the heated source and evaporated discretely to completion. The net result is a vapor stream that has uniform, identical composition to the evaporant. MBE involves growth of epitaxial films by condensation of one or more controllably directed atomic or

molecular beams each emerging from a point source in an ultrahigh vacuum system. Because of the very slow deposition rates in this technique, epitaxial growth of high perfection is achieved at relatively low substrate temperature and multilayer structures of different materials in a predetermined sequence can be obtained. The technique is particularly important for epitaxial growth studies of multi-component materials such as II-VI and III-V compound semiconductors.[2]

2.4.2.2. *Sputtering*

In this technique, vapor species are created by mechanically knocking out the atoms or molecules from the surface of a solid material by bombarding it with energetic, nonreactive ions. The ejection process, sputtering, occurs as a result of momentum transfer between the impinging ions and the atoms of the target being bombarded. The sputtered species, which are predominantly neutral, can then be condensed on a substrate to form a thin film. The sputtering yield, defined as the number of ejected species per incident ion, increases with the energy and mass of the bombarding ions. The variation with energy shows a linear behavior in a small region above a threshold value determined by the sublimation energy of the target material. For higher energies, the yield approaches saturation, which occurs at higher energies for heavier bombarding particles. For example, Xe^+ bombardment shows saturation above 100 keV, whereas Ar^+ is saturated at less than 20 keV. At very high energies of the bombarding ions, the yield decreases because of the increasing penetration depth and hence increasing energy losses below the surface, with the consequence that not all the affected atoms are able to reach the surface.

The sputtering process is very inefficient from an energy point of view

because most of the energy is converted to heat, which becomes a serious limitation at high deposition rates. If the surface of a multi-component target does not change metallurgically by thermal diffusion, chemical reaction or back-sputtering processes, the sputtering process ensures layer by layer ejection and hence a homogeneous film of composition corresponding to that of the target. The high energy of the ejected species and the attendant bombardment of the growing film (acting as an anode) by electrons and negative ions have considerable influence on the growth of films and yields highly adherent films.[2]

Despite being energy intensive, the sputtering process is best suited to depositing adherent films of multi-component materials of any kind. Ions for sputtering may be produced either by using a glow discharge between the target and substrate holder or by using a separate ion beam source. Depending on the geometry of the target-substrate system and the mode of ion transport, a large number of sputtering variants have been developed.

Ion-Beam Sputtering. This technique produces ions in a high pressure chamber and then extracts them into a differentially pumped vacuum chamber through suitable apertures with the help of suitable electron and ion optics. A high density beam of ions may thus be produced for sputtering in high vacuum.[2] The yield is insensitive to the target temperature except at very high temperatures where it shows an apparent rapid increase due to the accompanying thermal evaporation.[2, 3]

Glow-Discharge Sputtering. This is a cheap and simple means of producing ions for sputtering. An electric field is applied between two electrodes in a gas at low pressure. The gas breaks down to conduct electricity above a certain

voltage. The cathode dark space, across which most of the applied voltage drops, is the most important region for sputtering. Ions and electrons created at breakdown are accelerated across this region. The energetic positive gas ions strike the cathode to produce sputtering and cause emission of secondary electrons which are essential for sustaining the glow discharge. The accelerated electrons produce more ions by collision with gas atoms in the negative-glow region lying adjacent to the cathode dark space.

Radio-frequency (RF) sputtering. Sputtering sources are usually magnetrons that utilize strong electric and magnetic fields to trap electrons close to the surface of the magnetron, which is known as the target. The electrons follow helical paths around the magnetic field lines undergoing more ionizing collisions with gaseous neutrals near the target surface than would otherwise occur. The sputter gas is inert, typically argon. The extra argon ions created as a result of these collisions leads to a higher deposition rate. It also means that the plasma can be sustained at a lower pressure. The sputtered atoms are neutrally charged and so are unaffected by the magnetic trap. Charge build-up on insulating targets can be avoided with the use of RF sputtering where the sign of the anode-cathode bias is varied at a high rate. RF sputtering works well to produce highly insulating oxide films but only with the added expense of RF power supplies and impedance matching networks. Stray magnetic fields leaking from ferromagnetic targets also disturb the sputtering process. Specially designed sputter guns with unusually strong permanent magnets must often be used in compensation.

References

1. Heavens, O. S., *Optical Properties of Thin Solid Films*. Dover Publications Inc.: 1991.

2. Chopra, K. L., *Thin Film Phenomena*. McGraw-Hill: 1969.

3. Chopra, K. L.; Kaur, I., *Thin Film Device Applications*. Plenum Press: 1983.

CHAPTER 3: Reflectometry and Ellipsometry

3.1 Introduction

Reflectometry and spectroscopic ellipsometry (SE) are techniques that measure the changes in the properties of light when it interacts with a sample. In the case of reflectometry, the measured property is the change in intensity upon reflection from the sample surface. In the case of ellipsometry, the change in polarized light upon reflection from or transmission through the sample is the property of interest. The light is usually elliptically polarized upon reflection, hence the name "ellipsometry".[1]

Reflectometry has been used since the time of Sir Isaac Newton in academic and research laboratories; however, commercial instruments did not appear until the late 1970's.[2] The basic principles of ellipsometry were established more than 100 years ago by Paul Drude (1887) but the technique was not widely used because of the time consuming nature of the technique. However, rapid advances in computer technology since the 1990's has allowed for the automation of both the instruments and data analysis, and this has led to a large increase in the use of the technique.[1, 3] In the year 2000 for example, over 600 research papers were published with ellipsometry in the title, compared with less than 100 in 1990.[4]

3.2 Applications of Reflectometry and Spectroscopic Ellipsometry

Reflectometry and SE are mainly used to obtain the optical constants and thicknesses of thin films after their preparation. From measurements in the ultraviolet/visible region, SE is also able to characterize interband transitions and yield bandgap information. Since bandgap structure varies with surface temperature, alloy composition, phase structure and crystal grain size, these properties can be obtained from the analysis of optical constant spectra. In the infrared region, at high enough carrier concentration, electrical properties can be obtained; moreover, lattice vibration modes and local atomic structures can be studied.[1] Recent advances have also seen SE used for real-time, *in-situ* monitoring of film growth and process control.[1, 3] From real-time monitoring, initial growth processes as well as interface structures can be studied and enable reaction rate characterization during processing.[1] Both techniques have been used widely: in the semiconductor industry for the analysis of substrates, thin films and gate dielectrics; in chemistry for studying polymer films, self-assembled monolayers, proteins and DNA; in display applications such as the characterization of TFT films, transparent conductive oxides and organic LEDs and in the production of high and low dielectrics for anti-reflection coatings.[1, 3, 5]

SE offers several advantages: first, it is a high precision technique with thickness sensitivity of approximately 0.1 Å in even the most conventional instruments.[1] SE and reflectometry are more comprehensive than any other tools: optical, electrical, physical (or structural) and chemical (composition, bonding)

information may be obtained from only one measurement. They are fast (measurements require only a few seconds), nondestructive and non-contact: no pattern is needed compared with a stylus profilometer for thickness. Ellipsometry is an absolute technique (no need of reference or standards) and in addition, as ellipsometry measures the polarization state and not the intensity, it is less sensitive to light intensity fluctuations. The phase information from ellipsometry is very sensitive to surface layers making it the best non-destructive technique for thin film characterization. Additionally, there is no vacuum requirement compared with all electron-beam or ion-beam based instruments.[1, 2, 6]

The main disadvantage of reflectometry and SE are that they are indirect methods: an optical model is required for interpretation of the data. This can lead to the necessity for complicated data analysis. Also, since the spot size of the light beam probe is usually several millimeters, this leads to low spatial resolution. There is also difficulty in the characterization of materials with low absorption coefficients ($\alpha < 100\ cm^{-1}$).[1]

For layers that are well understood and a few hundred to a few thousands of angstroms thick, reflectometry has the advantage of speed. The primary strength of SE is the ability to analyze multiple layers and to determine the optical constant dispersion relationship.[2] The combination of reflectometry with SE on a single instrument thus provides the best of both worlds: speed and sensitivity. Additionally, the analysis of multiple data sets ensures that systematic errors can be minimized.

3.3 Principles of Reflectometry and Ellipsometry

3.3.1 Reflectometry Principles

The basic principle of reflectometry is the measurement of the intensity of a light beam before and after reflection from a sample. The ratio of the intensity of the reflected beam to that of the incident beam is called the absolute reflectance of the sample. In practice, since it is difficult to measure the intensity of the beam before it strikes the sample, a relative intensity is instead measured. In this case, the intensity of the light beam reflected from the sample is divided by the intensity of the same light beam reflected from a standard. The absolute reflectance of the unknown sample can be calculated as long as the absolute reflectance of the standard is known. A bare, crystalline silicon wafer is usually used since the optical properties of silicon are well understood and so the absolute reflectance can be readily calculated from these optical constants.[1, 2]

3.3.2 Reflectometry Instrumentation

The basic reflectometry instrumentation consists of a light source, a reflection and a detector. For spectroscopic reflectometry, either the light source or the detector is able to separate the light into the various wavelengths. In this system, a light beam from the light source is incident on the sample at normal incidence (0°) and 70°. A halogen lamp is used in tandem with a deuterium source to provide illumination over a broad spectral range (240 – 920 nm). The detector system is used simultaneously for the ellipsometry measurement and is described below.

3.3.3 Ellipsometry Principles

Ellipsometry consists of the measurement of the change in polarization state of a beam of light upon reflection from (or transmission through) the sample of interest. Specifically, *p*- and *s*-polarized light waves are irradiated onto a sample and the optical constants and film thickness of the sample are measured from the change in polarization state by light reflection or transmission.[1] When the measurement is performed as a function of wavelength, as it was in this study, the technique is called spectroscopic ellipsometry.[2] The amplitude reflection coefficients for *p*- and *s*-polarizations differ significantly due to the difference in electric dipole radiation. Thus, upon light reflection from a sample, *p*- and *s*-polarizations show different changes in amplitude and phase. Ellipsometry measures the two values (ψ, Δ) that express the amplitude ratio and phase difference between *p*- and *s*-polarizations respectively. In ellipsometry, therefore, the variation of light reflection with *p*- and *s*-polarizations is measured as the change in polarization state. In particular, when a sample structure is simple, the amplitude ratio ψ is characterized by the refractive index n, while Δ represents light absorption described by the extinction coefficient k. In this case, the two values (n, k) can be determined directly from the two ellipsometry parameters (ψ, Δ) obtained from a measurement by using the Fresnel equations.[1, 2, 6]

The (ψ, Δ) measured from ellipsometry are defined from the ratio of the amplitude reflection coefficients for *p*- and *s*-polarizations:

$$\rho = tan\,\psi \exp(i\Delta) \equiv \frac{r_p}{r_s} \qquad (3.1)$$

As described in Chapter 1, r_p and r_s are originally defined by the ratios of

reflected electric fields to incident reflected fields, and tan ψ exp($i\Delta$) is defined further by the ratio of r_p to r_s. In Figure 3.2 therefore, ψ represents the angle determined from the amplitude ratio between the reflected *p*- and *s*-polarizations, while Δ expresses the phase difference between reflected *p*- and *s*-polarizations.

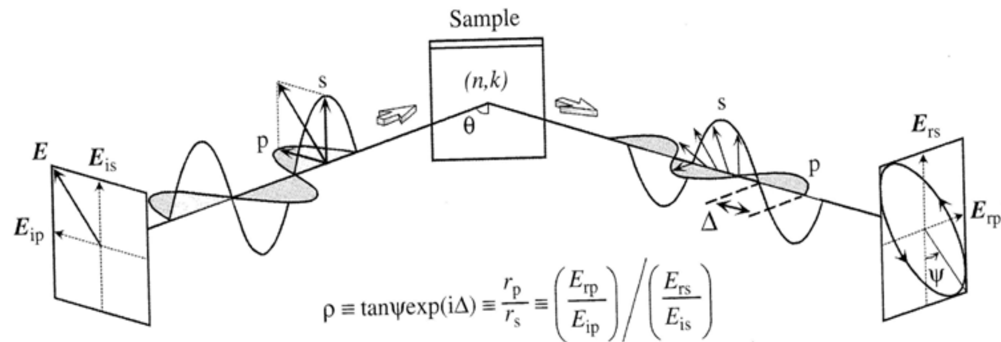

Figure 3.2: Measurement principle of ellipsometry.
From *Spectroscopic Ellipsometry Principles and Applications*, Hiroyuki Fujiwara, 2007, Copyright John Wiley and Sons Ltd. Reproduced with permission.

3.3.4 Ellipsometry Instrumentation

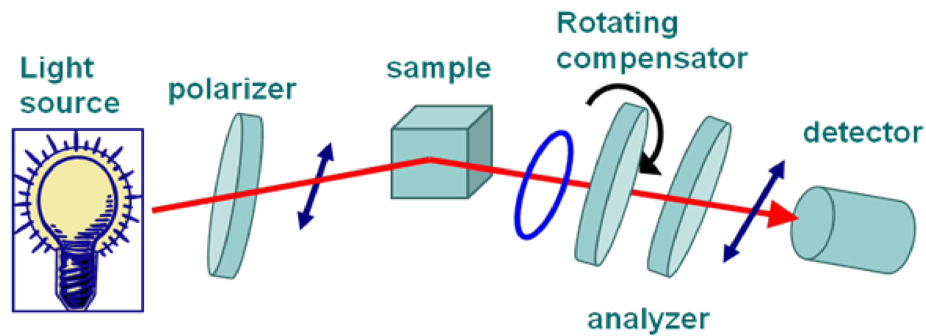

Figure 3.3: Optical configuration of the rotating compensator ellipsometer used in this study

The optical configuration of a rotating compensator ellipsometer (RCE) is shown in Figure 3.2 above. A halogen lamp is used in tandem with a deuterium source to provide illumination over a broad spectral range (240 – 920 nm). The state of polarization of the incident light beam is usually set by a polarizer, which is an optical system that converts a beam of light of any polarization state into a light beam with a single known polarization state. The polarizer yields a linearly polarized beam upon transmission through the polarizer. The analyzer is also a polarizer: it is used to resolve the polarization state of the light beam after reflection from the sample.[2] The compensator is an optical element that alters the phase of one polarization component of a light beam with respect to the other: it is often employed to convert linear polarization to circular polarization and vice-versa.[1] In the RCE design, all the Stokes parameters (vectors which describe the polarization state of electromagnetic radiation) can be obtained in a single measurement and thus the measurement ranges for (ψ, Δ) are not restricted but can be measured over the full range with uniform sensitivity.[1] The detectors use a fixed grating with a silicon CCD array to allow for fast data collection.

3.4 Data Analysis

In order to evaluate the optical constants and thickness of samples from reflectometry and SE, data analysis must be performed. This analysis consists of three main parts: dielectric function modeling, construction of an optical model, and fitting to the measured (ψ, Δ) and reflectometry spectra.

3.4.1 Dielectric Function Modeling

In the analysis of reflectometry and SE data, the dielectric function of a sample is required: if it is unknown, modeling of the dielectric function is necessary. In this study, the SCI™ dispersion model was used. It is a modified Lorentz oscillator model, which allows for coupling between the oscillators.[7] (The Lorentz oscillator model is described in chapter 1.) In the limit as the damping coefficient goes to zero, the SCI model converges to the Lorentz oscillator model.

3.4.2 Optical Model

The construction of the optical model is one of the most important steps in ellipsometry data analysis. The model is built using an estimated film thickness and the material optical characteristics. The resulting parameters are then considered to be the best estimate of the physical parameters, film thickness and material optical constants for each layer in the structure. The optical models used for the materials in this study are described in the experimental section of each chapter.

3.4.3 Data Analysis

Data analysis is performed using linear regression analysis and optical constants and film structure are determined by minimizing fitting errors calculated from a fitting error function. Figure 3.3 below shows the steps in the data analysis procedure.

First, an optical model corresponding to the sample is constructed and then

the dielectric functions of each layer are selected using a dielectric function model. Using analytical parameters, such as the high frequency dielectric constant, the damping coefficient, the center energy of each oscillator, the amplitude of each oscillator and the oscillator vibration (broadening) frequency, the calculated reflectance and (ψ, Δ) spectra are fitted to the experimental spectra. In the next step, the fitting error (called the root mean square error or RMSE) is evaluated. If it is too large, the analytical parameters are optimized and adjustments made to the optical model as necessary. Finally, from the optical model and analytical parameters that minimize the RMSE, the optical constants and thickness of each layer are determined. The quality of the fits was determined using the root mean square error (RMSE) which is calculated using the following formula:

$$\mathrm{RMSE} = \sqrt{\frac{\sum_{\mathrm{j=1}}^{\mathrm{n}} [(\mathrm{Y}_{\mathrm{target,\,j}} - Y_{calculated,j})^2 \, x \, weight_j^2]}{\sum_{j=1}^{n} weight_j^2}} \qquad (3.2)$$

The parameters are as follows: n is the number of selected targets, Y_{target} is the target value, $Y_{calculated}$ is the calculated (predicted) value, and *weight* is the standard deviation at each target point.[7] The weighting of each data point by its standard deviation ensures that noisy data points do not skew the results of the fit. Noisy data points will have larger standard deviation values so that their contribution to the RMSE tends to be smaller.[2] The smaller the RMSE value, the better the fit, with a perfect fit having an RMSE value of 0, i.e., no difference between the measured and simulated data.

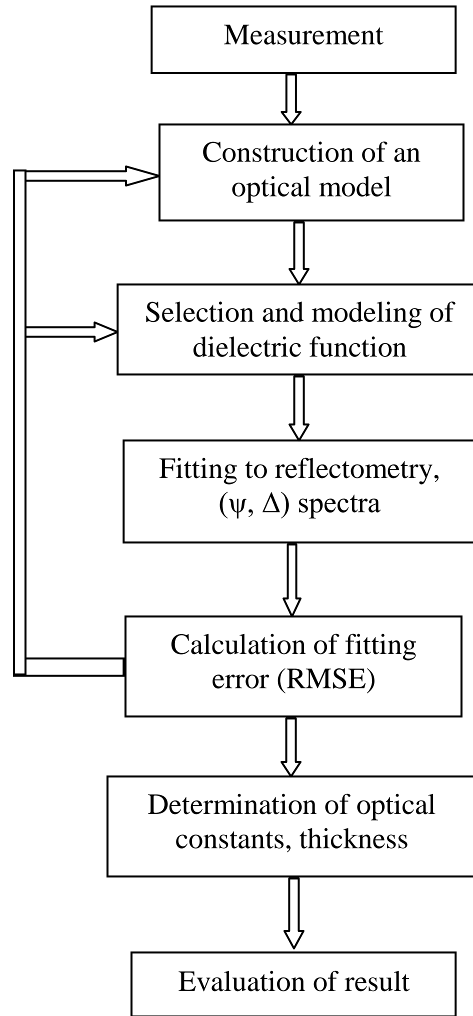

Figure 3.3: Flow chart showing the steps in the analysis of reflectometry and SE data.

It is important to evaluate the obtained results for reasonableness. An optical model approximates the sample structure and the obtained results are not necessarily correct even when the fit is good[1] (small RMSE values). If possible, the ellipsometry results can be validated using other measurement techniques such as scanning electron microscopy (SEM) and atomic force microscopy (AFM). An example of this approach is demonstrated with the analysis of zinc oxide thin films in chapter 4 of this study.

References

1. Fujiwara, H., *Spectroscopic Ellipsometry Principles and Applications*. John Wiley and Sons, Ltd.: 2007.

2. Tompkins, H. G.; McGahan, W. A., *Spectroscopic Ellipsometry and Reflectometry: A User's Guide*. John Wiley and Sons, Inc.: 1999.

3. Vedam, K., Spectroscopic Ellipsometry: a Historical Overview. *Thin Solid Films* **1998,** 313-314, 1 - 9.

4. Aspnes, D. E., Expanding Horizons: New Developments in Ellipsometry and Polarimetry. *Thin Solid Films* **2004,** 455-456, 3-13.

5. Hilfiker, J. N.; Hale, J. S.; Johs, B. D.; Tiwald, T. E.; Synowicki, R. A.; Bungay, C. L.; Woolam, J. A., Spectroscopic Ellipsometry in Optical Coatings Manufacturing. *Society of Vacuum Coaters* **2001,** 505, 295-300.

6. Azzam, R. M. A.; Bashara, N. M., *Ellipsometry and Polarized Light*. 2nd ed.; North Holland Press, Amsterdam: 1987.

7. SCI, *FilmTek (TM) 3000SE Operations Manual*. Scientific Computing International: 2006.

CHAPTER 4: Optical Properties of Zinc Oxide Thin Films

4.1. Introduction

There has been great interest in thin film piezoelectric materials such as zinc oxide for wide ranging applications such as thin film resonators in wireless communication devices,[1] as ultraviolet light emitting devices,[2-4] as material for thin film solar cells[5] and as optical coatings,[6] to give a few examples. Precise knowledge of the optical properties is crucial for designing modern optical and optoelectronic devices but so far, only a few studies have been done on the optical properties of ZnO crystals and films and many discrepancies remain among the various studies.[4-11] Additionally, research in this area has focused on films grown by molecular beam epitaxy (MBE) and pulsed laser deposition (PLD). Sputtering as an alternative deposition method offers several advantages: low deposition temperatures are possible, high deposition rates on amorphous substrates, preferred orientation of the materials deposited and large deposition areas.[12] Films grown by sputtering therefore could potentially be used for large scale applications,[11] such as solar cells, if their optical properties were well understood. Previous studies have concluded that the structure, surface morphology, composition and optical properties of thin films are strongly dependent on substrate temperature. Thus a study of optical properties with varying substrate temperature will add important information to the body of knowledge in this field.

Reflectometry and spectroscopic ellipsometry (SE) are fast, non-contact, non-destructive tools which are very sensitive to surface layers and thus ideal for

analyzing thin films. Ellipsometry is widely used in the semiconductor industry for example, for process control: pairing the technique with reflectometry results in far fewer systematic errors and thus more reliable results than could be obtained using SE only.

We report for the first time the optical properties of zinc oxide thin films deposited at varying substrate temperatures analyzed by spectroscopic ellipsometry and reflectometry using a coupled Lorentz oscillator model which is able to fit the experimental data both above and below the band gap of the material. The films were deposited by radio frequency (RF) magnetron sputtering on silicon and platinum-coated silicon substrates.

4.2. Structure and Properties of Zinc Oxide

Zinc oxide (ZnO) is a member of the wurtzite family whose characteristic features include a non-centrosymmetric structure and polar crystallographic surfaces. The structure may be described as a number of hexagonal alternating planes composed of tetrahedrally coordinated O^{2-} and Zn^{2+} ions stacked alternately along the *c*-axis (Figure 4.1).

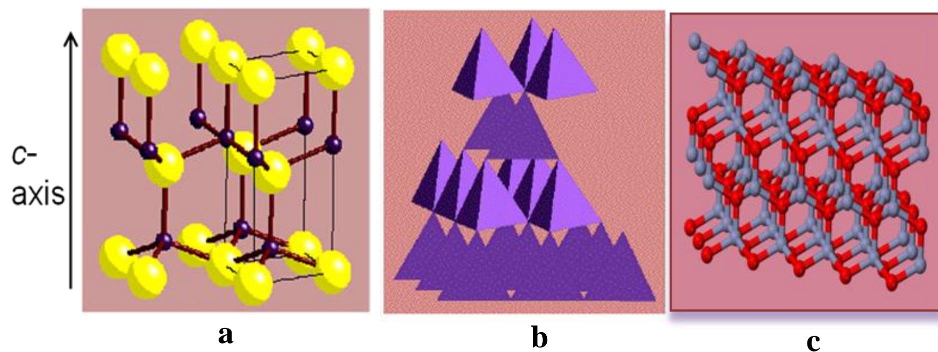

Figure 4.1: Structure of Zinc Oxide (a) ball-and-stick representation; (b) polyhedral representation (c) ball-and-stick representation showing hexagonal structure

ZnO exhibits a number of interesting properties which makes it an excellent candidate for applications in diverse fields. It is a multifunctional II-VI, n-type, direct-gap semiconductor with wide bandgap energy (3.37 eV) and a high excitonic binding energy (60 meV).[11,13] These properties make it of considerable interest for both electrical and optical applications: Bagnall et al[2] and Tang et al[3] have demonstrated optically pumped ultraviolet lasing at room temperature from ZnO films grown by molecular beam epitaxy. It is also an important transparent conductive oxide, exhibiting high transmittance in the visible region (~85%)[13] and low electrical resistivity ($10^{-4} – 10^{-2}$ Ω cm),[13] making it an ideal material for solar cells and flat panel displays.[6] Due to the non-centrosymmetric structure,

ZnO is piezoelectric, a key property in making it useful for electromechanical coupled sensors and transducers.[11]

4.3. Experimental

4.3.1. Preparation of Zinc Oxide Thin Films

ZnO films were deposited using radio frequency (RF) planar magnetron sputtering equipment (ANELVA SPF-332H) a schematic of which is shown in Figure 4.2. This system consists of a cryogenic vacuum pump which achieves a base pressure of less than 5 x 10^7 torr, a RF power supply (13.56 MHz) with a matching unit, a 3 inch diameter coaxial planar magnetron under the target holder, argon (Ar) and oxygen (O_2) gas inlets and quartz lamps for substrate heating. A 3 inch diameter Zn target (99.995% Pure Tech Inc. 0.125 inch thickness) was reactively sputtered in an Ar-O_2 (1:1) plasma discharge at 5 sccm flow rates for each gas with varying chamber pressures. A 4-inch main butterfly valve controls the total pressure in the system during deposition. High purity gases (Ar and O_2) were premixed and introduced into the system. The flow rates were adjusted by manual leak valves and measured using Matheson flow meters. The total working pressure in the system was measured with a MKS Baratron capacitance gauge.

Two types of substrates were used in this process: Si (100) wafers bearing a native oxide layer and Pt (111) on Si. Before deposition onto the substrates, the target was pre-sputtered for 10 minutes. During this period, the deposition of ZnO on the substrate was prevented by the presence of a shutter. After pre-sputtering, the shutter removal changed the plasma impedance, requiring the retuning of the RF power source from the matching unit to optimize the sputtering process. During sputtering, the substrates were placed parallel to the target surface in a sputter-down geometry. The substrates were either intentionally heated with

a quartz lamp to temperatures varying from 300 – 700 °C, or unintentionally heated to a temperature ranging from 45 – 65 °C due to energetic particle bombardment. The substrate temperature was measured by a thermocouple situated below and in contact with the substrate. The target substrate distance was 9.5 mm.

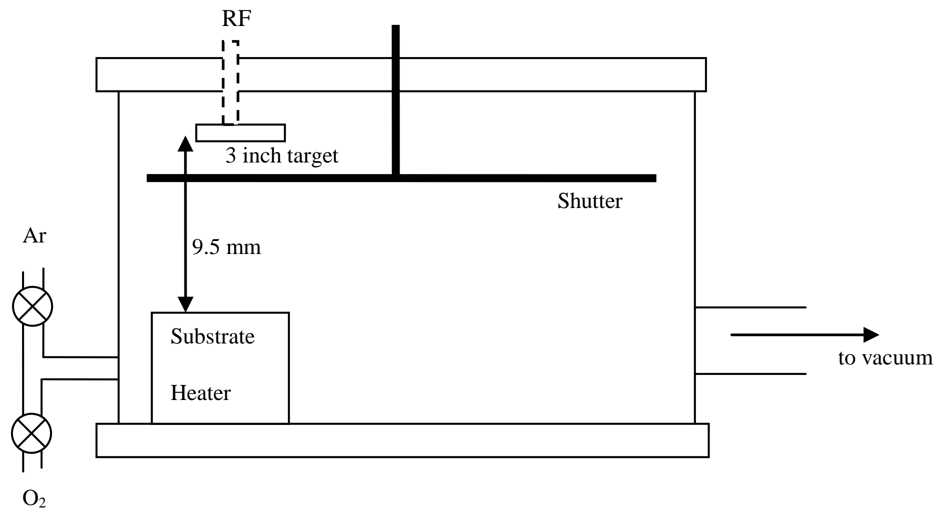

Figure 4.2: Schematic of the Anelva SPF-332H sputtering system

4.3.2. Determination of Optical Properties

The optical properties of the films were measured by multi-angle spectroscopic reflectometry and spectroscopic ellipsometry on a FilmTek™ 3000SE optical thin film metrology system (Scientific Computing International). Details of the experimental setup and procedure are given in chapter 3.

4.4. Results

4.4.1. Reflectometry and Ellipsometry Data

4.4.1.1. ***Film Structure and Model Parameters***.

The film deposited on silicon was modeled as three layers consisting of the substrate (silicon), a zinc oxide layer and a zinc oxide/void EMA layer to account for any surface roughness (Figure 4.3A(i)). The film deposited on platinum was modeled as three layers consisting of the substrate (platinum), a zinc oxide layer and a graded zinc oxide/void EMA layer to account for any surface roughness (Figure 4.3A(ii)). The zinc oxide layer was modeled using the SCI™ dispersion model which is a generalized Lorentz oscillator model which allows for coupling between the oscillators. In the limit as the damping coefficient goes to zero, the SCI model converges to the Lorentz oscillator model. The zinc oxide/void layer was modeled using an effective medium approximation (EMA) using the Bruggeman model. This model is based on the self-consistent choice that the dielectric function of the total system equals the dielectric function of the host material which in this case is zinc oxide.[17]

Figure 4.3A: Optical model used in analysis of (i) ZnO on Si and (ii) ZnO on Pt thin films

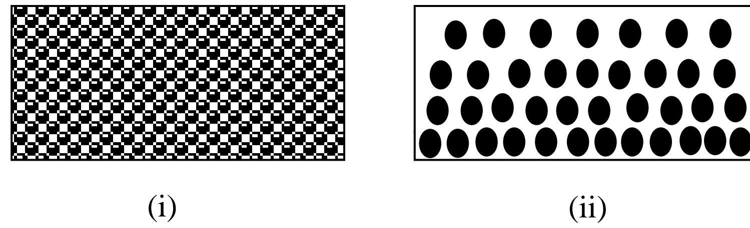

Figure 4.3B: Optical Model of EMA layer for film deposited on Si with ZnO: void = 50:50 (i) and Pt with graded model (ii). Black spheres represent ZnO

The reflectometry and SE data was then analyzed using a multiple parameter regression analysis. The model used two oscillators for the films deposited on silicon and three oscillators for the films deposited on platinum and varied the following parameters: the high frequency dielectric constant; the damping coefficient; the center energy of each oscillator; the amplitude of each oscillator and the oscillator vibration (broadening) frequency.

4.4.1.2. *Sample Reflectance and Ellipsometric Data and Dispersion Spectra*

Figure 4.4 (a –d) shows typical measured and simulated reflectometry and ellipsometry data for a zinc oxide film grown on a silicon substrate at a deposition temperature of 500°C, as well as the refractive index and extinction coefficient dispersion spectra determined using the SCI ™ model. Table 4.1 shows the values of the fitted parameters as well as the thickness, refractive index and extinction coefficient obtained at 632 nm and the RMSE value of the data fits. A summary of the results obtained for the analyzed films is shown in Tables 4.2 and 4.3 below. Appendix A contains all the data sets analyzed in this manuscript.

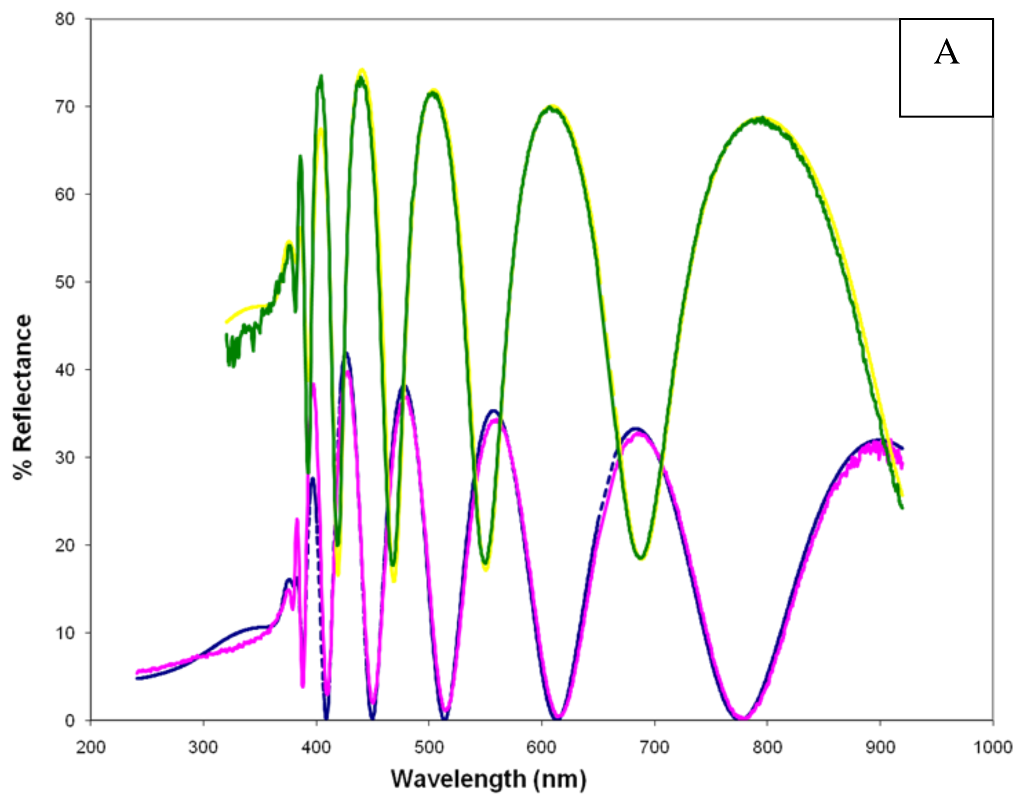
A
80
70
60
50
40
30
20
10
0
200
300
400
500
600
700
800
900
1000
% Reflectance
Wavelength (nm)

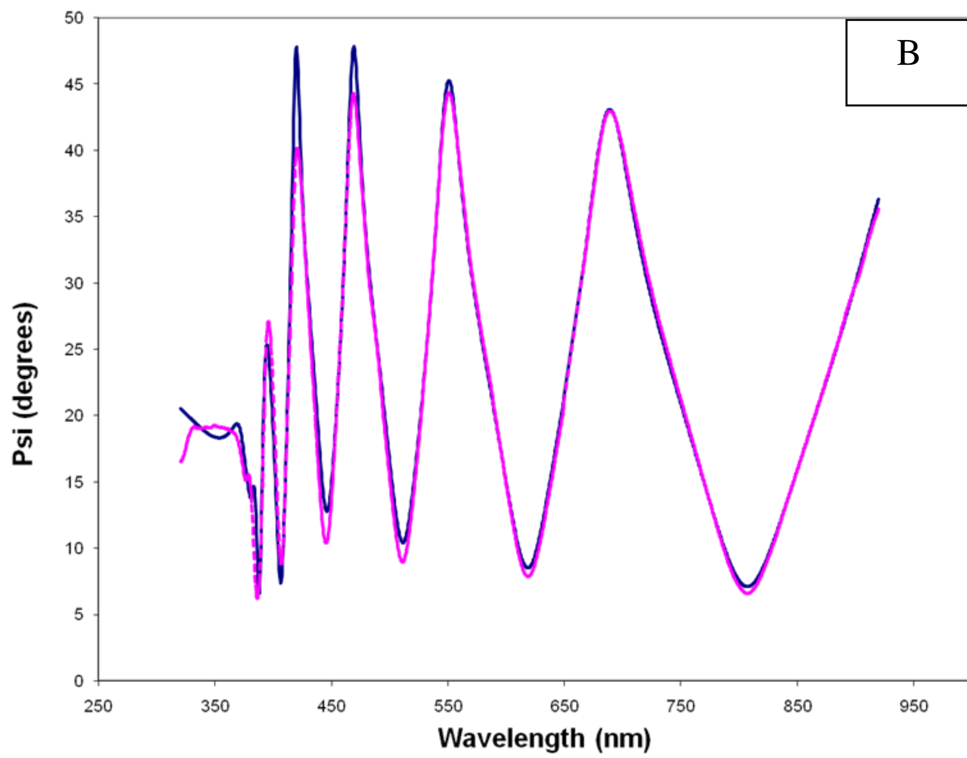
B
50
45
40
35
30
25
20
15
10
5
0
250
350
450
550
650
750
850
950
Psi (degrees)
Wavelength (nm)

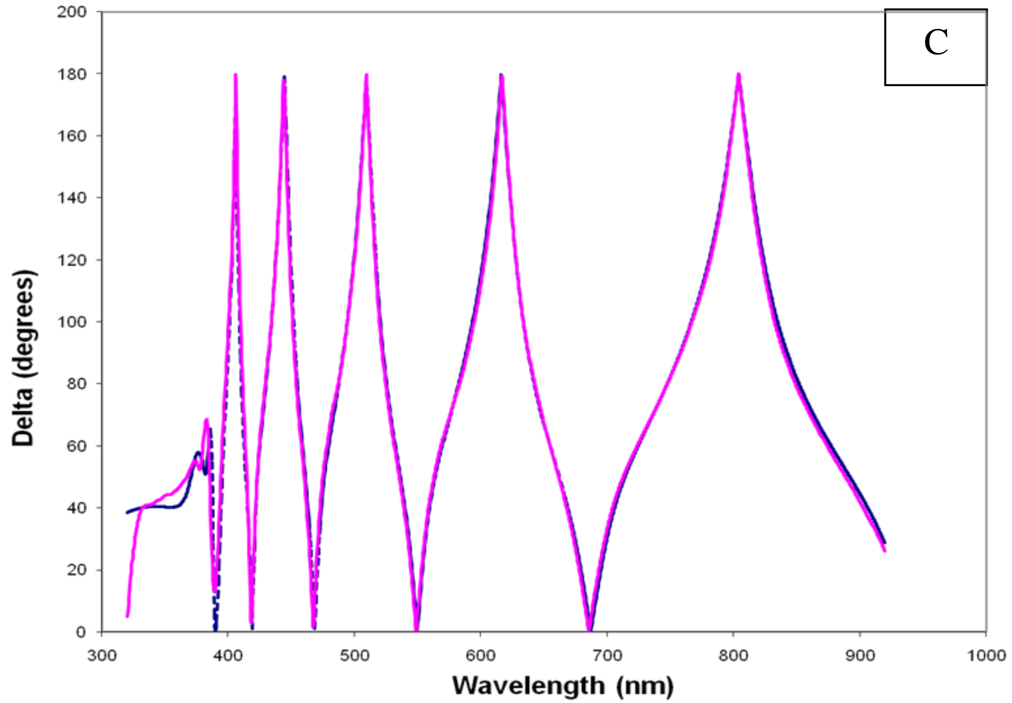

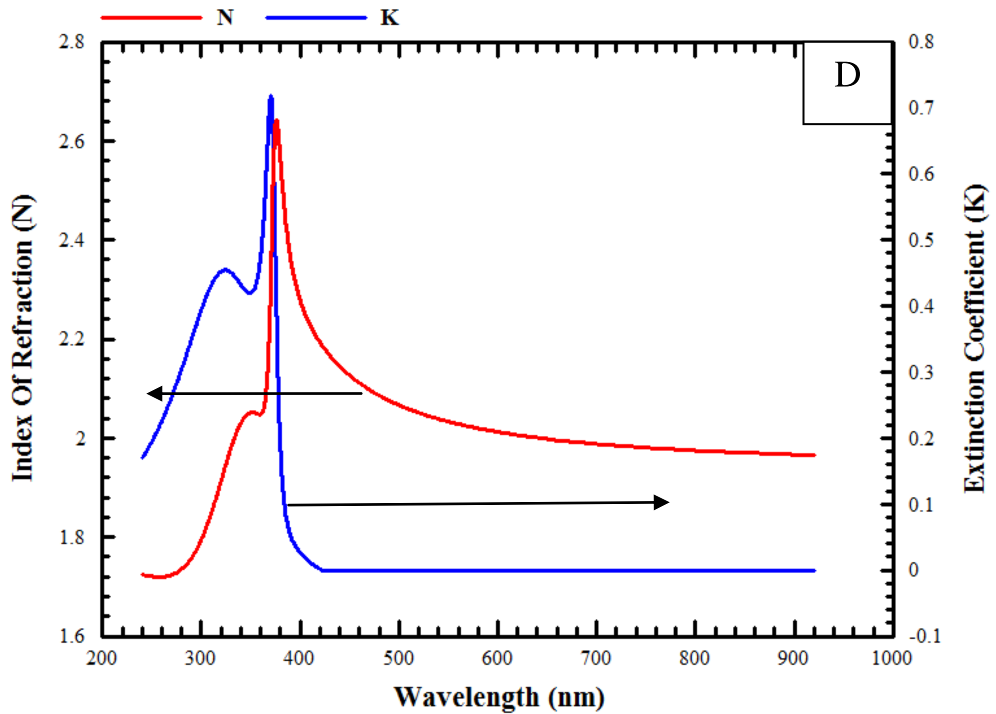

Figure 4.4: (a) Measured (violet) and simulated (blue) 0° and measured (green) and simulated (yellow) 70° reflectance (b) Measured (violet) and simulated (blue) psi (ψ) (c) Measured (violet) and simulated (blue) delta (Δ) (d) index of refraction (n) and extinction coefficient (k) dispersion spectra for 0.675 μm ZnO film deposited at 550°C on Si substrate

Table 4.1: Regression Parameter Data and Extracted Optical Constants for fits shown in Figure 4.4

Layer #1 Material Coefficient Table	
Number of Oscillators	2
High Frequency Dielectric Constant	3.201437
Damping Coefficient	2.434038
Amplitude (1)	0.512585
Center Energy (1)	3.321930
Vibrational Frequency (1)	0.107968
Amplitude (2)	1.406792
Center Energy (2)	3.695282
Vibrational Frequency (2)	1.115256
Layer #2 Material Coefficient Table	
EMA Screening	0.3333
EMA Type	Bruggeman
Number of Materials	2
% Same As Layer #1	50.0000
% VOID	50.0000
Extracted Data	
Thickness Layer 1	675.18 nm ± 0.05 nm
Thickness Layer 2	20.57 nm ± 0.05 nm
Refractive Index @ 632 nm	2.03348 ± 0.00020
Extinction coefficient @ 632 nm	0.0000
RMSE	1.590

Table 4.2: Summary of Data for ZnO Thin Films on Silicon Substrate

Sample ID	Deposition Temperature/°C	Thickness Layer 1/nm ± 0.05 nm	Thickness Layer 2/nm ± 0.05 nm	Refractive Index, n @632 nm ± 0.00020	RMSE
GM30-a	100	671.46	16.94	1.98328	1.277
GM13-g	400	402.28	12.93	2.01218	0.974
GM29-3	450	646.95	12.47	2.02177	1.449
GM17'-a	550	675.18	20.57	2.03348	1.590
GM25-2	600	643.34	14.61	2.03629	1.473

Note: k = 0 at 632 nm for all films

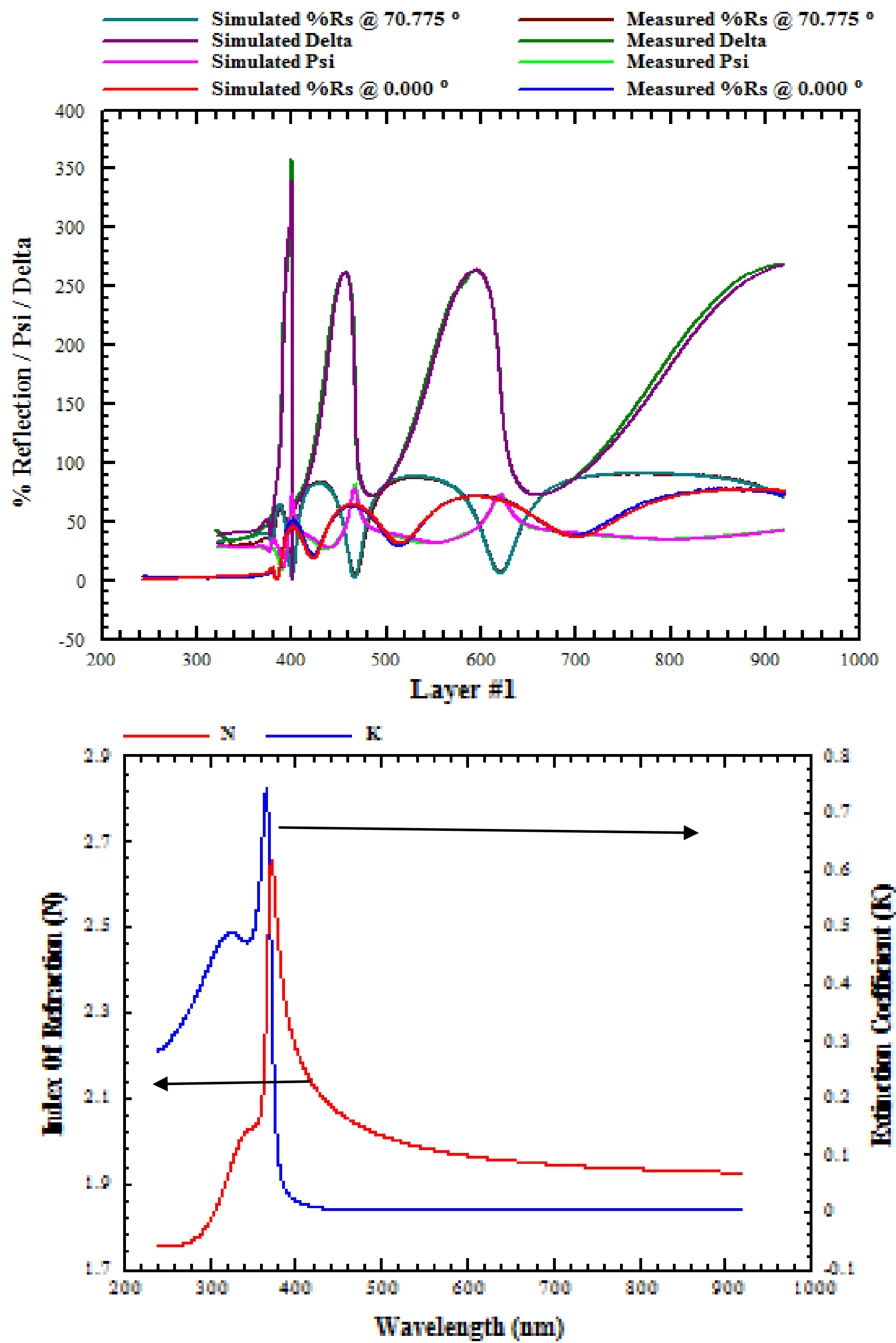

Figure 4.5: (Top) Measured and simulated 0°, 70°, reflectance , psi (ψ) and delta (Δ) data (Bottom) index of refraction (*n*) and extinction coefficient (*k*) dispersion spectra for ~ 0.65 μm ZnO film deposited at 500°C on Pt substrate

Table 4.3: Regression Parameter Data and Extracted Optical Constants for fits shown in Figure 4.5.

Layer #1 Material Coefficient Table	
Number of Oscillators	3
High Frequency Dielectric Constant	1.000000
Damping Coefficient	0.886088
Amplitude(1)	14.251682
Center Energy(1)	9.532871
Vibrational Frequency (1)	22.709711
Amplitude(2)	0.994141
Center Energy(2)	3.356137
Vibrational Frequency (2)	0.119004
Amplitude(3)	2.023066
Center Energy(3)	3.667778
Vibrational Frequency (3)	0.970417

Layer #2 Material Coefficient Table	
EMA Screening	0.3333
EMA Type	Landau-Lifshitz
Number Nodes	3
HOST MATERIAL	Same As Layer #1
Material #2	VOID
% POSITION NODE #1	0.00
% POSITION NODE #2	50.00
% POSITION NODE #3	100.00
% FRACTION VOID NODE #1	0.0000
% FRACTION VOID NODE #2	79.3708
% FRACTION VOID NODE #3	67.0000

Table 4.4: Summary of Data for ZnO Thin Films on Platinum Substrates

Sample ID	Deposition Temperature /°C	Thickness ZnO layer /nm ± 0.05 nm	Thickness Graded EMA layer /nm ± 0.05 nm	Refractive Index, *n* ± 0.00020	RMSE
GM30a	100	653.46	61.69	1.94547	2.828
GM11b	400	623.67	62.66	1.95369	3.463
GM10b	500	413.34	55.25	1.95766	1.994
GM17a	550	636.24	63.21	1.97558	3.726
GM19c	650	875.80	35.31	1.97995	4.063
GM20r	700	685.61	49.44	1.99080	3.980

Note: $k = 0$ at 632 nm for all films

Table 4.5: Comparison of RMSE Values for Various Models used to fit ZnO Thin Films on Platinum Substrates

Sample ID	Deposition Temperature/°C	Root Mean Square Error, RMSE		
		EMA 50:50 ZnO: void	EMA estimated by AFM	Graded Model
GM30a	100	3.886	7.498	2.828
GM11b	400	3.479	7.177	3.463
GM10b	500	2.541	4.775	1.994
GM17a	550	5.825	6.639	3.726
GM19c	650	4.039	4.392	4.063
GM20r	700	4.116	7.055	3.980

4.4.2. Atomic Force Microscopy

Atomic Force Microscopy (AFM) images were collected on a Thermo-Microscopes™ Explorer AFM instrument scanning in contact mode using a silicon nitride tip with a nominal radius of 20 nm. Images were processed by two-dimensional, second order leveling and analyzed to obtain area roughness, line roughness and peak-valley height measurements using the instrument software (ThermoMicroscopes™ SPMLab Version 5.01).

Figure 4.6: AFM images (left: 5 µm^2 and right: 1 µm^2) of ZnO thin films on Pt at deposition temperature (A) 100 °C; (B) 550 °C; (C) 650 °C.

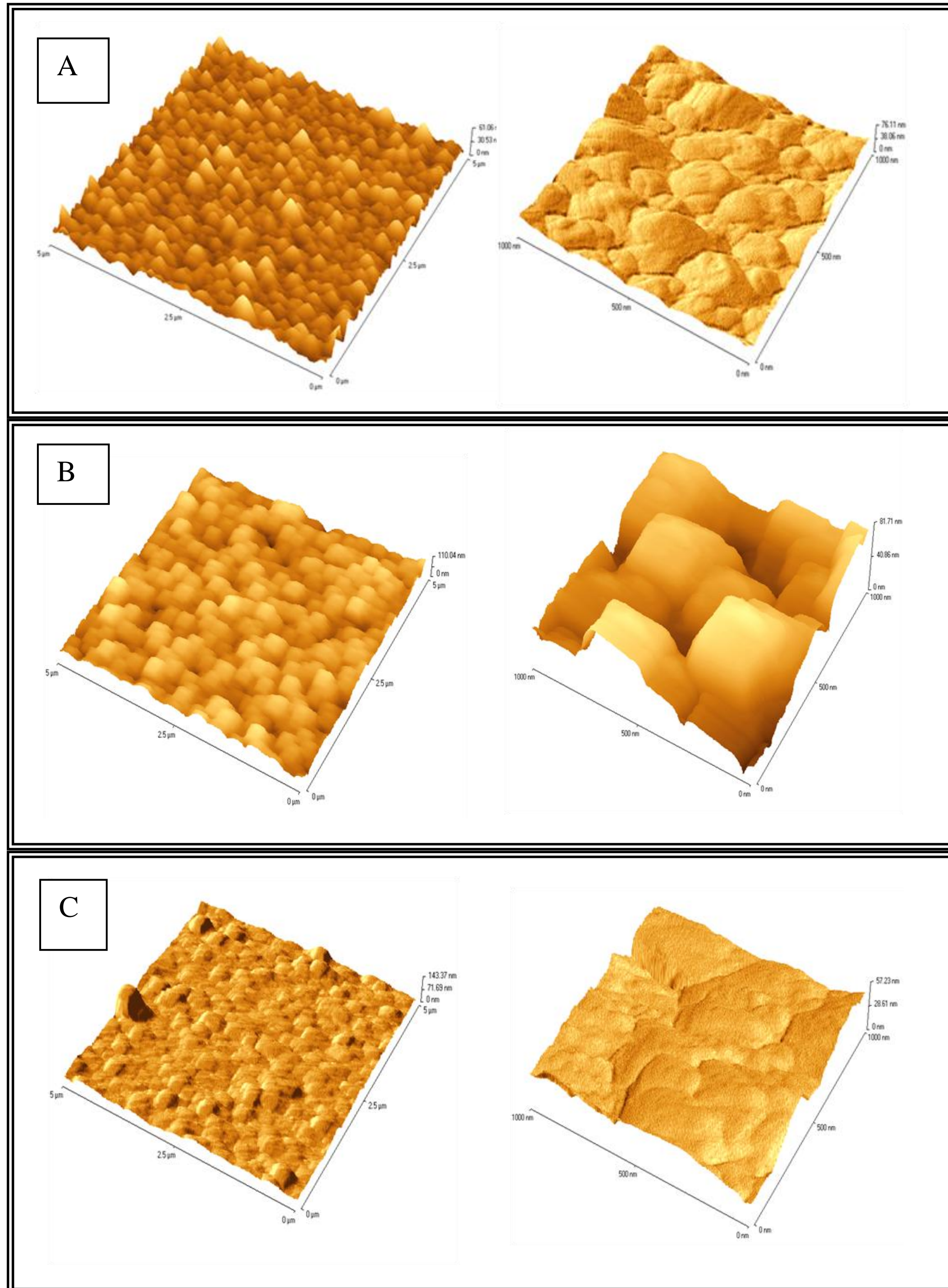

Table 4.6: AFM Analysis: Roughness, R_a and Averaged Peak-Valley Height for images

AFM Analysis Type		Deposition Temperature / °C		
		100	550	650
Line R_a / nm	1 μm^2	6.29	14.42	6.04
	5 μm^2	5.08	11.63	8.35
Area R_a / nm	1 μm^2	8.21	14.32	8.83
	5 μm^2	6.16	11.97	9.26
Average Peak-Valley Height/ nm	1 μm^2	13.62	17.83	12.41
	5 μm^2	9.12	18.16	12.95

R_a is the roughness average and is the arithmetic average of the absolute values of the measured profile height deviation calculated as follows:

$$R_a = \frac{1}{n}\sum_{i=1}^{n}|Z_i - \overline{Z}|$$

4.4.3. Scanning Electron Microscopy (SEM) Images

Scanning Electron Microscopy (SEM) images were collected on a Digital Scanning Microscope, DSM 940 (Zeiss) at a voltage of 15 kV and a working distance of 11 mm.

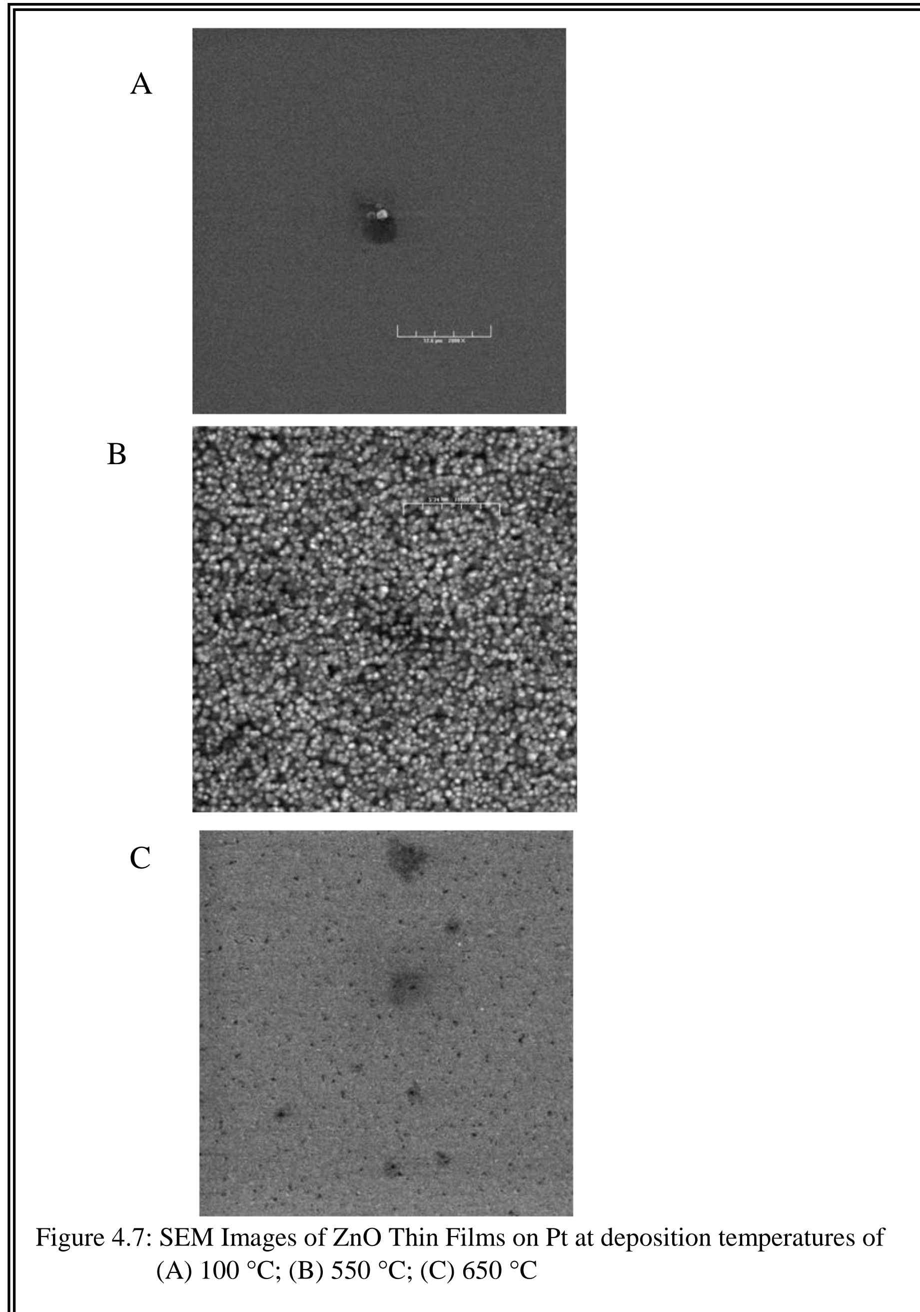

Figure 4.7: SEM Images of ZnO Thin Films on Pt at deposition temperatures of (A) 100 °C; (B) 550 °C; (C) 650 °C

4.5. Discussion

The quality of the fit of the data to the model used is amply demonstrated by the close match of the simulated data to the measured spectra: the RMSE obtained for the fits in Figure 4.4 was 1.437 over all four data sets, both above and below the ZnO band edge. The average RMSE for the fits on silicon was 1.353 (five films), while the average for the fits on platinum was 3.342 (six films). As a comparison, the best fits obtained for SiO_2 on Si, one of the best understood systems in terms of optical behavior, is between 0.5 – 1.0. Average RMSE values of 1.353 and 3.342 therefore amply demonstrate the excellent fitting capabilities of the model.

The optical spectra show strong interference oscillations below the band edge (~375 nm) due to multiple internal reflections between the film and the substrate. Above the band edge (wavelengths below 375 nm), no oscillations are seen due to light absorption resulting from the ZnO interband transition. The *n* and *k* spectra show strong peaks which may be attributed to ZnO interband transitions (375 nm) as well as a smaller, broadened peak (338 nm) attributed to exciton-phonon complex transitions.[4] The value of the extinction coefficient is seen to be zero between 400 – 920 nm, indicating that the ZnO film is transparent in this spectral region. Therefore, in this region, the refractive index of ZnO can be modeled using the simple empirical Cauchy dispersion model:

$$n(\lambda) = n_0 + \frac{n_1}{\lambda^2} + \frac{n_2}{\lambda^4}$$

The dispersion obtained for the index of refraction is typical of semiconductors, showing *n* decreasing with increasing wavelength and a resonant frequency close

to the visible region (370 nm).[14] Similar behavior is observed for films deposited on platinum.

Figure 4.8 below shows a plot of (a) refractive index versus deposition temperature and (b) EMA layer thickness versus deposition temperature for films deposited on silicon substrates. The films have a zinc oxide layer thickness of 650 nm ± 30 nm (with the exception of one film). The results indicate a general trend of n increasing with increasing deposition temperature. Since n is an indicator of packing density,[11] it may be surmised that increasing substrate temperatures result in the increased mobility of species impinging on the surface. As such, the atoms have sufficient energy to assemble into a regular lattice structure and thus increasing deposition temperatures result in a lattice structure that approaches that of the bulk material.[12,15] Refractive index can also be used as an indicator of film stoichiometry: index increases with an increase in the O/Zn ratio. Since electrical measurements also indicate that the films are nearly insulating, this trend indicates that the film stoichiometry is close to ZnO, i.e. 1:1 ratio of Zn to O and therefore little interstitial zinc which would give rise to n-type conductivity in the films. EMA thicknesses show no correlation to temperature. As discussed later in this manuscript with respect to the films deposited on platinum, while it may be expected that at higher deposition temperatures the roughness of the films would increase, the values obtained from the reflectometry/SE analysis are consistent with the physical estimates obtained from AFM measurements. Additionally, the film deposited at 550 °C on platinum showed faceting[16] and this is the film on silicon for which the highest EMA value is obtained.

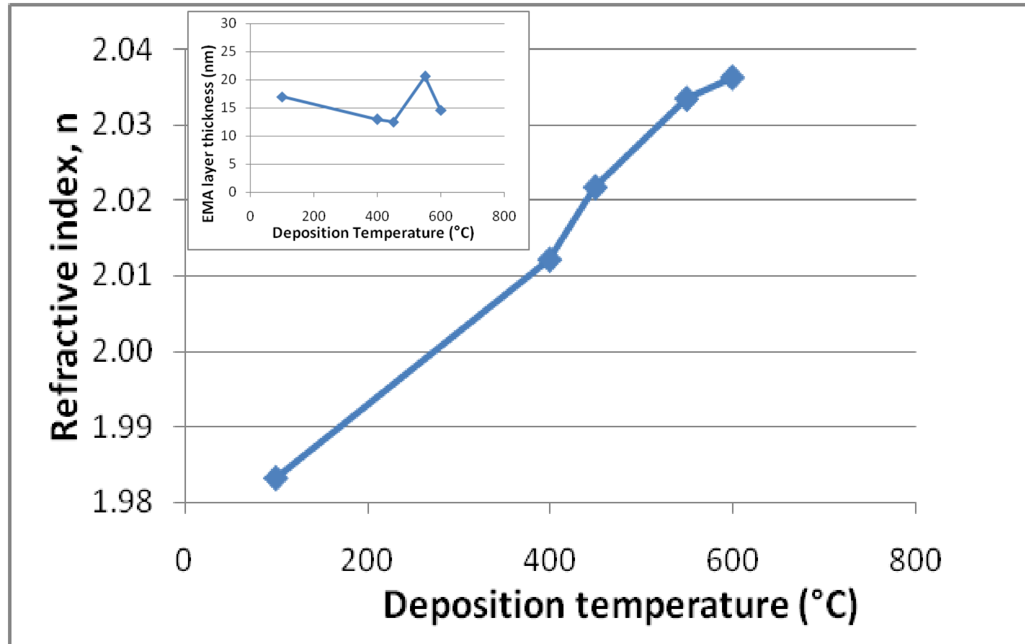

Figure 4.8: Refractive index (n) and EMA layer thickness in nm (inset) vs. deposition temperature (°C) for ZnO thin films on silicon substrate

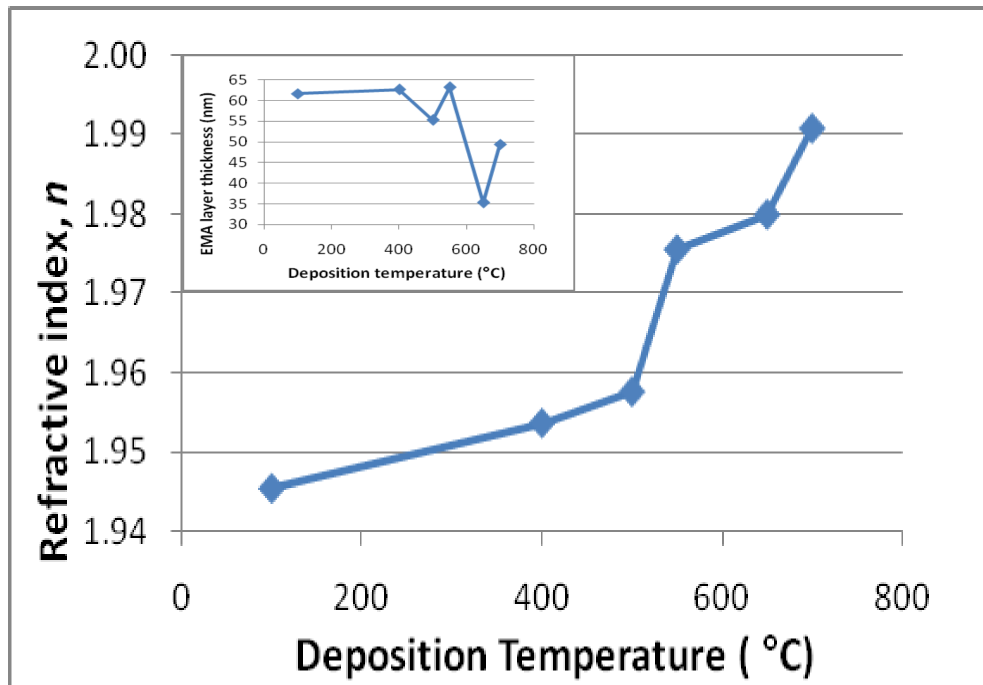

Figure 4.9: (a) Refractive index (n) and EMA layer thickness in nm (inset) vs. deposition temperature (°C) for ZnO thin films on platinum substrate

Figure 4.9 shows a plot of refractive index versus deposition temperature and (b) EMA layer thickness versus deposition temperature for films deposited on platinum substrates. Four of the films on platinum have a zinc oxide thickness of approximately 650 nm; the remaining two have thicknesses of 413 and 875 nm. The ellipsometry-reflectometry model appears to overestimate the thickness of the EMA layer based on the evidence of field effect scanning electron microscopy (FESEM) images[16] and scanning electron microscopy (SEM) images (Figure 4.7). Both types of imaging indicate that the films deposited at low temperatures (below 300 °C) are relatively smooth and that faceting occurs on the platinum-substrate films at 550 °C resulting in much greater roughness in films deposited at temperatures above 500 °C. To obtain a physical estimate of the film roughness, atomic force microscopy (AFM) imaging of the films were carried out in contact mode using 20 nm silicon nitride tips. The images of the films deposited at 100, 550 and 650 °C are shown in Figure 6 along with area and line roughness values (R_a) as well as average peak-valley heights in Table 4.6. Figure 4.10 below plots the roughness values versus deposition temperature: it is immediately obvious that the film deposited at 550 °C is much rougher than the ones deposited at 100 and 650 °C which have similar roughness. This result correlates well with what is observed visually from the FESEM and SEM data.

The average peak-valley height measurement was first used as a physical estimate of the film roughness and input as a non-varying parameter in the ellipsometry-reflectometry analysis. However, this approach yielded

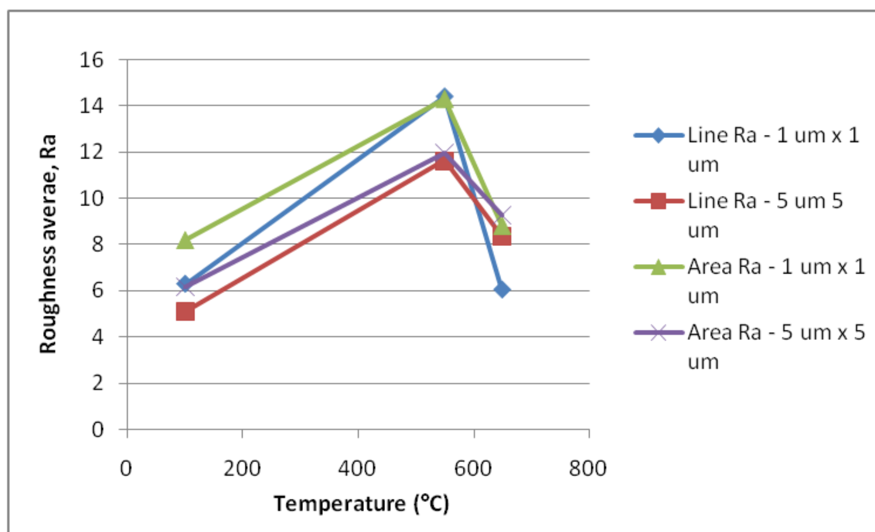

Figure 4.10: Roughness average, R_a vs. deposition temperature (°C) for ZnO films on platinum

unsatisfactory fits and refractive index values. Closer inspection of the AFM images revealed why this might be so: the zinc oxide material is not uniformly distributed throughout the roughness layer, as is assumed by the Bruggeman EMA. Instead, the proportion of ZnO decreases and the proportion of void increases as we move from the bottom of the EMA layer toward the top, as illustrated in Figure 4.3B. Based on this observation, a graded index was used to describe the EMA layer in the reflectometry-ellipsometry model.

The graded material model is similar to the EMA in that it is a mixture of two materials. However, in the graded model, the mixture ratio is specified at different depths within the layer (i.e., models an inhomogeneous layer) and the index of refraction is graded in the direction perpendicular to the surface of the film. The mixture ratio is assumed to be a linear interpolation of the mixture ratios at the specified nodes.[17] Using this approach the data obtained and the RMSE of the fits are shown in Table 4.4. Excellent fits were obtained using the graded

model compared with a simple EMA (50:50 ratio of ZnO: void distributed homogeneously throughout the layer) or fixing the EMA layer thickness based on the AFM as a non-varying parameter in the model. The RMSE of all three approaches are summarized in Table 4.5. As can be seen from the data in the table, the graded EMA consistently gives better RMSE values than the other two models, indicating better fits of the measured to simulated data. The EMA thicknesses obtained from the graded model are also consistent with the AFM data: for example, for the sample deposited at 100°C, the AFM gives values of 61.06 nm and 76.11 nm for the 1 μm^2 and 5 μm^2 scan areas respectively, which compares very well with 61.69 nm from the reflectometry-ellipsometry model.

As with the films deposited on silicon, the films deposited on platinum show an increase in the refractive index with increasing deposition temperature. The same arguments can be made to explain this trend. A survey of the literature reveals many reports that show that the crystallinity of zinc oxide thin films increase with increasing substrate temperatures. Çetinörgü et al[18] studied films deposited by filtered vacuum arc deposition (FVAD) on microscope glass and UV-fused silica and concluded that the film grown at a substrate temperature of 400 °C was more crystalline, had larger grain sizes, higher surface roughness and higher resistivity than films grown at room temperature based on XRD, AFM and X-ray photoelectron spectroscopy (XPS) measurements. Transmission and SE measurements found that the optical transmission of the films were also increased at higher substrate temperatures, however, the refractive index of the film deposited at 400 °C was 10 % lower than that deposited at room temperature.

Kang and Joung[12] studied films deposited on $Pt/TiO_x/SiO_2/Si$ by RF magnetron sputtering at substrate temperatures varying from 100 – 400 °C. Their study found that the film deposited at 200 °C had the highest crystallinity based on full width at half maximum (FWHM) of the XRD peaks, AFM and SEM measurements. Using transmittance and reflectance data, they also concluded that the more crystalline film had a higher index of refraction. Hu et al[5] studied ZnO films deposited on α-SiO_2 substrate by PLD at substrate temperatures ranging from 225 – 500 °C. Unlike Kang and Joung's study, they found a decrease in FWHM values, indicating higher crystallinity with increasing substrate temperatures, albeit using different deposition methods. While transmittance measurements were used to determine the refractive index of the film deposited at 425 °C, no comparison of *n* was made at the various deposition temperatures. Similarly, Heitsch et al,[19] Kim et al[20] and Singh and Major[21] all observed an increase in grain size and crystallinity with increasing substrate temperature using different deposition techniques (PLD, MOCVD and RFMS respectively) on different substrates (Si (111 and 100), SiO_2 and fused quartz respectively) using a variety of measurement techniques (XRD, SEM, AFM and Raman).

However, no studies have explicitly examined the relationship between substrate temperature and refractive index on any substrate using SE or, as in our case, the combination of reflectometry and SE. Table 4.7 summarizes previous studies carried out on the optical properties of ZnO crystals and thin films using spectroscopic or transmission ellipsometry. The studies by Washington[4] and Hu[5] used the Sellmeier and Cauchy models respectively but were only able to fit below

the band gap of ZnO. Liu[6,34] and Dumont[7] were able to fit over the whole range but only by using one of the above two models below the band gap and using more complex computational methods above the band gap. Rebien[11] did not specify the optical model used to fit their data: the emphasis of the study was to compare sol-gel deposited films to sputtered films. Additionally, all the studies cited deposited the film at only one substrate temperature with the exception of Hu, who deposited over the temperature range of 225 – 500 °C. However, Hu's study only measured the refractive index for the deposition temperature that was determined to give the most crystalline material (425 °C). Only the studies by Jellison[8] (on ZnO single crystal) and Hu gave quantitative values for the refractive index: all the other studies presented the dispersion spectra obtained and compared them qualitatively to other published work or to ZnO bulk values.

This study has therefore been able to accomplish two things. First, we have developed an optical model that has been able to give excellent fits to the measured data both above and below the band gap without resorting to more complex computational or point-by-point fitting methodology. Secondly, we have determined the refractive index for films deposited over a wide range of substrate temperatures. Thus we have been able to demonstrate that the correlation between substrate temperature and crystallinity also extends to refractive index and that the refractive index of ZnO for optoelectronic applications can be tailored by substrate temperature selection.

Table 4.7: Comparison of previous studies on Optical Properties of Zinc Oxide Crystal and Thin Films

Reference	Sample Type	Substrate	Technique	Substrate Temperature (°C)	Optical Method: Model(s) Used	Measurement Range (nm)	Refractive index, *n*
Bond 1965[22]	Single crystal	-	Vapor transport	-	Prism: Minimum deviation	400 - 4000	n_o = 1.9985 n_e = 2.0147 @ 600 nm
Park 1968[23]	Single crystal	-	Vapor transport		Transmittance: calc. from interference maxima		n_o = 2.232 @399.4 nm n_e = 2.237 @399.9 nm at 4.2 K
Matz & Luth 1979 [10]	Single crystal $(1\bar{1}00)$	-	Vapor transport	-	-	310 - 827	1.96 @ 600 nm (est.)
Inukai 1995[24]	Film	Glass	RFMS	300	Prism-coupling method	?	1.990 @ ?
Gupta 1996[25]	Film	Quartz	RFMS	RT then annealed @ 673 K	Transmittance: Swanepol method	300 - 900	1.998 @ 700 nm
Hu 1997[5]	Film	(001) α-SiO_2	PLD	225 - 500	SE: Cauchy (< band gap)	350 – 900	1.96 @ 633 nm for 425 °C film
Jellison 1998[8]	Single crystal	-	Vapor transport	-	SE: Lorentz oscillator	250 - 850	1.997 @ 600 nm
Washington 1998[4]	Film	(0001) Al_2O_3	PLD	800	Sellmeier (< band gap)	250 - 932	Consistent with Hu
Dumont 1999 [7]	Film	Glass	RFMS	20	Computation 310 – 500 Sellmeier 500 - 750	310 - 750	Compared qualitatively to other published results

Reference	Sample Type	Substrate	Technique	Substrate Temperature (°C)	Optical Method: Model(s) Used	Measurement Range (nm)	Refractive index, *n* reported
Sun 1999[26]	Film	Sapphire	PLD	500 - 800	Sellmeir < band gap	375 - 900	1.9777 @ 632.8 nm (calculated from fit)
Zayer 1999[27]	Film	Silicon	RFMS	100 - 300	SWE: quadratic model	Not stated	1.940 (wavelength not stated)
Postava 2000[28]	Film	Sapphire	RFMS	500	SE: Holden formula + Sellmeir term	206.6 – 1240 nm	Dispersion curves reported
Rebien[11]	Film	Fused silica	RFMS	RT	Not stated	275 - 1650	Close to bulk
Moustaghfir 2003[29]	Film	Glass slides	RFMS	RT	Swanepoel method	Not stated	1.88 – 1.96@ 632.8 nm
Ondo-Ndong 2003[30, 31]	Film	Glass	RFMS	100	Transmittance	300 - 900	1.95 @ 600 nm
Mehan 2004[32]	Film	Glass	RFMS	RT	Prism coupling method	-	1.9692 (n_0) @632 nm¶
Shan 2005[33]	Film	Glass	PLD	100 – 500	SE: Sellmeir	413 - 1770	1.9 – 2.1 @ 632.8 nm
Çetinörgü 2006[13]	Film	Glass, UV fused silica	FVAD	RT	Transmittance and SE: Tauc-Lorentz	250 - 1000	2.00 @ 500 nm
Liu 2006[34]	Film	(100) Si	FCVA	RT then annealed	SE: Cauchy + point-by-point fitting†	250 - 1100	*n* decreases with annealing
Liu 2006[6]	Film	(100) Si	FCVA	230	SE: Cauchy + point-by-point fitting†	250 - 1100	Similar to Rebien
Şenadim 2006[35]	Film	Glass	PFCVAD	25	Transmittance, reflection: Swanepoel and Kramers-Kronig	400 – 700	1.832 @ 500 nm

Reference	Sample Type	Substrate	Technique	Substrate Temperature (°C)	Optical Method: Model(s) Used	Measurement Range (nm)	Refractive index, n
Çetinörgü 2007[36]	Film	Glass, UV fused silica	FVAD	RT	Transmittance SE: Tauc-Lorentz	250 – 1000 191 – 989	1.87 – 2.03 @ 550 nm
Çetinörgü 2007[18]	Film	Glass, UV fused silica	FVAD	RT, 400	Transmittance SE: Tauc-Lorentz	250 – 1100	RT:1.87 – 2.03 400: 1.77 – 1.98@ 550 nm
Gioffre 2007[37]	Film	Si/SiO_2	RFMS	50	SE: Tauc-Lorentz	200 - 1700	~ 2.00 @ 600 nm (est)
Kang 2007[38]	Film	Pt(111)/TiO_x/ SiO_2/Si	RFMS	200	Transmittance: Swanepoel envelope method	350 - 1400	2.043@ 400 nm
Kang 2007[12]	Film	Pt(111)/TiO_x/ SiO_2/Si Quartz	RFMS	Variable	Transmittance: Swanepoel envelope method	350 - 1400	~ 1.95 @ 600 nm (est)
Khoshman 2007[39]	Amorphous thin film	Si (100), c-Si (100) Quartz	RFMS	< 52	SE: Cauchy-Urbach	330 - 1600	1.83 @ 450 nm 1.70 @ 800 nm
Kapoor 2008[40]	Thin film	Si (100)	PLD	25, 150, 300,400	SE: model not stated	Not stated	1.85 – 2.60 (wave-length range not stated)
This work	Thin film	Si (100) Pt(111) Ti/SiO_2/Si	RFMS	Variable	Modified Lorentz oscillator	240 – 920 nm	2.02717@ 632 nm 1.99080 @ 632 nm

* TE = transmission ellipsometry ‡ GE = generalized ellipsometry
†Cauchy 375 – 1100 nm, point-by-point fit 250 – 375 nm
¶ Assumed: study used He-Ne laser (usual operation wavelength 632 nm)

Crystals such as zinc oxide with a hexagonal structure are said to be optically anisotropic. Because of the particular arrangement of the atoms in the crystal, light generally propagates at a speed depending on the orientation of its plane of polarization relative to the crystal structure. In tetragonal and hexagonal crystals, a light ray traveling parallel to the *c*-axis encounters an isotropic structure, since $a_1 = a_2$ in these crystals. A light ray travelling in any other direction however encounters an anisotropic structure and so travels with a different velocity. The *c*-axis is therefore an optically unique axis in these crystals and is called the optic axis: for this direction, the speed of propagation is independent of the orientation of the plane of polarization of the light ray. In substances such as calcite ($CaCO_3$) and zinc oxide there is only one such axis and the crystal is termed uniaxial.

When a ray of plane-polarized light traverses a uniaxial crystal parallel to the optic axis, regardless of the vibration direction of the electric field, the index of refraction is the same and is usually denoted n_o. When a ray traverses the crystal along a direction which is normal to the optic axis, the index of refraction depends on the vibration direction of the electric field. If the vibration direction is also normal to the optic axis, then the index is also n_o. When the vibration direction is parallel to the optic axis, the index of refraction is different and is now denoted n_e. When the vibration direction lies between these two directions, then the light ray is split into two components, called the ordinary and extraordinary ray, whose electric fields are constrained to vibrate in directions respectively parallel and normal to the optic axis. The two indices of refraction n_o and n_e are

called the principal indices of refraction of a uniaxial crystal corresponding to the ordinary and extraordinary rays respectively.[41,42]

In an anisotropic material the refractive indices can be illustrated by a representation surface - the optical indicatrix (Figure 4.11). For each (orthogonal) principal direction in the anisotropic material, there is an associated principal refractive index. The variation of the refractive index with the plane of the wavefront can be represented by an ellipsoid. The semi-axes of this optical indicatrix are directly proportional to the principal refractive indices. Uniaxial crystals have two principal refractive indices and one optic axis parallel to the symmetry axis (z) and so perpendicular to the circular section.

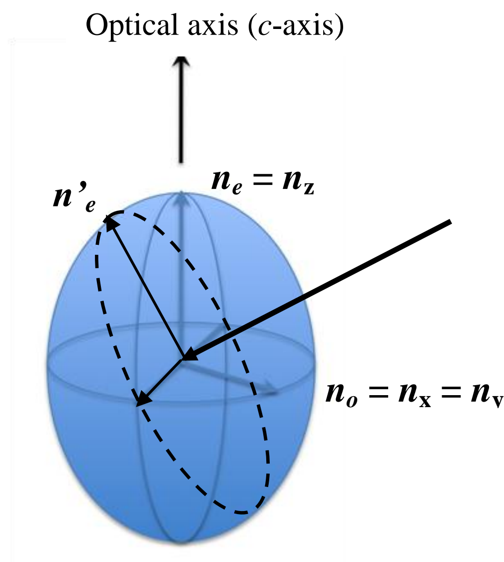

Figure 4.11: The optical indicatrix for a positive, uniaxial crystal such as ZnO

In general, the electric field of a light wave experiences two permitted vibration directions, known as the fast and slow directions, both in the plane of the wavefront, and determined by the shape of the indicatrix. Consider a section

passing through the origin of the indicatrix for a uniaxial crystal, and orientated parallel to the wavefronts, as shown by the dotted line in Figure 4.11 above. The two permitted vibration directions are given by the major and minor axes of this section. The corresponding refractive indices are the lengths of these axes. The section will be elliptical unless the light is travelling along the optic axis so that the plane of the wavefront coincides with the circular section of the ellipsoid. The ordinary vibration direction lies in the circular section of the indicatrix (i.e. perpendicular to the optic axis) with refractive index n_o. Light travelling along the optic axis experiences just this refractive index - the ordinary refractive index. The extraordinary vibration direction lies in the plane of the wavefront and perpendicular to the ordinary vibration direction, and has refractive index n'_e. The value of n'_e is determined from the ordinary refractive index and the principal extraordinary refractive index n_e.[43]

SE measurements detect both the ordinary and extraordinary ray; however, the measurement is dominated by the ordinary component.[11,44] Further, based on the measurements of other researchers, no noticeable variation is obtained in measurements on samples rotated with respect to the surface normal and with different angles of incidence;[4] our measurements similarly show no major variations in the index obtained upon rotation of the samples. This indicates that the optical *c*-axis of the zinc oxide crystal is oriented perpendicular to the substrate surface. This conclusion is borne out by X-ray diffraction data. Numerous studies of ZnO deposited on various substrates also have shown that ZnO is preferentially deposited with the *c*-axis oriented perpendicular to the

surface. Hence, measurements of sputtered zinc oxide thin films can be compared with the ordinary refractive index of bulk zinc oxide. The bulk refractive index (ordinary ray) of zinc oxide single crystal is 1.9985 at 600 nm;[45] the values measured reach a maximum value of 2.027 at a deposition temperature of 600 °C on silicon and 1.991 on platinum, almost identical to the single crystal values.

Figure 10.11 shows the comparison of the refractive index values obtained for films deposited on silicon and those deposited on platinum. The presence of a native, amorphous silicon dioxide layer on silicon substrates leads to the expectation that more crystalline films should be grown on platinum substrates.

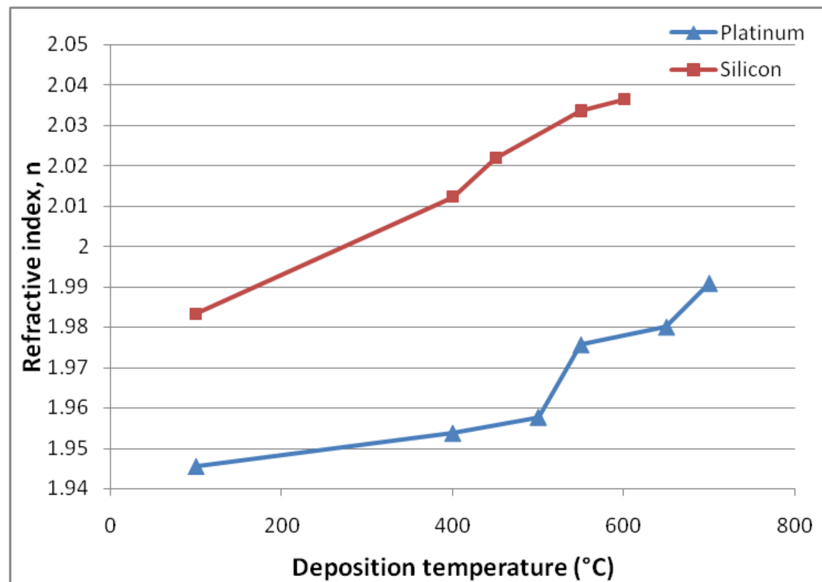

Figure 4.12: Comparison of refractive index *n*, vs. deposition temperature for ZnO films on silicon and platinum substrates

This is because Pt presents a hexagonal (111) surface, devoid of any oxide layer and should therefore provide a better surface for nucleation. Additionally, the small lattice mismatch between ZnO (3.42 Å) and Pt (3.92 Å) also supports deposition of textured films. This expectation is confirmed by comparing the

intensities of the (002) peaks in the X-ray diffraction spectra of films deposited at the same temperatures.[1] This would then lead to an expectation of higher refractive indices for films deposited on platinum compared to those on silicon at the same substrate deposition temperature. This is not observed in this study. We believe this may be due to a systematic error which would require a further careful study to elucidate. Nonetheless, we have demonstrated that increased substrate deposition temperatures lead to greater crystallinity and higher refractive indices in the temperature range studied.

4.5. Conclusions

We have successfully developed a reliable optical model based on the Lorentz oscillator for ZnO thin films on silicon and platinum substrates. This model is able to fit the data both above and below the band gap for ZnO and from it, we determined the refractive index and extinction coefficient for the thin films in the spectral range 240 – 920 nm. Additionally, we have demonstrated that the refractive index of the films increases with substrate deposition temperatures. Since previous research has shown that the film crystallinity increases with increasing substrate deposition temperatures, we can therefore conclude that the refractive index also increases with the crystallinity of the films.

References

1. Kowach, G. R.; Mirica, E.; Jones, C. D. W.; Dennis, B. S.; Pinczuk, A.; Safar, H.; Kleiman, R. N.; Kammlott, G. W., Properties of Radio Frequency (RF) Sputtered Zinc Oxide Thin Films for Piezoelectric Applications. *Lucent Technologies Technical Memorandum* **1999**.

2. Bagnall, D. M.; Chen, Y. F.; Zhu, Z.; Yao, T.; Koyama, S.; Shen, M. Y.; Goto, T., Optically pumped lasing of ZnO at room temperature. *Applied Physics Letters* **1997,** 70, (17), 2230-2232.

3. Tang, Z. K.; Wong, G. K. L.; Yu, P.; Kawasaki, M.; Ohtomo, A.; Koinuma, H.; Segawa, Y., Room-temperature ultraviolet laser emission from self-assembled ZnO microcrystallite thin films. *Applied Physics Letters* **1998,** 72, (25), 3270-3272.

4. Washington, P. L.; Ong, H. C.; Dai, J. Y.; Chang, R. P. H., Determination of the optical constants of zinc oxide thin films by spectroscopic ellipsometry. *Applied Physics Letters* **1998,** 72, (25), 3261-3263.

5. Hu, W. S.; Liu, Z. G.; Sun, J.; Zhu, S. N.; Xu, Q. Q.; Feng, D.; Ji, Z. M., Optical Properties of Pulsed Laser Deposited ZnO Thin Films. *Journal of Physics and Chemistry of Solids* **1997,** 58, (6), 853-857.

6. Liu, Y. C.; Hsieh, J. H.; Tung, S. K., Extraction of optical constants of zinc oxide thin films by ellipsometry with various models. *Thin Solid Films* **2006,** 510, 32-38.

7. Dumont, E.; Dugnoille, B.; Bienfait, S., Simultaneous determination of the optical properties and of the structure of r.f.-sputtered ZnO thin films. *Thin Solid Films* **1999,** 353, (1-2), 93-99.

8. G. E. Jellison, J.; Boatner, L. A., Optical Functions of Uniaxial ZnO determined by Generalized Ellipsometry. *Physical Review B* **1998,** 58, (7), 3586-3589.

9. Liang, W. Y.; Yoffe, A. D., Transmission Spectra of ZnO Single Crystals. *Physical Review Letters* **1968,** 20, (2), 59.

10. Matz, R.; Lüth, H., Ellipsometric spectroscopy of the ZnO nonpolar surface. *Applied Physics A: Materials Science & Processing* **1979,** 18, (2), 123-130.

11. Rebien, M.; Henrion, W.; Bar, M.; Fischer, C.-H., Optical properties of ZnO thin films: Ion layer gas reaction compared to sputter deposition. *Applied Physics Letters* **2002,** 80, (19), 3518-3520.

12. Kang, S. J.; Joung, Y. H., Influence of substrate temperature on the optical and piezoelectric properties of ZnO thin films deposited by RF magnetron sputtering. *Applied Surface Science* **2007,** 253, (17), 7330-7335.

13. Cetinorgu, E.; Goldsmith, S.; Zhitomirsky, V. N.; Boxman, R. L.; Bungay, C. L., Optical characterization of filtered vacuum arc deposited zinc oxide thin films. *Semiconductor Science and Technology* **2006,** 21, (9), 1303-1310.

14. Tompkins, H. G.; McGahan, W. A., *Spectroscopic Ellipsometry and Reflectometry: A User's Guide*. John Wiley and Sons, Inc.: 1999.

15. Chopra, K. L., *Thin Film Phenomena*. McGraw-Hill: 1969.

16. Mirica, E.; Kowach, G.; Evans, P.; Du, H., Morphological Evolution of ZnO Thin Films Deposited by Reactive Sputtering. *Crystal Growth and Design* **2004,** 4, (1), 147-156.

17. SCI, *FilmTek (TM) 3000SE Operations Manual*. Scientific Computing International: 2006.

18. Cetinorgu, E.; Goldsmith, S.; Boxman, R. L., The effect of substrate temperature on filtered vacuum arc deposited zinc oxide and tin oxide thin films. *Journal of Crystal Growth* **2007,** 299, (2), 259-267.

19. Heitsch, S.; Bundesmann, C.; Wagner, G.; Zimmermann, G.; Rahm, A.; Hochmuth, H.; Benndorf, G.; Schmidt, H.; Schubert, M.; Lorenz, M.; Grundmann, M., Low temperature photoluminescence and infrared dielectric functions of pulsed laser deposited ZnO thin films on silicon. *Thin Solid Films* **2006,** 496, (2), 234-239.

20. Kim, K.-S.; Kim, H. W.; Lee, C. M., Effect of growth temperature on ZnO thin film deposited on SiO2 substrate. *Materials Science and Engineering B* **2003,** 98, (2), 135-139.

21. Singh, S.; Srinivasa, R. S.; Major, S. S., Effect of substrate temperature on the structure and optical properties of ZnO thin films deposited by reactive rf magnetron sputtering. *Thin Solid Films* **2007,** 515, (24), 8718-8722.

22. Bond, W. L., Measurement of the Refractive Indices of Several Crystals. *Journal of Applied Physics* **1965,** 36, (5), 1674-1677.

23. Park, Y. S.; Schneider, J. R., Index of Refraction of ZnO. *Journal of Applied Physics* **1968,** 39, (7), 3049-3052.

24. Inukai, T.; Matsuoka, M.; Ono, K., Characteristics of zinc oxide thin films prepared by r.f. magnetron-mode electron cyclotron resonance sputtering. *Thin Solid Films* **1995,** 257, (1), 22-27.

25. Gupta, V.; Mansingh, A., Influence of postdeposition annealing on the structural and optical properties of sputtered zinc oxide film. *Journal of Applied Physics* **1996,** 80, 1063.

26. Sun, X. W., Optical properties of epitaxially grown zinc oxide films on sapphire by pulsed laser deposition. *Journal of Applied Physics* **1999,** 86, (1), 408.

27. Zayer, N. K.; Greef, R.; Rogers, K.; Grellier, A. J. C.; Pannell, C. N., In situ monitoring of sputtered zinc oxide films for piezoelectric transducers. *Thin Solid Films* **1999,** 352, (1-2), 179-184.

28. Postava, K.; Sueki, H.; Aoyama, M.; Yamaguchi, T.; Ch, I.; Igasaki, Y.; Horie, M., Spectroscopic ellipsometry of epitaxial ZnO layer on sapphire substrate. *Journal of Applied Physics* **2000,** 87, (11), 7820-7824.

29. Moustaghfir, A.; Tomasella, E.; Ben Amor, S.; Jacquet, M.; Cellier, J.; Sauvage, T., Structural and optical studies of ZnO thin films deposited by r.f. magnetron sputtering: influence of annealing. *Surface and Coatings Technology* **2003,** 174-175, 193-196.

30. Ondo-Ndong, R.; Ferblantier, G.; Al Kalfioui, M.; Boyer, A.; Foucaran, A., Properties of RF magnetron sputtered zinc oxide thin films. *Journal of Crystal Growth* **2003,** 255, (1-2), 130-135.

31. Ondo-Ndong, R.; Pascal-Delannoy, F.; Boyer, A.; Giani, A.; Foucaran, A., Structural properties of zinc oxide thin films prepared by r.f. magnetron sputtering. *Materials Science and Engineering B* **2003,** 97, (1), 68-73.

32. Mehan, N.; Gupta, V.; Sreenivas, K.; Mansingh, A., Effect of annealing on refractive indices of radio-frequency magnetron sputtered waveguiding zinc oxide films on glass. *Journal of Applied Physics* **2004,** 96, (6), 3134-3139.

33. Shan, F. K.; Liu, G. X.; Lee, W. J.; Lee, G. H.; Kim, I. S.; Shin, B. C.; Kim, Y. C., Transparent conductive ZnO thin films on glass substrates deposited by pulsed laser deposition. *Journal of Crystal Growth* **2005,** 277, (1-4), 284-292.

34. Liu, Y. C.; Tung, S. K.; Hsieh, J. H., Influence of annealing on optical properties and surface structure of ZnO thin films. *Journal of Crystal Growth* **2006,** 287, (1), 105-111.

35. Senadim, E.; Eker, S.; Kavak, H.; Esen, R., Optical and structural parameters of the ZnO thin film grown by pulsed filtered cathodic vacuum arc deposition. *Solid State Communications* **2006,** 139, (9), 479-484.

36. Cetinorgu, E., Characteristics of filtered vacuum arc deposited ZnO-SnO2 thin films on room temperature substrates. *Optics Communications* **2007,** 280, (1), 114-119.

37. Gioffre, M.; Angeloni, M.; Gagliardi, M.; Iodice, M.; Coppola, G.; Aruta, C.; Della Corte, F. G., The influence of oxygen on the optical properties of RF-sputtered zinc oxide thin films. *Superlattices and Microstructures* **2007,** 42, (1-6), 85-88.

38. Kang, S.; Joung, Y.; Chang, D.; Kim, K., Piezoelectric and optical properties of ZnO thin films deposited using various O2/(Ar+O2) gas ratios. *Journal of Materials Science: Materials in Electronics* **2007,** 18, (6), 647-653.

39. Khoshman, J. M.; Kordesch, M. E., Optical constants and band edge of amorphous zinc oxide thin films. *Thin Solid Films* **2007,** 515, (18), 7393-7399.

40. Khandelwal, R.; Singh, A. P.; Kapoor, A.; Grigorescu, S.; Miglietta, P.; Stankova, N. E.; Perrone, A., Effects of deposition temperature on the structural and morphological properties of thin ZnO films fabricated by pulsed laser deposition. *Optics & Laser Technology* **2008,** 40, (2), 247-251.

41. Azaroff, L. V., *Introduction to Solids*. Tata McGraw-Hill Publishing Company Limited: 1977; p 460.

42. Moulson, A. J.; Herbert, J. M., *Electroceramics: Materials, Properties, Applications*. Chapman and Hall: 1990.

43. Fujiwara, H., *Spectroscopic Ellipsometry Principles and Applications*. John Wiley and Sons, Ltd.: 2007.

44. Aspnes, D. E., Approximate Solution of Ellipsometric Equations for Optically Biaxial Crystals. *Journal of the Optical Society of America* **1980,** 70, (10), 1275-1277.

45. Nikogosyan, D. N., *Properties of Optical and Laser-Related Materials: A Handbook*. John Wiley and Sons: 1997.

Chapter 5: Optical Properties of Strontium Titanate Thin Films

5.1 Introduction

Strontium titanate ($SrTiO_3$ or STO) possesses several interesting properties that have made the material of great interest for various potential applications. Non-stoichiometric or doped *n*-type semiconducting $SrTiO_3$ may be applicable as dielectric and photoelectric material. Thin films may find applications in microelectronics, solar and sensor technology[1]: a potential application is as charge storage material in high density dynamic random access memory (DRAM). As an incipient ferroelectric that has low dielectric loss and large dielectric non-linearity at cryogenic temperatures, it is an ideal candidate for tunable microwave devices with high temperature semiconductors. Thin films have potential to compete with GaAs-based Schottky diodes in microwave varactor technology.[2] Most studies of STO thin films have focused on materials grown by molecular beam epitaxy (MBE) and pulsed laser deposition (PLD);[3-5] however, materials grown by cheaper or other methods such as radio frequency (RF) magnetron sputtering are poised to become good alternatives in technological applications once their quality can be confirmed and their optical properties well understood. Techniques such as spectroscopic ellipsometry and reflectometry are excellent tools for studying the optical properties of materials grown by this method. We report here an analysis of the optical properties of STO thin films grown on silicon and platinum substrates at varying deposition temperatures. Our results also show that the film crystallinity is dependent on the deposition

temperatures and substrate and that this relationship can be quantified using the refractive index (*n*) determined by ellipsometric methods. Additionally, our results show that the STO thin films thus prepared exhibit a graded index of refraction when the films are deposited above 300 °C and show no interfacial layer formed between the substrate and film.

5.2 Structure and Properties of Strontium Titanate

Strontium titanate, $SrTiO_3$, is an incipient ferroelectric (i.e., it behaves like a ferroelectric material in the paraelectric phase[6]) and member of the perovskite family of compounds (Figure 5.1). Unstrained and at room temperature it has a cubic perovskite structure and undergoes a phase transition to a tetragonal structure when cooled to 110 K. When this occurs, the Ti atoms are slightly displaced and the structure becomes non-centrosymmetric: the material thus has the potential to exhibit ferroelectric and piezoelectric behavior. Ferroelectric materials are good capacitors and thus can be used as computer memory since in one polarized state or another they can act as binary systems. $SrTiO_3$ is an insulator transparent to visible light. The fundamental band gap for the bulk is 3.22 eV which is generally believed to be due to transitions from *2p* oxygen states to *3d* titanium states.[5]

Epitaxial films of STO are of interest as high-κ gate dielectrics because of the potential for higher uniformity, lower defect density and lower leakage current relative to polycrystalline metal oxides or amorphous silicon dioxide films.[4]

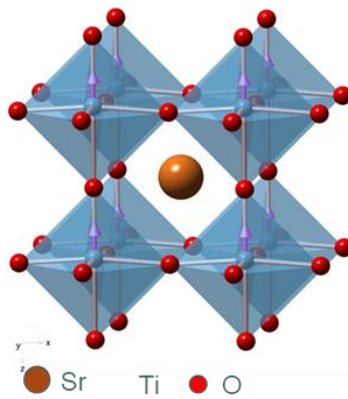

Figure 5.1: Crystal Structure of Strontium Titanate
http://www.camsoft.co.kr/CrystalMaker/graphics/resources/hires/perovskite.jpg

Epitaxial STO also has potential use as an intermediate layer between a ferroelectric thin film and silicon substrate in a metal-ferroelectric-insulator-semiconductor field-effect transistor (MFIS FET) to prevent reaction and interdiffusion between the ferroelectric and silicon.[7]

5.3 Experimental

5.3.1 Preparation of Strontium Titanate Thin Films

Strontium titanate films were deposited by radio frequency planar magnetron sputtering in an ANELVA SPF-332H system, a schematic of which is shown in Chapter 4 (figure 2). This system consists of a cryogenic vacuum pump which achieves a base pressure of less than 5 x 10^7 torr, a RF power supply (13.56 MHz) with a matching unit, a 3 inch diameter coaxial planar magnetron under the target holder, argon (Ar) and oxygen (O_2) gas inlets and quartz lamps for substrate heating. A $SrTiO_3$ target (3.0 inch diameter, 0.25 inch thickness, 99.9% purity, Sputtering Target Manufacturing Co.) was sputtered in an Ar-O_2 (4:1) plasma discharge at 5 sccm flow rates for each gas with varying chamber pressures. A 4-inch main butterfly valve controls the total pressure in the system during deposition. High purity gases (Ar and O_2) were premixed and introduced into the system. The flow rates were adjusted by manual leak valves and measured using Matheson flow meters. The total working pressure in the system was measured with a MKS Baratron capacitance gauge.

Two types of substrates were used in this process: Si (100) wafers bearing a native oxide layer and Pt (111) deposited on Si. Before deposition onto the substrates, the target was presputtered for 10 minutes. During this period, the deposition of strontium titanate on the substrate was prevented by the presence of a shutter. After presputtering, the shutter removal changed the plasma impedance, requiring the retuning of the RF power source from the matching unit to optimize the sputtering process. During sputtering, the substrates were placed parallel to

the target surface in a sputter-down geometry. The substrates were either intentionally heated with a quartz lamp to temperatures varying from 300 – 700 °C, or unintentionally heated to a temperature varying from 45 to 65 °C due to energetic particle bombardment. The substrate temperature was measured by a thermocouple situated below and in contact with the substrate. The target substrate distance was 95 mm.

5.3.2 Determination of the Optical Properties

Multi-angle reflectometry measurements on the films were carried out on a Film Tek™ 3000SE metrology system (Scientific Computing International (SCI)). The reflectance measurements were carried out at normal incidence and polarized 70° incidence over the wavelength range 240 – 920 nm using a deuterium-halogen light source. Details of the experimental setup and procedure are given in chapter 3.

5.4 Results

5.4.1 Description of Model

The films were analyzed with multi-angle reflectometry because at larger film thicknesses (approximately 1 micron), ellipsometric data is less reliable and so were omitted from the measurement. The film on silicon was modeled as two-layers consisting of the substrate, and a strontium titanate graded layer. The strontium titanate graded layer was modeled using a graded material model similar to an effective medium approximation (EMA), except that the mixture ratio is specified at different depths within the layer. The mixture ratio throughout the graded layer is assumed to be a linear interpolation of the mixture ratio at the specified nodes. The strontium titanate layer was modeled using a two-oscillator SCI™ dispersion model which is a generalized Lorentz oscillator model which allows for coupling between the oscillators. In the limit as the damping coefficient goes to zero, the SCI™ model converges to the Lorentz oscillator model.[8] The following parameters were varied: the high frequency dielectric constant; the damping coefficient; the center energy of each oscillator, the amplitude of each oscillator and the oscillator vibration (broadening) frequency. The reflectometry data was then analyzed using a multiple parameter regression analysis in the wavelength range 400 – 920 nm, the region in which the film is transparent. The films on platinum were modeled as two layers consisting of the substrate and a strontium titanate layer. The strontium titanate layer was modeled using a three-oscillator SCI™ dispersion model which is a generalized Lorentz oscillator model that allows for coupling between the oscillators. In the limit as the damping

coefficient goes to zero, the SCI™ model converges to the Lorentz oscillator model. The following parameters were varied: the high frequency dielectric constant; the damping coefficient; the center energy of each oscillator, the amplitude of each oscillator and the oscillator vibration (broadening) frequency. The data was then analyzed using a multiple parameter regression analysis in the wavelength range 240 – 920 nm.

5.4.2 Sample Reflectometry Data

Figures 5.2A and 5.3A show typical measured and simulated spectroscopic reflectometry data for a strontium titanate film grown on a silicon substrate at a deposition temperature of 700°C and platinum substrate at 500 °C respectively, as well as the graded refractive index and extinction coefficient dispersion spectra determined using the SCI ™ model. Table 5.1 shows the values of the regression parameters for the film deposited on silicon while Table 5.3 gives those for the film on platinum. A summary of the results obtained for the analyzed films is shown in Tables 5.2 and 5.4 below. Appendix B contains all the data sets analyzed in this manuscript.

5.4.2.1 STO Thin Film on Silicon Substrate

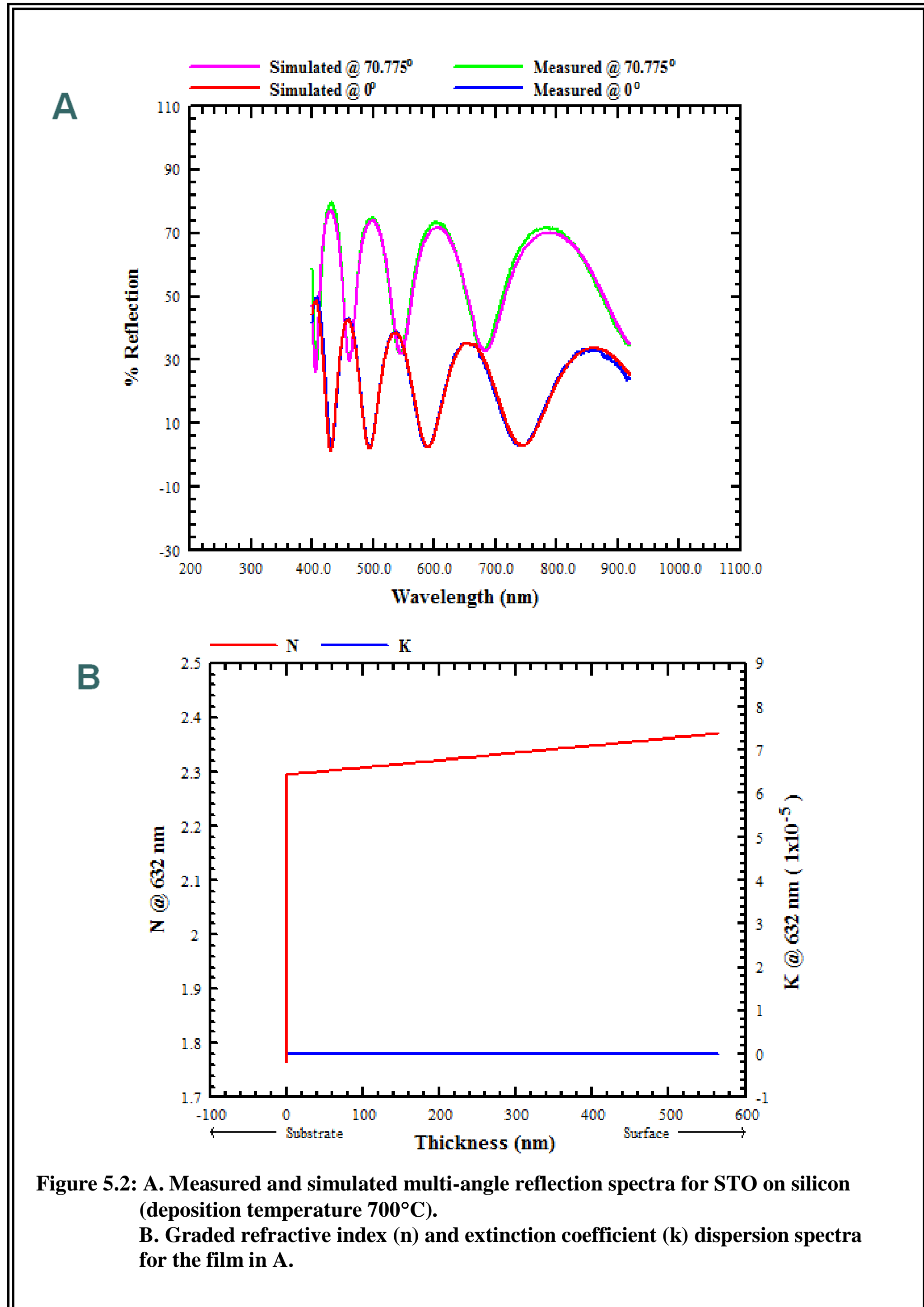

Figure 5.2: A. Measured and simulated multi-angle reflection spectra for STO on silicon (deposition temperature 700°C).
B. Graded refractive index (n) and extinction coefficient (k) dispersion spectra for the film in A.

Table 5.1: Regression Parameter Data and Extracted Optical Constants for fits shown in Figure 5.2.

Layer #1Material Coefficients Table	
EMA Screening	0.3333
EMA Type	Landau-Lifshitz
Number of Nodes	3
Host Material	Same As Layer #2
Material #2	Same As Layer #3
% POSITION NODE #1	0.00
% POSITION NODE #2	0.00
% POSITION NODE #3	100.00
% FRACTION NODE #1	0.0000
% FRACTION NODE #2	87.8428
% FRACTION NODE #3	100.0000
Extracted Data	
Thickness Layer 1 (STO)	564.88 nm ± 0.05 nm
Maximum Refractive Index @ 632 nm	2.32958 ± 0.00010
Extinction coefficient @ 632 nm	0.0000
RMSE	1.638

Table 5.2 Summary of Data for Strontium Titanate Films on Silicon Substrate

Sample ID	Deposition Temperature (°C)	Thickness (nm) ± 0.05 nm	Refractive Index (*n*)† ± 0.00010	Extinction Coefficient (*k*)†	RMSE
DK15	RT*	1650	1.84401	0	4.962
DK17	300	1580	1.98940	0	6.415
DK19	400	858	2.27359	0	2.325
DK14	500	1370	2.30412	0	2.255
DN64	500	1181	2.28078	0	2.002
DN66	700	810	2.36684	0	2.618
DN63	700	565	2.32958	0	1.638
DN67	800	660	2.38458	0	2.561

† Measured at 632.8 nm

*RT = room temperature i.e., no external heating of substrate

5.4.1.2 STO Thin Film on Platinum Substrate

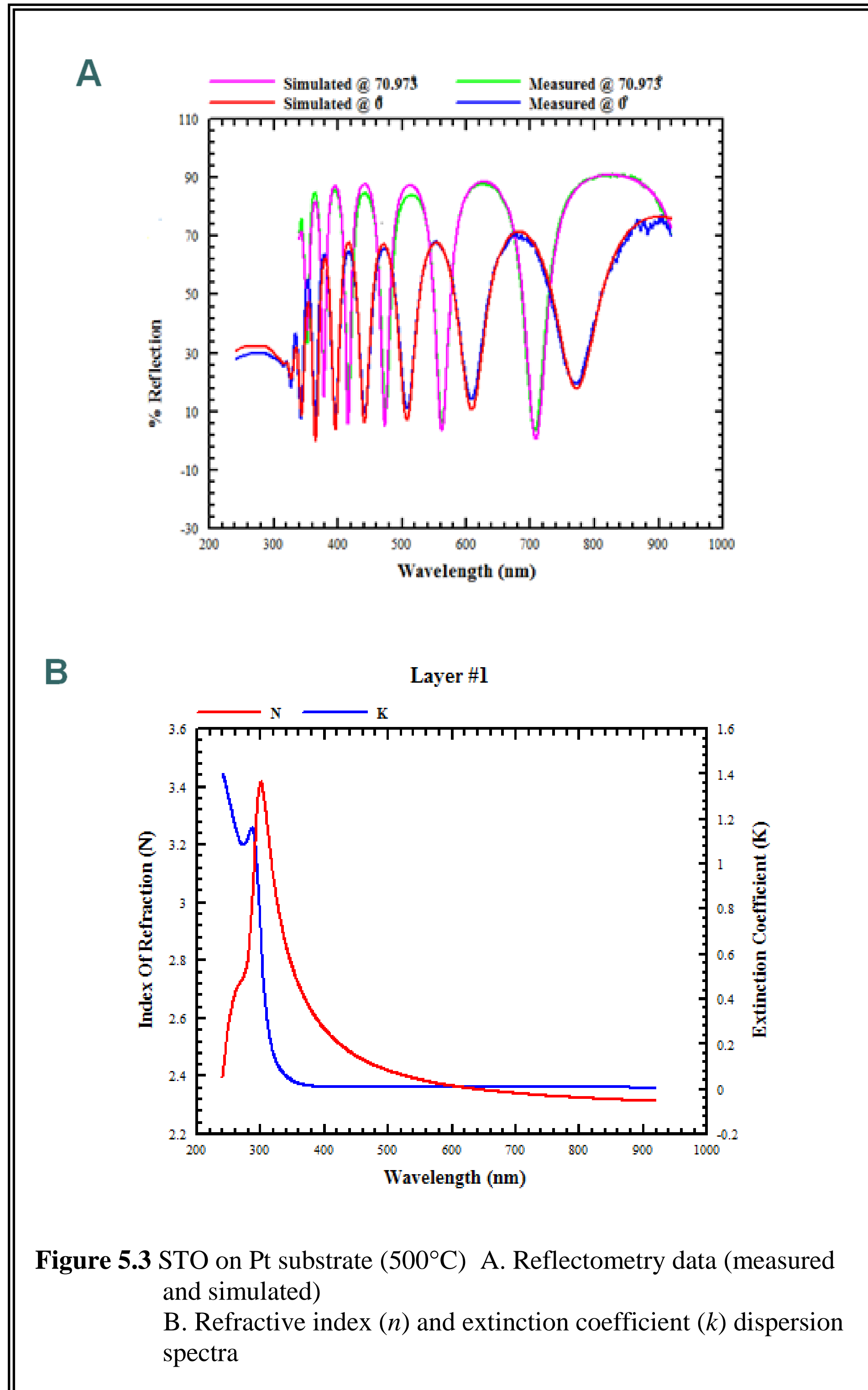

Figure 5.3 STO on Pt substrate (500°C) A. Reflectometry data (measured and simulated)
B. Refractive index (n) and extinction coefficient (k) dispersion spectra

Table 5.3: Regression Parameter Data and Extracted Optical Constants for fits shown in Figure 5.3

Layer #1 Material Coefficient Table	
Number of Oscillators	3
HF Dielectric Constant	1.744346
Damping Coefficient	1.251767
Amplitude (1)	1.289897
Center Energy (1)	4.399506
Vibrational Frequency (1)	0.398148
Amplitude (2)	4.696470
Center Energy (2)	4.664757
Vibrational Frequency (2)	1.154658
Amplitude (3)	3.006969
Center Energy (3)	3.653673
Vibrational Frequency (3)	4.878242
Extracted Data	
Thickness Layer 1 (STO)	601.02 nm ± 0.05 nm
Maximum Refractive Index @ 632.8 nm	2.28980 ± 0.00010
Extinction coefficient @ 632.8 nm	0.0112
RMSE	2.164

Table 5.4 Summary of Data for Strontium Titanate Films on Platinum Substrate

Sample ID	Deposition Temperature (°C)	Thickness (nm) ± 0.05 nm	Refractive Index (*n*) † ± 0.00010	Extinction Coefficient (*k*)† ± 0.00010	RMSE
DK15_2	100	1350	2.03065	0	6.721
DK17_1	300	1264	2.19165	0	6.286
DK19_1	400	762	2.38630	0.00683	4.272
DK9_2	500	562	2.35717	0	2.432
DK29_2R	600	830	2.33335	0.00823	3.081
DN66_2R	700	578	2.33400	0	6.727

† Measured at 632.8 nm

5.4.3 X-Ray Diffraction Data

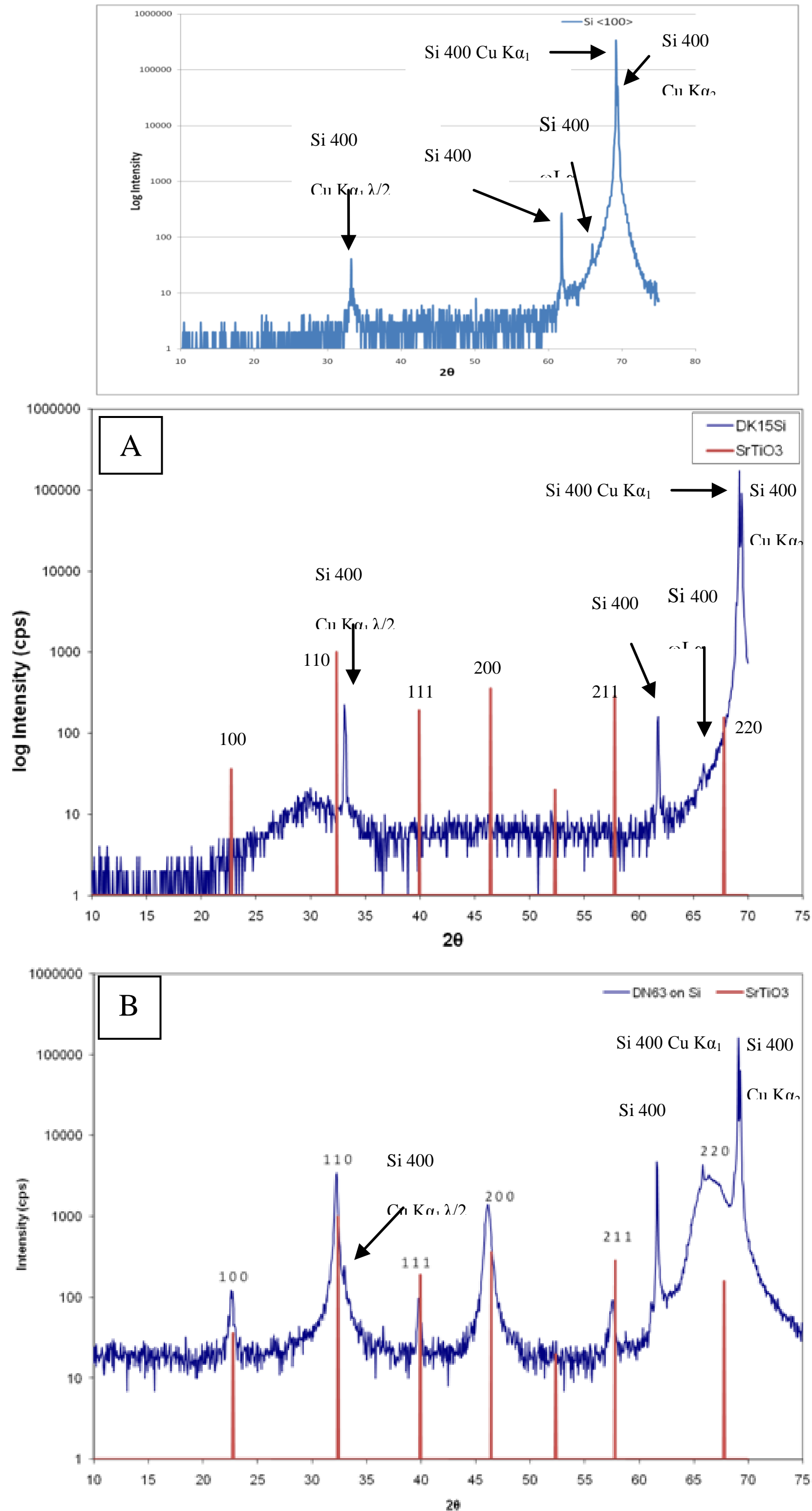

Figure 5.4: X-Ray diffraction spectra for Si substrate (top) and STO on silicon substrate at deposition temperature (a) 100 °C and (b) 700 °C

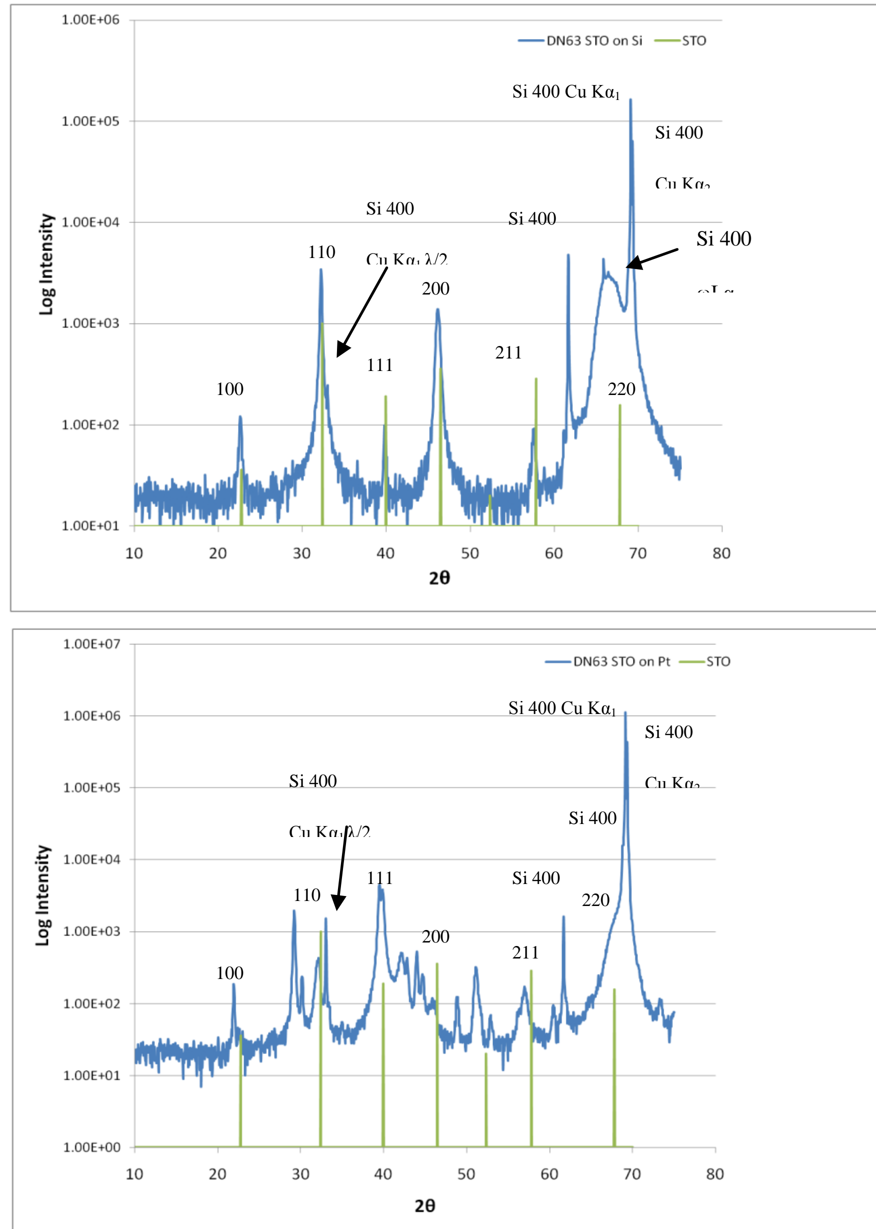

Figure 5.5: X-ray diffraction spectra for Si substrate (top), STO on Si (middle) and Pt (bottom) substrate (deposition temperature 700°C)

5.5 Discussion

Figures 5.2 and 5.3 show typical measured and simulated multi-angle reflection data for the strontium titanate thin films measured at 0 and 70.775 degrees. Tables 5.1 and 5.3 list the regression parameters used in the analysis and optical data obtained. The quality of the fits of the data to the models used is amply demonstrated by the close match of the simulated data to the measured spectra: the average RMSE obtained for these fits was 3.097 in the spectral region 400- 920 nm for films deposited on silicon, and 4.920 over the spectral range 240 – 920 nm for films deposited on platinum. These values demonstrate the excellent fitting capabilities of the models (the best understood material, SiO_2 on Si, typically gives fits of between 0.5 – 1.0). The results also indicate that the films are smooth since no effective medium approximation (EMA) layer, which accounts for surface roughness in the films, was required to obtain good fits.

The reflectance spectra show strong interference oscillations due to multiple internal reflections between the film and the substrate. The refractive index dispersion spectrum shows the typical semiconductor dispersion, that is, *n* decreases with increasing wavelength as well as the typical shape near an electronic interband transition. Band structure calculations show that STO has an indirect gap at about 3.2 eV and a direct gap at about 3.4 eV usually attributed to interband transitions from the oxygen 2*p* states to titanium 3*d* states.[5] There are also other features at 3.8, 4.3, 4.8, 6.2 and 8.5 eV known as van Hove singularities or critical points, related to optical interband transitions from the highest valence bands to the lowest conduction bands at various points in the Brillouin zone.[9, 10] Figure 5.6

shows a comparison of the dispersion spectra for single crystal strontium titanate (data from reference 6) and that obtained for our film with a substrate deposition temperature of 500 °C.

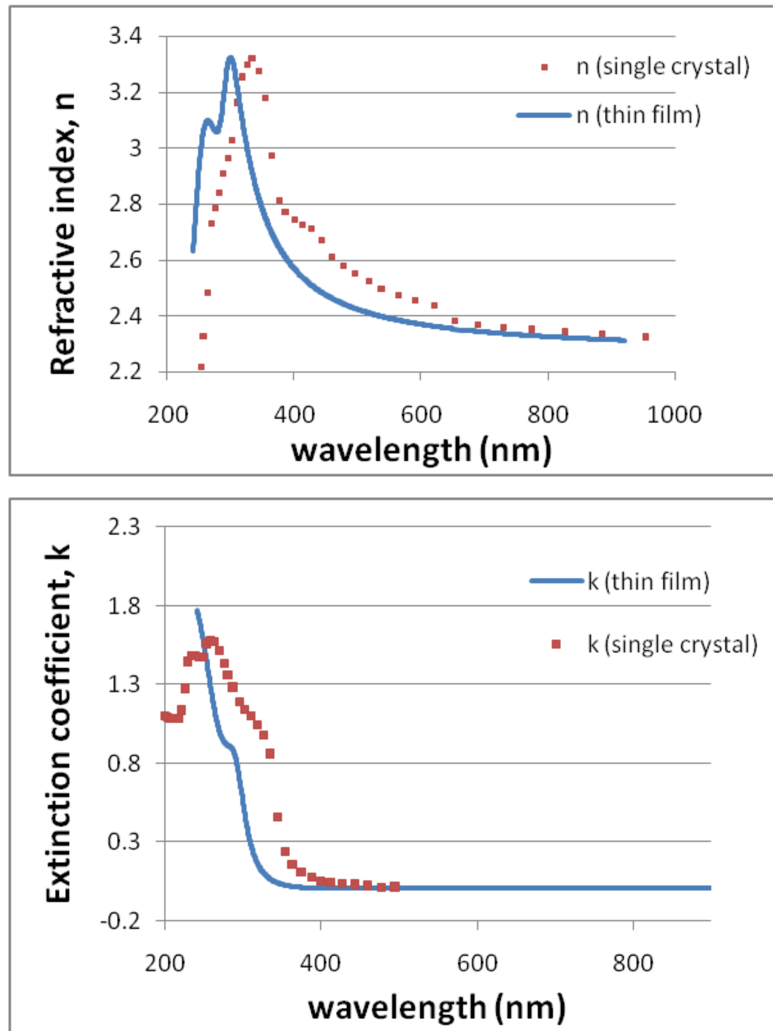

Figure 5.6: Comparison of Optical Constant Dispersion of STO thin film (this work) and single crystal (data from ref. 6) for (a) refractive index, *n* and (b) extinction coefficient, *k*.

The data shows that the shape of the dispersion spectra is very similar to that obtained for single crystal STO; however, the band edge in the *k* spectrum is shown to be shifted from 365 nm to about 320 nm. For the film with substrate deposition

temperature of 700 °C, the band edge shows a shift to about 360 nm, approaching the direct band edge value for single crystal material, a consequence of the enhanced refractive index as will be discussed later. Ma and colleagues[5] deposited STO films on vitreous silica substrate by RF magnetron sputtering and measured their optical properties by transmittance measurements. Zhang and colleagues[11] deposited STO on fused-quartz substrates by pulsed laser deposition and also used transmittance measurements to study their optical properties. Both groups saw a shift in the band gap energy to higher energies which was attributed to thermal stress in the film exerted by the substrate due to their different expansion coefficients. This could possibly be a contributing factor in our case, although we believe the effect is also due to the imperfect texture in the films.

Both substrates show a trend of increasing refractive index, n with increasing substrate deposition temperature, as shown in Table 5.2 and Table 5.4. Figure 5.7 below for films on silicon substrate demonstrates this trend graphically. The refractive index is an indicator of packing density: thus the increase in n with temperature can be understood as due to the increased packing density of the film at higher temperatures. As the deposition temperature increases, the atomic species impinging on the substrate surface have increased kinetic energy and thus higher surface diffusion. This consequently leads to better film crystallinity as the atoms have sufficient energy to assemble into a more regular structure. Thus increased packing density, as evidenced by higher n values, indicate a more crystalline film than those obtained at lower substrate temperatures. This observation was also

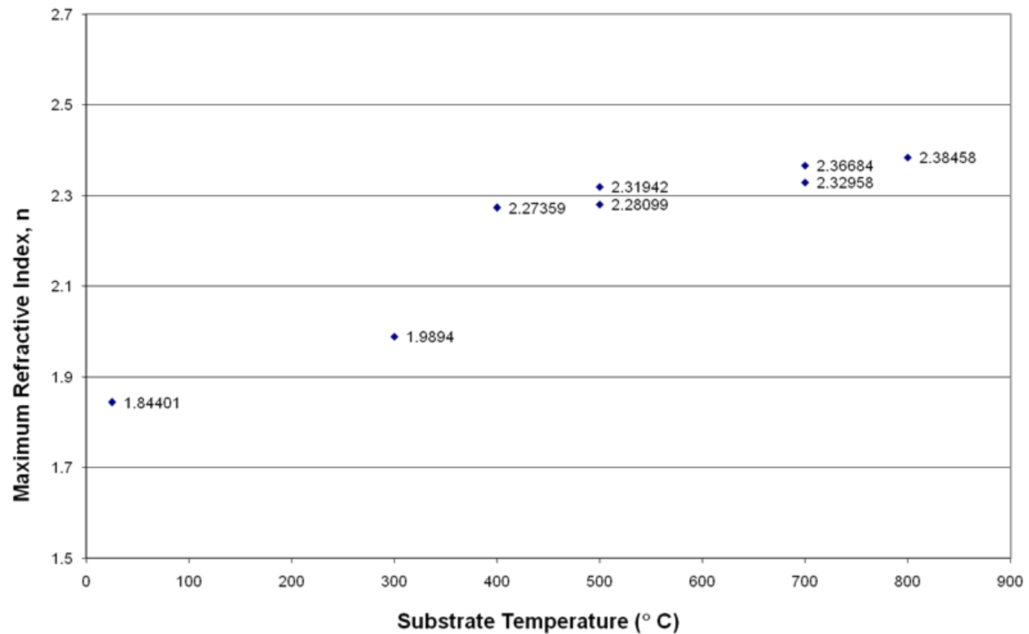

Figure 5.7: Refractive index vs. substrate deposition temperature for STO film on silicon substrate

studied by X-ray diffraction. Figures 5.4 show X-ray diffraction patterns for films deposited at 100° and 700°C compared with data for strontium titanate single crystal. The film deposited at 100°C shows only the STO <110> characteristic reflection shifted to a higher value of 2θ, indicating a non-ideal stoichiometry. In comparison, the film deposited at the higher temperature show all but one of the characteristic STO reflections.

The effect of the substrate on the resulting film was also studied. Figure 5.8 below compares the refractive index of the film on silicon with those on platinum at similar substrate deposition temperatures. The results show that overall higher refractive indices result for films deposited on platinum, suggesting that these films have greater crystallinity. This result can be understood by considering the nature of the substrates: silicon possesses an amorphous, native oxide layer

whereas platinum is a non-oxide forming metal with a hexagonal <111> surface. Films deposited on silicon are presented with an amorphous surface and thus have to self-nucleate.

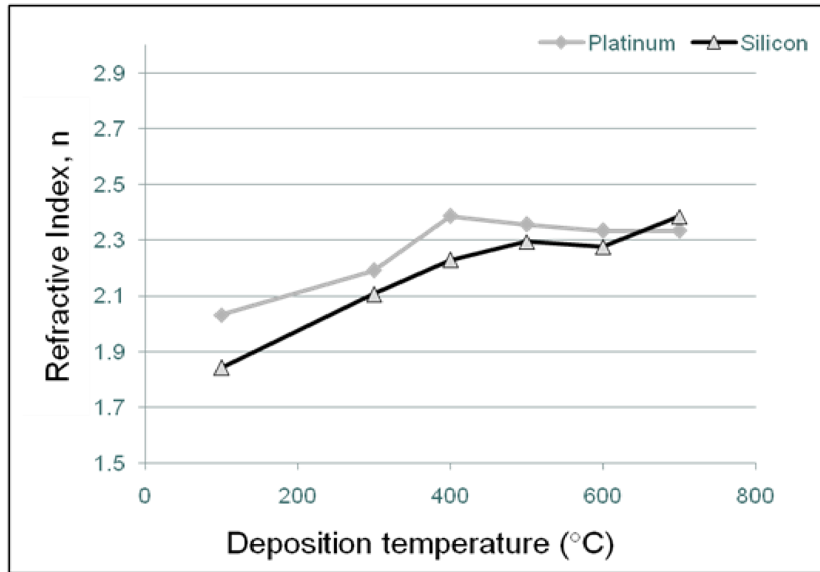

Figure 5.8: Refractive index, *n* vs. substrate deposition temperature for films on silicon and platinum substrate

The analysis of the ellipsometry data indicates a graded refractive index on silicon: the index increases linearly in the normal direction, reaching a maximum at the sample surface (Figure 5.2b). It seems likely that the initial layers of STO are not as well organized because of the lattice mismatch with the amorphous surface but subsequent layers become increasingly textured as the layers beneath provide a nucleation surface. Figure 5.9 shows a schematic representation of the graded index. The appearance of the graded index appears in films with substrate deposition temperatures above 300°C and is also accompanied by a large

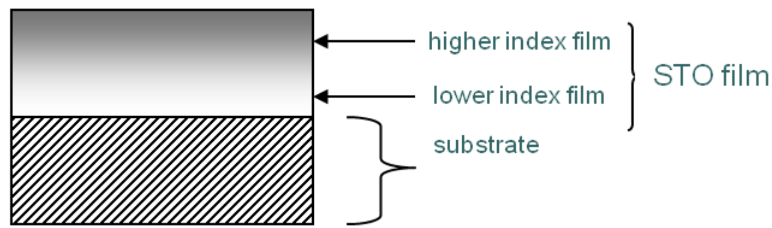

Figure 5.9: Schematic of STO film structure showing gradation in refractive index with film depth

increase in the measured index. Again, this can be rationalized on the basis of atom mobility: at temperatures above 300°C the atoms apparently have greater than the minimum energy and thus packing density and packing efficiency shows a large increase as typified by the increase in *n* (1.989 at 300 °C to 2.274 at 400°C).

Several research groups have reported the need to include an interfacial layer in the optical model for STO films on silicon.[4, 10, 12, 13] Our analysis yields excellent fits without needing to do so; indeed, the fits are actually worsened by doing so. We believe that the need for an interfacial layer is due to simplistic modeling of the data. Initially, films were modeled as a single layer using single wavelength data (single wavelength ellipsometry, SWE). With the advent of SE, the analysis improved somewhat by using multi-wavelength data, but the optical model was still single-layered. While multi-layer, multi-wavelength analysis is now being used, we believe that our approach of using a graded model represents the next level of sophistication, and will lead to a dramatic impact on the understanding of thin films of these materials.

Films deposited on platinum by comparison show no graded index – the data can be fitted with a 3-oscillator, single-layer model. As mentioned earlier,

platinum presents a hexagonal <111> textured surface with a lattice parameter of 3.923 Å.[6,10] This is very close to the bulk lattice parameter of STO which is 3.905 Å; therefore platinum offers a very good nucleation site for STO film growth. X-ray diffraction data also provides evidence of this: Figure 5.4 shows X-ray data for films grown on silicon and platinum under identical deposition conditions. The data show that while both films have excellent texture, the film on platinum has higher intensity in the characteristic reflections and also show more features in its spectrum, again suggesting higher crystallinity in the films grown on platinum.

The bulk refractive index of $SrTiO_3$ is 2.385 at 632.8 nm;[6] the refractive index of our films reached a maximum value of 2.385 and 2.386 on silicon and platinum respectively which is very close to the bulk value, indicating very high crystallinity and film quality.

5.6 Conclusion

Multi-layer models of reflectometry data were successfully developed to analyze the optical properties of strontium titanate thin films deposited on silicon and platinum-coated silicon substrates. Specifically, a graded index model was used to successfully fit the data for films grown on silicon. Our results show that the crystallinity of the films increases with substrate deposition temperature, as typified by an increase in the refractive index, which was attributed to better packing density with increased atom mobility. We also showed that the films deposited on platinum have greater crystallinity due to the better nucleation site afforded by the textured platinum surface in comparison with the amorphous oxide on the silicon substrate. Lastly, the refractive index of the thin films on silicon was 2.38458 at a deposition temperature of 800 °C and 2.33400 at a deposition temperature of 700 °C on platinum, measured at 632.8 nm. These values closely approach the bulk value of 2.389, indicating that good quality films were deposited.

References

1. Hubert, T.; Beck, U.; Kleinke, H., Amorphous and nanocrystalline $SrTiO_3$ thin films. *Journal of Non-Crystalline Solids* **1996,** 196, 150-154.

2. Taylor, T. R.; Hansen, P. J.; Pervez, N.; Acikel, B.; York, R. A.; Speck, J. S., Influence of stoichiometry on the dielectric properties of sputtered strontium titanate thin films. *Journal of Applied Physics* **2003,** 94, (5), 3390.

3. Du, Y.; Zhang, M.-S.; Wu, J.; Kang, L.; Yang, S.; Wu, P.; Yin, Z., Optical properties of $SrTiO_3$ thin films by pulsed laser deposition. *Applied Physics A: Materials Science & Processing* **2003,** 76, (7), 1105.

4. Goncharova, L. V.; Starodub, D. G.; Garfunkel, E.; Gustafsson, T.; Vaithyanathan, V.; Lettieri, J.; Schlom, D. G., Interface structure and thermal stability of epitaxial $SrTiO_3$ thin films on Si (001). *Journal of Applied Physics* **2006,** 100, (1), 014912.

5. Ma, J. H.; Huang, Z. M.; Meng, X. J.; Liu, S. J.; Zhang, X. D.; Sun, J. L.; Xue, J. Q.; Chu, J. H., Optical Properties of $SrTiO_3$ thin films deposited by radio-frequency magnetron sputtering at various substrate temperatures. *Journal of Applied Physics* **2006,** 99, 033515 - 03315-5.

6. Palik, E. D., *Handbook of Optical Constants of Solids II*. Academic Press, Inc.: 1991.

7. Jian-Hua, M.; Xiang-Jian, M.; Tie, L.; Shi-Jian, L.; Xiao-Dong, Z.; Jing-Lan, S.; Jun-Hao, C., Structural and electrical properties of SrTiO<SUB>3 thin films as insulator of metal-ferroelectric-insulator-semiconductor (MFIS) structures. *Chinese Physics* **2005,** 14, 2352-2359.

8. SCI, *FilmTek (TM) 3000SE Operations Manual*. Scientific Computing International: 2006.

9. Yu, P. Y.; Cardona, M., *Fundamentals of Semiconductors*. Springer, Berlin: 1996.

10. Zollner, S.; Demkov, A. A.; Liu, R.; Fejes, P. L.; Gregory, R. B.; Alluri, P.; Curless, J. A.; Yu, Z.; Ramdani, J.; Droopad, R.; Tiwald, T. E.; Hilfiker, J. N.; Woolam, J.

A., Optical properties of bulk and thin-film $SrTiO_3$ on Si and Pt. *J. Vac. Sci. Technol. B* **2000,** 18, (4), 2242 - 2254.

11. Deng, Y.; Du, Y. L.; Zhang, M. S.; Han, J. H.; Yin, Z., Nonlinear optical properties in SrTiO3 thin films by pulsed laser deposition. *Solid State Communications* **2005,** 135, (4), 221-225.

12. Gaidi, M.; Stafford, L.; Amassian, A.; Chaker, M.; Margot, J.; Martinu, L.; Kulishov, M., Influence of the microstructure on the optical characteristics of $SrTiO_3$ thin films. *Journal of Materials Research* **2005,** 20, 68 - 74.

13. Zollner, S.; Demkov, A. A.; Liu, R.; Curless, J. A.; Yu, Z.; Ramdani, J.; Droopad, R., Optical Properties of Thin Film $SrTiO_3$ on Si Grown by MBE. *Material Research Society Symposium Proceedings - Recent Developments in Oxide and Metal Epitaxy: Theory and Experiment* **2000,** 619, 161-171.

CHAPTER 6: Assessment of Morphological and Optical Properties of Molecularly Mediated Thin Film Assembly of Gold Nanoparticles

Lingyan Wang,† Dionne Miller,‡ Quan Fan,† Jin Luo,† Mark Schadt,† Qiang Rendeng,† Guannan Roger Wang,† Jianguo Wang,§ Glen R. Kowach,‡ and Chuan-Jian Zhong*,†

†Department of Chemistry, State University of New York at Binghamton, Binghamton, New York 13902,

‡Department of Chemistry, City College of New York, New York, New York 10031, and §Science and Technology Division, Corning Inc., Corning, New York 14831

6.1 Abstract

This paper reports the results of an investigation of the optical properties of molecularly mediated thin film assemblies of nanoparticles. Thin film assemblies of gold nanoparticles of different sizes that are linked by dithiols and carboxylic acid functionalized thiols of different alkyl chain lengths are studied as a model system. These thin films have been assembled on different substrates for the systematic measurements of the morphological and optical properties. The correlation of the *d*-spacing values between the experimental and theoretical results has revealed the presence of ordered nanostructures in the thin film assemblies. The wavelength of the surface plasmon resonance band of the nanoparticles in these thin film assemblies is shown to be linearly dependent on the particle size and the interparticle linker chain length. The analyses of the optical properties theoretically using Mie theory and experimentally using reflectometry and spectroscopic ellipsometry have provided

important information for the assessment of the optical constants for these nanostructured thin films. Implications of the results to the understanding of the interparticle structural properties are also discussed.

6.2 Introduction

The design and fabrication of nanoparticle-based materials have been investigated in many cutting-edge areas of nanoscience and nanotechnology, including microelectronics, molecular recognition, catalysis, and chemical/biological sensing.[1-10] Metallic nanoparticles such as gold, silver, and copper have attracted widespread interest in these areas because of their unique optical and electronic properties at the nanoscale dimension. These properties depend on the size, shape, composition, interparticle, and surface properties.[1] We have demonstrated the capabilities not only in synthesizing highly monodispersed gold nanoparticles but also in assembling them into thin films via a mediation-templating route with electrical and optical properties fine-tunable in terms of size, composition, and spatial properties.[2-4] A general strategy for the thin film assembly involves an initial exchange of thiols with thiolates [e.g., decanethiolate (DT)-capped Au] in solution followed by cross-linking via either intercore Au-S bonding [e.g., using alkyl chain dithiol (ADT)] or intershell hydrogen-bonding (e.g., using acid-functionalized thiol).[4] In contrast to the stepwise route,[5-9] this assembly route is a simple one-step process applicable to almost any substrate. The measurements of both the mass change and the surface plasmon resonance band evolution[2a] demonstrated that the thickness of the film is characteristic of multilayer morphology and can be controlled by

concentrations of the nanoparticles and assembling time. The film assemblies have been shown to function as highly sensitive materials on chemiresistive or piezoelectric platforms for chemical sensing.[10]

While the thin film assemblies have been shown to display thermally activated electrical conductivity property,[11, 12] which is tunable in terms of particle size, chain length, and functionality, the study of the optical properties is rather limited. The surface plasmon (SP) resonance band of gold nanoparticles is one important phenomenon due to the collective oscillation of electrons confined in these metallic nanoparticles.[13,14] The exploitation of the optical properties has been reported for chemical and biological applications.[5,15,16] For example, free-floating target DNA strands can be detected by colorimetric detection with complementary DNA linked to gold nanoparticles for specific DNA sequences.[15] The target strands bind to the gold-bound complementary strands and form an assembly of the gold nanoparticles, and the change of the color serves as the means of detection.[15a] This strategy has been widely exploited for the development of DNA detection methods.[15,16] Gold nanoparticle multilayers formed via step-by-step assembly of molecular linkers and nanoparticles have also been shown to be useful for constructing thin films as optical biosensors.[5,16]

Despite many promising applications demonstrated for various assemblies of nanoparticles, the understanding of how the interparticle spatial parameters are correlated with the SP band properties is limited, especially for molecularly mediated thin film assemblies. One of the challenges is the lack of well-defined thin film assembly of nanoparticles with controllable interparticle spatial properties. The recent

demonstrations of the capabilities both in synthesizing highly monodispersed gold and gold-silver nanoparticles and in assembling them into thin films of controlled particle size and interparticle spatial properties[2-4,7-10] have provided us the opportunity to address this challenge. This report describes the findings of a systematic study of the morphological and optical properties of the molecularly mediated thin film assemblies of nanoparticles. This study focuses on the assessment of the correlation of the optical parameters with the size of the nanoparticles and the chain length of the linker molecules. It is important to emphasize that while the previous studies reported the concept of controlling interparticle spacing using a similar linking mechanism, it used an assembly method[7-9] that is different from our one-step assembly approach.[2,4,10,17] There has been no systematic correlation between the surface plasmon resonance band properties of such thin film assemblies as in our approach and the interparticle chain length spacing or particle size. In this report, we used several techniques to characterize the thin films assembled by our one-step assembly approach and obtained new results that have not been reported previously in terms of the systematic correlation.

6.3 Experimental

Chemicals. Hydrogen tetrachloroaurate trihydrate (HAuCl4.3H2O, 99%), tetraoctylammonium bromide (TOA+Br-, 99%), Decanethiol (DT, 96%), sodium borohydride (NaBH4, 99%) were purchased from Aldrich. 11-mercaptoundecanoic acid (MUA) and Alkyl dithiols (ADT, HS-(CH2)m-SH) included 1,3-propanedithiol (PrDT, m=3, 99%), 1,5-pentanedithiol (PDT, m=5, 96%), 1,8-Octanedithiol (ODT,

m=8, 97%), 1,9-nonanedithiol (NDT, m=9, 95%), which were purchased from Aldrich and used as received. 1,10-decanedithiol (DDT, m=10, 90%) was purchased from TCI and used as received. Solvents included hexane (99.9%) and toluene (99.8%) from Fisher, and ethanol (99.9%) from Aldrich. Water was purified with a Millipore Milli-Q water system.

Synthesis of Gold Nanoparticles (Aunm). Gold nanoparticles of 2 nm (Au2nm) core size encapsulated with decanethiolate (DT) monolayer shells were synthesized by two-phase reduction of $AuCl_4$- according to Brust's method[7] and a synthetic modification.[3] Details for the synthesis of our gold nanoparticles (2.0 ± 0.7 nm core size) were previously described.[3] Gold nanoparticles with larger sizes were synthesized by a thermally-activated processing route developed in our laboratory.[3] The procedures include following solvent evaporation, the Au2nm-DT nanoparticles and other reactants and products from the synthesis solution were dissolved quantitatively in toluene giving a stock solution with known concentrations of Au2nm-DT particles, free DT, and TOA-Br. The reaction container was placed in a preheated oven set at 145 °C ~150 °C. After 1-hour thermal treatment, the container removed from the oven and allowed to cool before dissolving the nanoparticles in the mostly solid mixture in toluene. The products washed by ethanol and separated by centrifuge. Finally products were re-dispersed in hexane. Gold nanoparticles of 4 nm, 5 nm, and 6nm are denoted as Au4nm, Au5nm, and Au6nm, respectively.

Preparation of Thin Film Assembly. The general preparation of the thin films followed the one-step exchange-crosslinking-precipitation method reported for gold.[2,4] Briefly, it involved immersion of substrates (e.g., glass, electrodes etc.) into a

mixture of hexane solution of DT-capped Aunm (30 μM) with hexane solution of ADT (50 mM) or ethanol solution of MUA (20mM) for the thin film assembly. The reaction was carried out at room temperature. ADT and MUA function as a mediator or cross-linking agent. The mediator to nanoparticle ratio was controlled, typically the Au nanoparticle to ADT ratio was about 1:50-500 (~1:50 for PrDT, 1:500 for PDT, ODT, NDT, DDT) for 2.0 nm Au, and about 1:400 ~ 4000 (~1:400 for PrDT, 1:4000 for PDT, ODT, NDT, DDT) for larger sizes Au nanoparticle. Typical MUA to nanoparticle ratios were 50-500. The pre-cleaned substrates (glass and silicon wafer) were immersed vertically into the assembly solution to ensure that the film formed was free of powder deposition. At a controlled immersion time, the film-deposited substrates were immersed and immediately rinsed thoroughly with hexane and dried under nitrogen before the characterization. The chain length for the thin films is denoted according to the number of $-CH_2-$ units (m) in ADT. The films were uniform and the thickness could be controlled.

Instrumentation and Measurements. A Multimode NanoScope IIIa (Digital Instruments) was utilized for Atomic Force (AFM) imaging. The Tapping Mode (TM)-AFM with standard silicon cantilevers (Nanoprobes) were used. The instrument was calibrated by imaging standard grating samples. Transmission electron microscopy (TEM) was performed on Hitachi H-7000 electron microscope (100 kV). The nanoparticle samples dispersed in hexane solution were cast or assembled onto a carbon-coated copper grid sample holder, followed by evaporation at room temperature. X-ray Powder Diffraction (XRD) was studied on a Scintag XDS 2000 θ-θ powder diffractometer equipped with a Ge (Li) solid-state detector (Cu Kα

radiation). The data were collected from $2\theta = 2\text{-}6°$ at a scan rate of 0.02° per step and 100 s per point. Grazing angle XRD data were obtained from Philips X'PERT-MRD X-ray diffractometer with grazing angle capability for studying thin films. UV-Vis spectra (UV-vis) were acquired with a HP 8453 spectrophotometer. The optical band measured is characteristic of the surface plasmon resonance band of the nanoparticles or nanoparticles thin films. Nanoparticle thin film samples were deposited on glass slides (cover glass) and solution samples were prepared using hexane as solvent. Both were measured in transmission mode and were collected over the range of 200-1100 nm. Reflectometry and spectroscopic ellipsometry were used to determine the optical constants such as refractive index and extinction coefficient. The thin films were assembled on silicon wafers bearing ~2000 Å of silicon dioxide. The thin film assemblies were analyzed by multiple angle reflectometry (0° and 70°) and spectroscopic ellipsometry using a Scientific Computing International (SCI) FilmTek 3000SE.

6.4 Results and Discussion

6.4.1 Morphological Properties

While the general morphological properties of some of the thin film assemblies of gold nanoparticles were discussed previously,[2, 4] this section provides a detailed discussion of the thin film uniformity and the crystalline structure based on Tapping Mode (TM)-AFM and X-ray diffraction techniques. AFM allows imaging of the thin film surface morphology with a minimum disruption of the nanostructures, whereas XRD permits probing of the nanoparticle ordering in the thin film.

For the thin films studied in this work, a typical set of AFM images is shown in the Figure 6.1 for NDT-Au_{2nm} (A) and MUA-Au_{6nm} films assembled on a (B) gold coated mica and (C) silicon wafer substrate, respectively. While there are domains of apparent inhomogeneity partly due to the surface roughness effect of substrates, the overall surface morphology indicates a uniform and smooth feature. The size of the nanoparticles determined from the *x-y* plane appears somewhat larger than the core-shell nanoparticle size due to tip-sample convolution, but a cross-section view reveals an average height closed to the expected particle sizes. For NDT-Au_{2nm} thin film on gold-coated mica (Figure 6.1 (A)), the cross-section analysis of vertical distance yields an average value of ~2.2 nm; for MUA-Au_{6nm} thin film on gold-coated mica (Figure 6.1 (B)), the cross-section analysis of vertical distance yields an average value of ~7.3 nm; for MUA-Au_{6nm} thin film on silicon (Figure 6.1 (C)), the cross-section analysis of vertical distance yields a value of ~ 4.3 nm. These values are expected from a model analysis for the nanoparticle thin film assembly. Similar surface morphology has also been observed for both NDT-Au_{2nm} and MUA-

Au_{6nm} films.[2, 4] We note that the thickness of MUA-Au_{6nm} thin film on silicon for AFM measurement was usually thicker than that for the reflectometry and spectroscopic ellipsometry measurement as described in a late subsection.

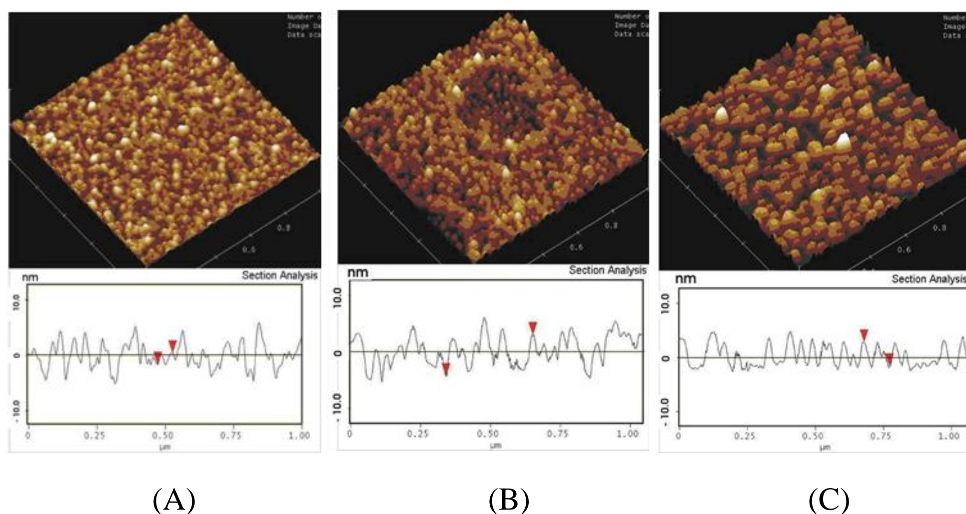

(A) (B) (C)

Figure 6.1: AFM images of (A) NDT-Au_{2nm} thin film on gold-coated mica, (B) MUA-Au_{6nm} thin film on gold-coated mica, and (C) MUA-Au_{6nm} thin film on silicon. The bottom panels show the corresponding cross-section analysis results.

To determine the nanostructured ordering in the thin film assemblies, both small angle and grazing angle XRD techniques were used. The thin films were assembled on silicon wafer or glass substrates. The general patterns, as discussed in the following descriptions of the results shown in Figure 6.2 confirm that the assembled thin films by different linking molecules have ordered structures with different *d*-space features. The results of the *d*-spacing (*d*) parameters for each of the thin films obtained based on Bragg equation, $2d\sin\theta = n\,\lambda$ (λ = 1.54056 Å), are summarized in Table 6.1.

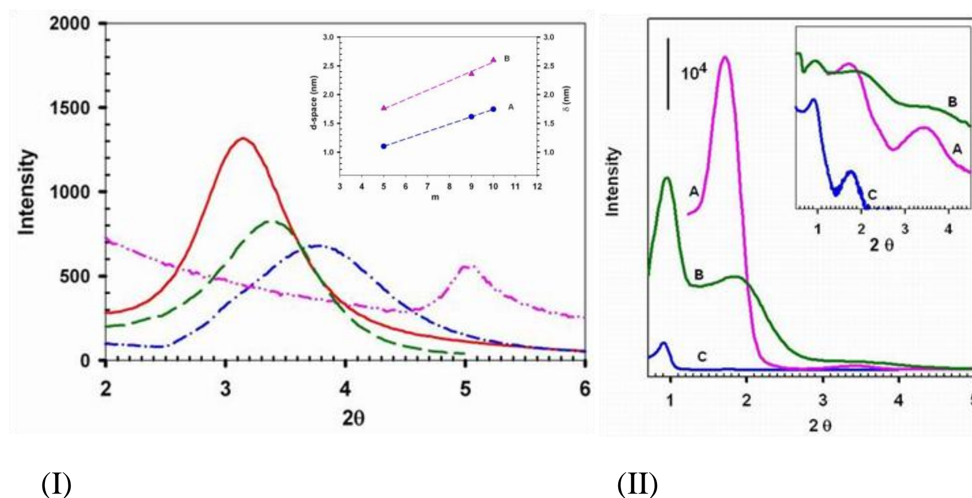

(I) (II)

Figure 6.2: (I). Small angle XRD data for thin film assemblies of Au_{2nm}: MUA-Au_{2nm} (red, solid line), DDT-Au_{2nm} (green, dash line), NDT-Au_{2nm} (blue, dash-dot line), PDT-Au_{2nm} (pink, dash-dot-dot line); Insert: Plots of the calculated edge-to-edge distance (δ) based Chem. 3D (A) and based on XRD data (B) vs. the number of methylene groups (m) in the alkyl chain of the linking molecules. Linear regression slope = 0.13 (R^2=1) (A) and 0.16 (R^2=0.99) (B). (II) Small angle (A & B) and grazing angle (C) XRD patterns for thin film assemblies of Au 5nm on glass substrates: (A) MUA-Au_{5nm} thin film measured by small angle XRD, (B) PDT-Au5nm measured by small angle XRD, (C) MUA-Au_{5nm} measured by grazing angle XRD; Insert: A close comparison of the peak positions (Log (Intensity) as y axis).

Figure 6.2(I) and Table 6.1 show the data for thin film assemblies of Au_{2nm} by ADT linkers of different chain lengths. Important information can be extracted from the analysis of the peak shift and *d*-spacing data. The shift of the XRD peaks shows that the increase in the chain length of the interparticle linking molecule leads to decrease the 2θ value, which is clear indication of the increase of the *d*-space value. By comparing these ADT- linked thin films, it is remarkable that the *d*-spacing value increases linearly with the number of methylene units in the alkyl chains (Figure 6.2(I) insert). These thin film assemblies linked by ADTs clearly exhibit certain ordering in the film in which the chain length of the linking molecules plays an important role in the interparticle spatial properties. Interestingly, the data

for the thin film assemblies linked by MUA (MUA-Au_{2nm}) do not fall in the same linear trend as observed for the ADTs, which likely reflects the interparticle structural difference between these two types of thin film assemblies.[2c] In addition, the XRD peaks are found to be independent of the nature of the substrate. The *d*-spacing values obtained for NDT-Au_{2nm} thin films on silicon substrate were basically identical to those obtained with glass substrate (not shown in the Figure 6.2(I)), demonstrating that the nanostructural ordering properties are characteristic of the thin film assemblies of gold nanoparticles.

Table 6.1: XRD results of thin film assemblies of gold nanoparticles

Sample	2θ	d-space (nm)	δ from calc.[g] (nm)	δ from TEM[h] (nm)
PDT-Au_{2nm}[a]	5.03	1.76	1.10	
NDT-Au_{2nm}[b]	3.74	2.36	1.62	
NDT-Au_{2nm}[a]	3.68	2.40	1.62	
DDT-Au_{2nm}[a]	3.40	2.60	1.75	
MUA-Au_{2nm}[a]	3.15	2.80	3.15	
PDT-Au_{5nm}[a,c]	1.9	4.64	1.10	
PDT-Au_{5nm}[a,d]	0.90	9.81	1.10	
MUA-Au_{5nm}[a]	1.72	5.13	3.15	1.2
MUA-Au_{5nm}[a,e]	1.76	5.02	3.15	1.2
MUA-Au_{5nm}[a,f]	0.82	10.8	3.15	1.2

[a] On glass. [b] On silicon. [c] Based on peak 1. [d] Based on peak 2. [e] Based on grazing-angle XRD, peak 1. [f] Based on grazing-angle XRD, peak 2. [g] Edge-to-edge distance (δ) derived from calculation.[17] [h] Edge-to-edge distance (δ) measured from TEM data. [2c]

Figure 6.2(II) and Table 6.1 shows a representative set of XRD data for the thin film assemblies of Au_{5nm} on the glass substrates, revealing several pieces of information. First, for the same MUA-Au_{5nm} thin film, the relative intensity of the two peaks (peaks at $2\theta = 0.82$ and 1.76) observed from the small angle XRD (Figure 6.2(II)B) is smaller than those from the grazing angle XRD (Figure 6.2(II)C). This is

due to the difference of the two techniques. Second, the *d*-spacing value for MUA-Au_{5nm} thin film from the small angle XRD is consistent with that from the grazing angle XRD. This demonstrates that the *d*-spacing value is characteristic of the thin film structure. Third, the *d*-spacing value for PDT-Au_{5nm} thin film is smaller than that of MUA-Au_{5nm} thin film. This is consistent with the difference of chain length between the two linker molecules.

In a previous TEM study of the thin film assembly,[2c] a monolayer of nanoparticles on the substrate was confirmed to exhibit close packed layer with well-defined interparticle distance (δ). Figure 6.3A shows a TEM image for a MUA-Au_{6nm} assembly, in which both the first layer and the second layer of nanoparticles can be clearly visualized.

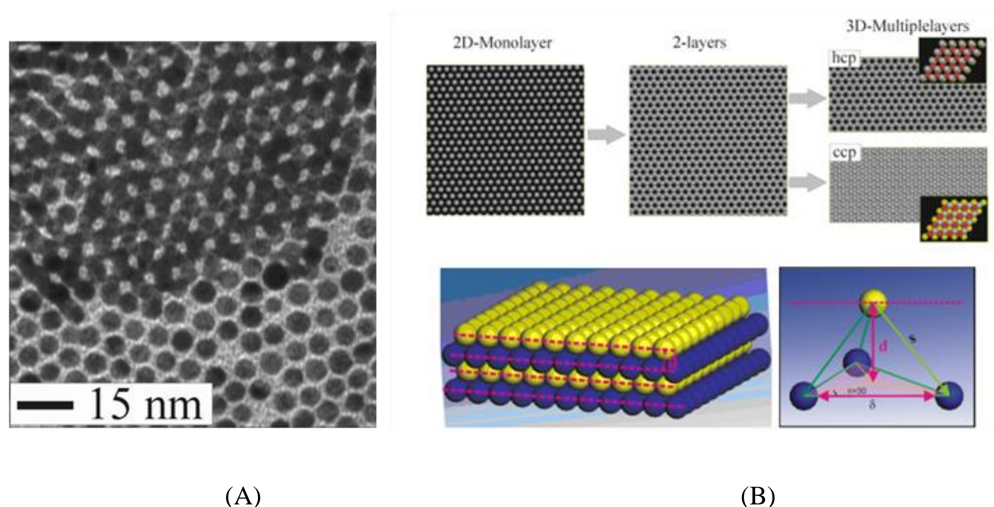

(A) (B)

Figure 6.3: (A) TEM of a MUA-Au_{6nm} assembly. (B) Illustrations of idealized models for 2D and 3D packing of nanoparticles in the thin film assemblies. (B, top) Top view of hcp and ccp close-packing; (B, bottom) particles positioning in between three particles.

On the basis of the dense-packing model, the layer-to-layer distance (*d*-spacing), the edge-to-edge distance (δ), and the particle radius (*r*), where θ = 30°, can be related to the center-to-center distance (*s*) of the nearest two particles in the two neighbored

layers $[((\delta/2 + r)/\cos\theta)^2 + d^2 = s^2$, where $\theta = 30°]$. Considering $s = \delta + 2r$, the *d*-spacing equation can be derived as

$$d = (\delta + 2r)\sqrt{\frac{2}{3}} \quad (6.1)$$

Table 6.2 compares the *d*-spacing values between those calculated from the packing models and those from the XRD measurements. It is apparent that the *d*-spacing values from the model-based calculation are generally larger than those determined from XRD measurements. The exact origin for the deviation is not clear at this point. There is possibly a compromised balance between the interparticle linking and the interparticle templating interactions that may have played an important role in producing a tighter packing than the packing in the idealized models. In our previous reports,[2c,10c,17] we discussed the interparticle spatial and structural effects on the relative change of the electrical conductivity due to the relative length differences of the interparticle $-(CH_2)_n-$ structures defined by both mediating (or linking) and capping (or templating) molecules. When the linking molecular length falls in the vicinity of the capping (e.g., DT), well-interdigitated mediating/capping alkyl structures are expected. For shorter or longer linking molecules, the alkyl chains are not expected to be well-interdigitated, and thus a difficult or loose interparticle chain-chain cohesive interdigitation is possible.

The comparison of d-spacing values for MUA-Au5nm reveals that the *d*-spacing value calculated from the packing models based on edge-to-edge distance δ determined from TEM measurement is quite close to that determined from the XRD measurement. While a further in-depth delineation of these experimental and theoretical *d*-spacing values is needed, the above results clearly demonstrate the

presence of ordered nanostructures in the thin film assemblies.

Table 6.2: Comparison of *d*-spacing values

Sample	*d*-space (nm)		
	From XRD	Cal'd [g]	Cal'd [h]
PDT-Au_{2nm} [a]	1.76	2.53	-
NDT-Au_{2nm} [b]	2.36	2.95	-
NDT-Au_{2nm} [a]	2.40	2.95	-
DDT-Au_{2nm} [a]	2.60	3.06	-
MUA-Au_{2nm} [a]	2.80	4.20	-
PDT-Au_{5nm} [a,c]	4.64	4.98	-
PDT-Au_{5nm} [a,d]	9.81	-	-
MUA-Au_{5nm} [a]	5.13	6.65	5.06
MUA-Au_{5nm} [a,e]	5.02	6.65	5.06
MUA-Au_{5nm} [a,f]	10.8	-	-

[a-f] See footnotes of Table 6.1. [g] Based on eq. 1 using the δ value obtained from Chem 3D modeling.[16] [h] Based on eq 1 using the δ value obtained from the TEM data.[2c]

6.4.2 Optical Properties

6.4.2.1 *Dependence of Surface Plasmon Resonance Band on Interparticle Spatial Properties*

In our previous reports,[2a,c] the surface plasmon (SP) band of gold nanoparticles was shown to exhibit a red shift upon assembly into a thin film. In the present paper, this shift was systematically studied in detail, especially focusing on the dependencies of the shift on the chain length of the linker molecules and the size of the particles.

Figure 6.4 shows a representative set of UV-Vis spectra for the dependence of the SP band shift on the size of the particles (A to D).

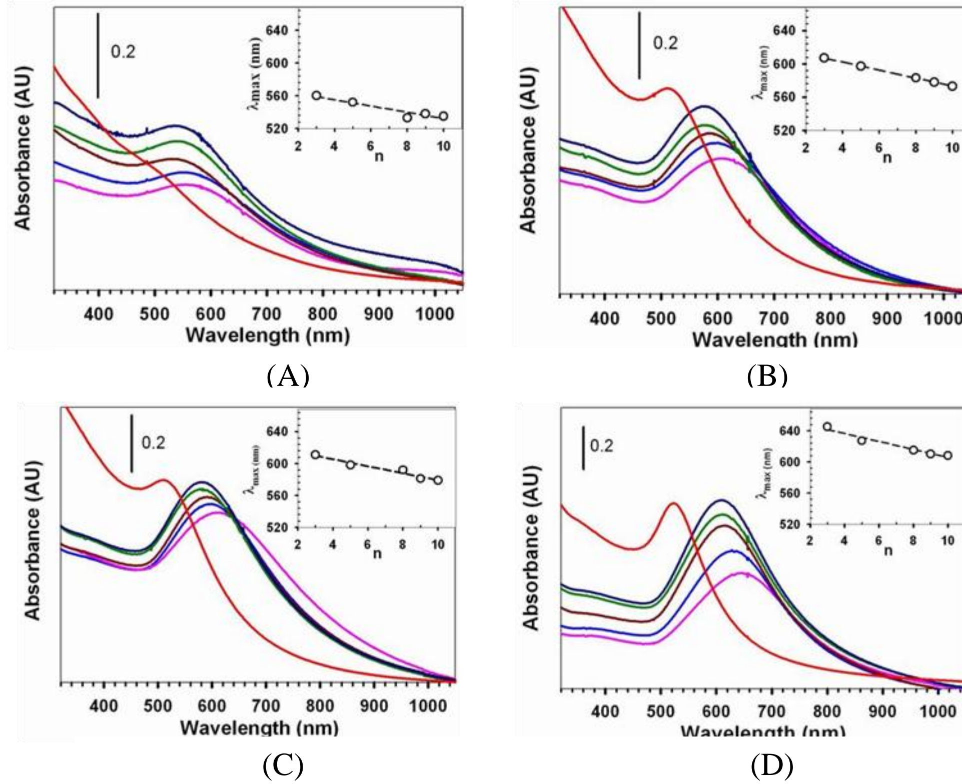

Figure 6.4: UV-vis spectra of the thin film assemblies of gold nanoparticles of different sizes on glass substrates: Au_{2nm} (A), Au_{4nm} (B), Au_{5nm} (C), and $Au\text{-}_{6nm}$ (D). In each case, the spectra were measured as a function of the chain length of the linker molecules: m=3 (pink), m=5 (light blue), m=8 (dark red), m=9 (dark green), and m=10 (dark blue). The spectra for the corresponding gold nanoparticles in hexane solution (red) were included for comparison.

In each case, the SP band was measured as a function of the chain length of the linker molecules. It is evident that the shift of the peak maximum of the SP band (λ_{max}) is dependent on both the particle size and the interparticle spacing. Such dependencies are plotted in Figure 6.5 for the comparison of the actual λ_{max} values. First, the SP band is shown to increase with particle sizes (Fig 6.5b). Second, the SP band shift exhibits a linear relation with the chain length for all particle sizes studied. Remarkably, the slopes for these λ_{max}-m and λ_{max}-2r plots are quite similar for the

thin film assemblies of different particle sizes with different linker lengths.

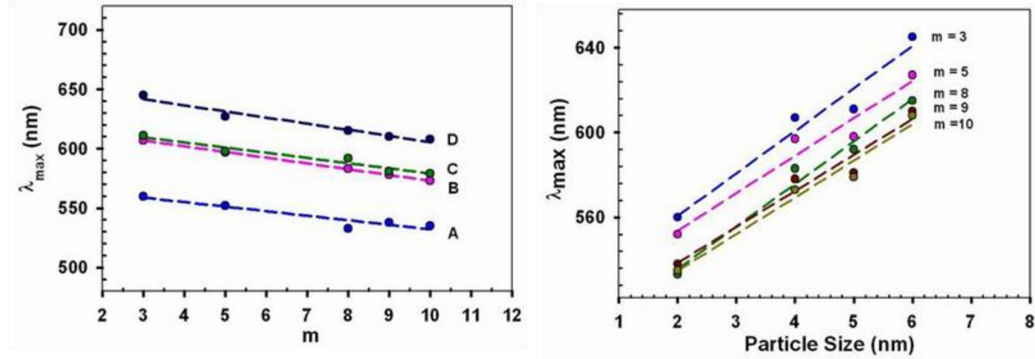

Figure 6.5: (a) Plot of SP band λ_{max} vs. chain length (*m*) for thin films of four different particle sizes: Au_{2nm} (A, light blue), Au_{4nm} (B, pink), Au_{5nm} (C, green), and Au_{6nm} (D, dark blue); (b) Plot of SP band λ_{max} vs. particle size (2*r*) for thin films with different linker chain lengths.

To understand the correlation of the SP band evolution with particle size, interparticle distance, and dielectric medium properties, Mie theory was considered as a simple model to compare the SP spectra. The simulation of the extinction coefficient (γ) is based on the following equation for small spheres:[18]

$$\frac{\gamma}{NV} = \frac{18\pi\varepsilon_{\alpha}^{3/2}}{\lambda} \times \frac{\varepsilon_2}{(\varepsilon_1 + 2\varepsilon_{\alpha})^2 + \varepsilon_2^2} \qquad (6.2)$$

where *N* is the number of spheres per unit volume, *V* is the volume of each sphere, *NV* is the volume concentration of the particles, λ is the wavelength of light in a vacuum, ε_{α} is the dielectric constant of the surrounding medium, and ε_1 and ε_2 are the real and complex parts of the dielectric function of Au. The dielectric medium constant (ε) is related to refractive index (n), i.e., $(n + ik)^2 = \varepsilon$, and the evolution of the SP band is recently shown to increase with the refractive index for nanoparticles in the assembly.[19] We next examine how these changes in particle size and interparticle distance are related to changes in the interparticle refractive index or dielectric

medium constant.

In Figure 6.6A, the simulated absorbance spectra were compared for ADT-Au_{4nm} films derived from different chain lengths. The spectra were simulated based on Mie theory by changing the refractive index (*n*). In the simulation, the general trend for the spectral shift is fitted to the experimentally observed spectra. The change in *n* (Δn) measures the difference of the refractive index between the surrounding medium of the nanoparticles in the thin film assembly and that of the solvent environment of the nanoparticles in the solution before the assembly. The value of Δn was found to exhibit an approximate linear relationship with the chain length (Figure 6.6B). Δn decreases with chain length. Remarkably, the linear relationship displays similar slopes for the different particle sizes that have been studied. The change in refractive index decreases with the interparticle spacing, and increases with the particle size.

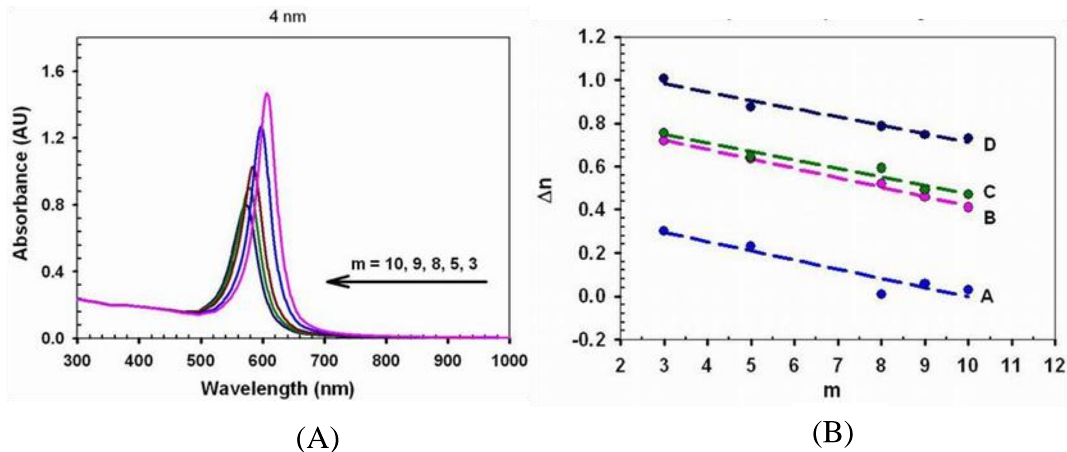

(A) (B)

Figure 6.6 (A) Simulation of SP band (based on Mie theory) for ADT-Au_{4nm} thin film: m=3 (pink), m=5 (light blue), m=8 (dark red), m=9 (dark green), and m=10 (dark blue). (B) Simulation results: the change of refractive index (Δn) used in the simulation vs. λ_{max} for ADT thin films of Au_{2nm} (A, light blue), Au_{4nm} (B, pink), Au_{5nm} (C, green), and Au_{6nm} (D, dark blue).

The experimentally obtained spectra were further analyzed using Mie theory in terms of the dielectric constant (ε) property. Figure 6.7A shows a set of simulation results by directly applying equation 2 to fit the experimental data. In the simulation, the spectral shift is fitted to the experimental observation using different ε values. In comparison with the linear relationship for the refractive index change, the value of ε was found to exhibit an exponential decay type of decrease with the chain length (Figure 6.7A). Similarly, the value of ε decreases with the interparticle spacing, and increases with the particle size.

We also used a modified Mie theory[20] to analyze the data for assessing the correlation of the interparticle dielectric medium constant properties with the interparticle distance and particle size. In the modified Mie theory,[20]

$$T_{film} = \frac{(1-R)^2 + 4R\sin^2\psi}{R^2\exp(-\alpha d) + \exp(\alpha d) - 2R\cos(\zeta + 2\psi)} \qquad (6.3)$$

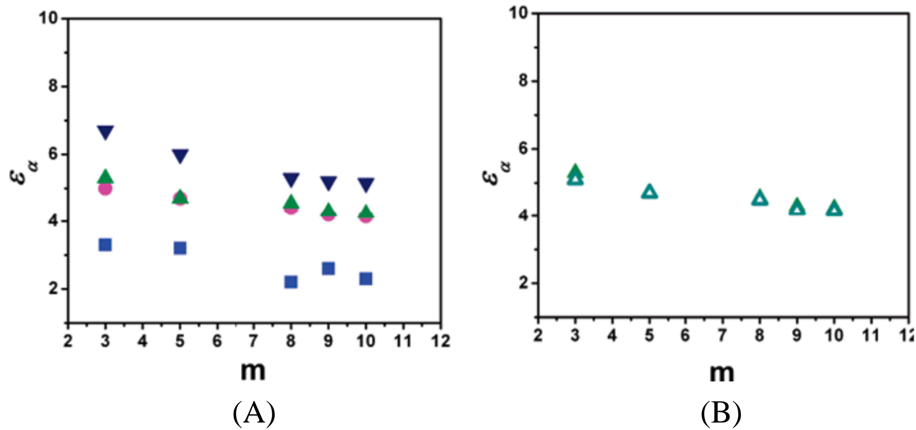

Figure 6.7: (A) Simulation of SP band for ADT-Au_{nm} thin film based equation 3: Au_{2nm} (dark square), Au_{4nm} (red, circle), Au_{5nm} (green triangle up), and Au_{6nm} (blue triangle down). (B) Simulation of SP band for ADT-Au_{5nm} thin film based equation 6.3(closed triangle). The simulation data based on equation 6.2 are included for comparison (open triangle).

T_{film} is light transmission, R is the reflectance at normal incidence which is related to the effective dielectric function (ε_{av}) for the metal nanoparticles. The variates ζ, α and ψ are related to ε_{av}, thickness of the nanoparticle ensemble (d) and λ. ε_{av} is related to the ε_1, ε_2, ε_α, and the volume fraction of the particles (ϕ). Briefly, the light transmission T_{film} is related to ε, d, and ε_α. The theoretical analysis of the SP band data was recently shown to provide useful insights into the interparticle properties.[20] Figure 6.7B shows a set of simulation results by directly applying equation 6.3 to fit the experimental data for ADT-Au_{5nm} thin films. In comparison with the simulation data based on equation 6.2, a very similar trend was observed for the change of the value of ε. Similar results have also been obtained for the other particle sizes. It is clear that the value of ε decreases with the interparticle spacing.

6.4.2.2 *Optical Analysis by Ellipsometry and Reflectometry*

To further assess the optical properties, the index of refraction and extinction coefficient were measured by reflectometry and ellipsometry. The thin films were assembled on silicon wafers bearing ~2000 Å of silicon dioxide and were analyzed by multiple angle reflectometry (0° and 70°) and spectroscopic ellipsometry. Data were analyzed using a multiple parameter regression analysis based on a coupled oscillator Lorentz model for gold. The analysis of the blank sample (silicon/silicon dioxide substrate) gave the average thickness of the SiO_2 layer as 2074Å and a refractive index, n of 1.4638 at 632 nm (2 spots measured).These values were used as non-varying parameters in the film analysis. Fits to the data were obtained with a root mean square error (RMSE) of 2.861 and 2.831

A set of results of NDT-Au_{2nm} and PDT-Au_{2nm} thin films is shown in Table 6.3 and Figure 6.8. For NDT-Au_{2nm} thin film, two spots were measured and the data analyzed over the spectral range of 420 – 920 nm. The model assumes an average thickness over the entire probed area (spot size 1 x 3 mm). The results indicate a film with an average thickness of approximately 33 nm; no effective medium approximation (EMA) layer was used to evaluate roughness. For PDT-Au_{2nm} thin film, three spots were measured and the data analyzed over a truncated range of 400 – 920 nm. All three spots have similar thickness, which implies that the film is very uniform. These optical constants of the thin films were compared. The refractive index (*n*) is found to increase with the thickness of the thin films with the same linking molecule. A comparison of the results between NDT-Au_{2nm} and PDT-Au_{2nm} thin films shows that the thin film with short chain length has a higher refractive index (*n*) and extinction coefficient (*k*) values than that with a long chain length. This is true even though the PDT-Au_{2nm} film is thinner than the NDT-Au_{2nm} film.

Table 6.3: The Optical Data of NDT-Au_{2nm} and PDT-Au_{2nm} Thin Films Assemblies

Sample	Thickness/ Å	N	K	Layers*
NDT-Au_{2nm}				
Spot 1	576.87	1.82015	0.25080	24
Spot 2	695.63	1.86412	0.25589	29
Average	636.25	1.842135	0.256945	26.5
PDT-Au_{2nm}				
Spot 1	322.57	1.90492	0.33330	18
Spot 2	327.29	1.90642	0.32422	18
Spot 3	336.94	1.92744	0.32035	19
Average	328.93	1.91293	0.32596	18.3

* Based on d-spacing value from XRD data in Table 6.1

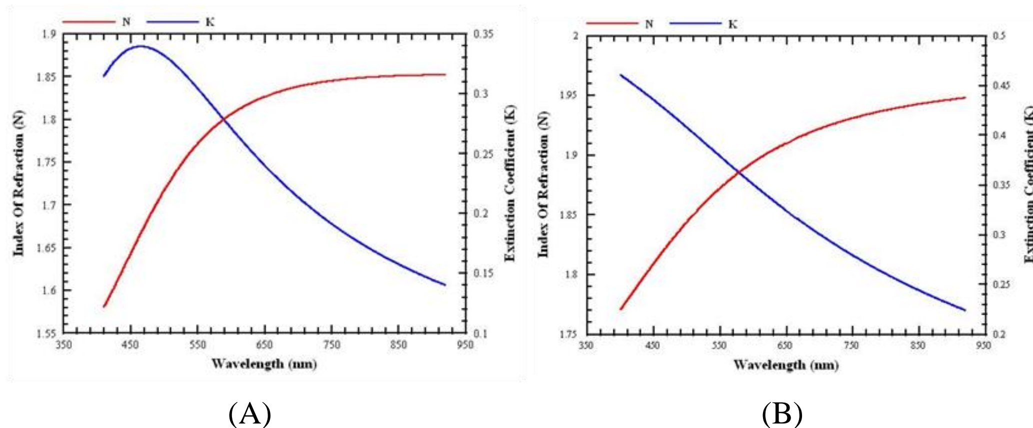

(A) (B)

Figure 6.8: Plots of wavelength vs. refractive index and extinction coefficient for (A) NDT-Au_{2nm}, and (B) PDT-Au_{2nm} thin films.

On average, the determined optical constants, *n* and *k*, are slightly larger for PDT-Au_{2nm} film than those for NDT-Au_{2nm} film. This trend is qualitatively consistent with the simulation results based on Mie theory.

We also note that there is some difficulty with the data fitting in the low wavelength region for films whose average thickness was greater than approximately 20 nm. This difficulty may have been partly due to the roughness of the films and partly due to the relatively high organic concentration of crosslinking molecules which results in significant absorption in the low wavelength region. The model used did not attempt to account for optical absorption of these species. In contrast to the data for the PDT-Au_{2nm} film (Figure 8-10B), the increased film thickness and the associated higher Au nanoparticle concentration could be responsible for the origin of the peak observed in the *k* spectrum for the NDT-Au_{2nm} film (Figure 8-10A), which appears at a wavelength slightly lower that the surface plasmon resonance band of gold nanoparticles (~ 490 nm).

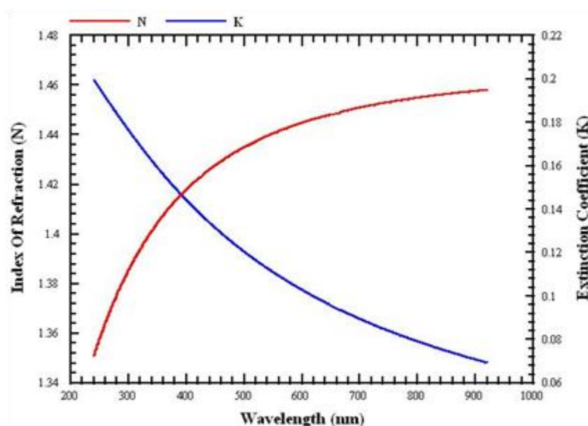

Figure 6.9: Plot of wavelength vs. refractive index and extinction coefficient for MUA-Au_{6nm} thin film.

For MUA-Au_{6nm} thin film (Figure 6.9), the data fitting was obtained with a RMSE of approximately 2, typical of an excellent fit. The average thickness of the nanoparticle thin film was found to be 56.0 ± 3.5 Å with a refractive index, *n* of 1.4428 ± 0.0200 and an extinction coefficient, *k* of 0.1076 ± 0.0100 measured at 632 nm. The average thickness determined was somewhat below the diameter of the nanoparticles which could reflect that part of the surface was not completely covered with the thin film in this particular sample. There are several reports on the optical constants of nanoparticle thin films prepared differently. For example, measurements of the refractive index of gold nanocrystal (~10 nm size)/silica films (thickness 110-150 nm) spin-coated onto Si wafers with different loading factors of gold have been reported.[22] The refractive index values were found to range from 1.46 to 1.70 with increased loading factors. Spectroscopic ellipsometry has also been reported to determine optical constants of colloidal gold films (colloid diameter ~ 13.2 nm) self-assembled onto derivatized Si/SiO_2 substrates.[23] The refractive index values were

found to range from approximately 1.09 to 1.21 for different surface coverages. We note that the bulk value of the refractive index (*n*) of gold at 619.9 nm is 0.194 with an extinction coefficient (*k*) of 3.15 at 652.6 nm.[24] However, thin films are known to behave very differently from bulk samples, and many factors such as deposition parameters, sample quality, etc. will affect the results obtained from different thin films. In comparison with the values reported for the nanoparticle thin films, the fact that the refractive index values determined for our thin films (1.4-1.9) were somewhat higher could reflect the structural difference of our thin film assembly. One of the unique aspects of our thin films is the interparticle molecular linkage and templating interactions. The interparticle spatial properties defined by the linking/templating molecules may have played an important role in increasing the overall refractive index value, as supported by the simulation results based on Mie theory. Further correlation between the refractive index and the interparticle structure is part of our ongoing work.

6.5 Conclusion

In conclusion, the results of the systematic measurements of the molecularly mediated assemblies of gold nanoparticles with different particle sizes and different linker chain lengths on different substrates have provided new insights into the understanding of the correlation between the interparticle spatial parameters and the optical properties for the one-step-derived thin film assemblies. The experimental-theoretical correlation of the interparticle *d*-spacing has revealed the presence of ordered nanostructures in the thin film assemblies. The linear dependence

of the SP band wavelength of the nanoparticles in the thin film assemblies on the particle size and the interparticle distance has substantiated the control of the interparticle spatial properties in terms of particle size and the molecular linker length. This controllability is further supported by the analyses of the optical properties theoretically using Mie theory and experimentally using reflectometry and spectroscopic ellipsometry, which have provided additional information for the assessment of the optical constants for these nanostructured thin films.

References

1. (a) Daniel, M. C.; Astruc, D. *Chem. Re*V. **2004**, *104*, 293. (b) Rosi, N. L.; Mirkin, C. A. *Chem. Re*V. **2005**, *105*, 1547. (c) Penn, S. G.; He, L.; Natan, M. J. *Curr. Opin. Chem. Biol.* **2003**, *7*, 609. (d) Katz, E.; Willner, I. *Angew. Chem. Int. Ed.* **2004**, *43*, 6042. (e) Haes, A. J.; Stuart, D. A.; Nie, S. M.; Van, Duyne, R. P. *J. Fluoresc.* **2004**, *14*, 355. (f) Nicewarner-Pena, S. R.; Freeman, R. G.; Reiss, B. D.; He, L.; Pena, D. J.; Walton, I. D.; Cromer, R.; Keating, C. D.; Natan, M. J. *Science* **2001**, *294*, 137.

2. (a) Han, L.; Maye, M. M.; Leibowitz, F. L.; Ly, N. K.; Zhong, C. J. *J. Mater. Chem.* **2001**, *11*, 1258. (b) Luo, J.; Jones, V. W.; Han, L.; Maye, M. M.; Kariuki, N.; Zhong, C. J. *J. Phys. Chem.* **2004**, *108*, 9669. (c) Han, L.; Luo, J.; Kariuki, N.; Maye, M. M.; Jones, V. W.; Zhong, C. J. *Chem. Mater.* **2003**, *15*, 29.

3. (a) Maye, M. M.; Zheng, W. X.; Leibowitz, F. L.; Ly, N. K.; Zhong, C. J. *Langmuir* **2000**, *16*, 490. (b) Maye, M. M.; Zhong, C. J. *J. Mater. Chem.* **2000**, *10*, 1895. (c) Schadt, M. J.; Cheung, W.; Luo, J.; Zhong, C. J. *Chem. Mater.* **2006**, *18*, 5147.

4. (a) Leibowitz, F. L.; Zheng, W. X.; Maye, M. M.; Zhong, C. J. *Anal. Chem.* **1999**, *71*, 5076. (b) Kariuki, N. N.; Luo, J.; Hassan, S. A.; Lim, I.-Im S.; Wang, L. Y.; Zhong, C. J. *Chem. Mater.* **2006**, *18*, 123.

5. (a) Keating, C. D.; Musick, M. D.; Lyon, L. A.; Brown, K. R.; Baker, B. E.; Pena, D. J.; Feldheim, D. L.; Mallouk, T. E.; Natan, M. J. *ACS Symp. Ser.* **1997**, *679*, 7. (b) Musick, M. D.; Keating, C. D.; Lyon, L. A.; Botsko, S. L.; Pena, D. J.; Holliway, W. D.; McEvoy, T. M.; Richardson, J. N.; Natan, M. J. *Chem. Mater.* **2000**, *12*, 2869. (c) Mulvaney, S. P.; He, L.; Natan, M. J.; Keating, C. D. *J. Raman Spectrosc.* **2003**, *34*, 163.

6. Andres, R. P.; Bielefeld, J. D.; Henderson, J. I.; Janes, D. B.; Kolagunta, V. R.; Kubiak, C. P.; Mahoney, W. J.; Osifchin, R. G. *Science* **1996**, *273*, 1690.

7. (a) Brust, M.; Bethell, D.; Kiely, C. J.; Schiffrin, D. J. *Langmuir* **1998**, *14*, 5425.(b) Brust, M.; Bethell, D.; Schiffrin, D. J.; Kiely, C. J. *Adv. Mater.* **1995**, *7*, 795. (c) Bethell, D.; Brust, M.; Schiffrin, D. J.; Kiely, C. *J. Electroanal. Chem.* **1996**, *409*, 137. (d) Brust, M.; Kiely, C. J.; Bethell, D.; Schiffrin, D. J. *J. Am. Chem. Soc*. **1998**, *120*, 12367.(e) Baum, T.; Bethell, D.; Brust, M.; Schiffrin, D. J.

Langmuir **1999**, *15*, 866. (f) Horswell, S. L.; O'Neil, I. A.; Schiffrin, D. J. *J. Phys. Chem. B*. **2001**, *105*, 941. (g) Gittins, D. I.; Bethell, D.; Schiffrin, D. J.; Nichols, R. J. *Nature* **2000**, *408*, 67.

8. (a) Zamborini, F. P.; Hicks, J. F.; Murray, R. W. *J. Am. Chem. Soc.* **2000**, *122*, 4514. (b) Templeton, A. C.; Zamborini, F. P.; Wuelfing, W. P.; Murray, R. W. *Langmuir* **2000**, *16*, 6682. (c) Ibanez, F. J.; Gowrishetty, U.; Crain, M. M.; Walsh, K. M.; Zamborini, F. P. *Anal. Chem.* **2006**, *78*, 753. (d) Leopold, M. C.; Donkers, R. L.; Georganopoulou, D.; Fisher, M.; Zamborini, F. P.; Murray, R. W. *Faraday Discuss.* **2004**, *125*, 63.

9. Krasteva, N.; Fogel, Y.; Bauer, R. E.; Muellen, K.; Joseph, Y.; Matsuzawa, N.; Yasuda, A.; Vossmeyer, T. *Ad*V. *Funct. Mater*. **2007**, *17*, 881.

10. (a) Han, L.; Daniel, D. R.; Maye, M. M.; Zhong, C. J. *Anal. Chem.* **2001**, *73*, 4441. (b) Wang, L. Y.; Kariuki, N. N.; Schadt, M.; Mott, D.; Luo, J.; Zhong, C. J.; Shi, X. J.; Zhang, C.; Hao, W. B.; Lu, S.; Kim, N.; Wang, J.-Q. *Sensors* **2006**, *6*, 667. (c) Wang, L. Y.; Shi, X.; Kariuki, N. N.; Schadt, M.; Wang, G. R.; Rendeng, Q.; Choi, J.; Luo, J.; Lu, S.; Zhong, C. J. *J. Am. Chem. Soc.* **2007**, *129*, 2161.

11. Hostetler, M. J.; Templeton, A. C.; Murray, R. W. *Langmuir* **1999**, *15*, 3782.

12. Abeles, B.; Cheng, P.; Coutts, M. D.; Arie, Y. *Ad*V. *Phys.* **1975**, *24*, 407.

13. (a) Mie, G. *Ann. Phys.* **1908**, *25*, 377. (b) Link, S.; El-Sayed, M. A. *Int. Rev. Phys. Chem.* **2000**, *19*, 409. (c) Wang, H.; Brandl, D. W.; Nordlander, P.; Halas, N. J. *Acc. Chem. Res.* **2007**, *40*, 53.

14. Kelly, K. L.; Coronado, E.; Zhao, L. L.; Schatz, G. C. *J. Phys. Chem. B* **2003**, *107*, 668.

15. (a) Mirkin, C. A.; Letsinger, R. L.; Mucic, R. C.; Storhoff, J. J. *Nature* **1996**, *382*, 607. (b) Elghanian, R.; Storhoff, J. J.; Mucic, R. C.; Letsinger, R. L.; Mirkin, C. A. *Science* **1997**, *277*, 1078. (c) Rosi, N. L.; Giljohann, D. A.; Thaxton, C. S.; Lytton-Jean, A. K. R.; Han, M. S.; Mirkin, C. *Science* **2006**, *312*, 1027. (d) Stoeva, S. I.; Lee, J. S.; Thaxton, C. S.; Mirkin, C. A. *Angew. Chem. Int. Ed.* **2006**, *45*, 3303.

16. (a) Dillenback, L. M.; Goodrich, G. P.; Keating, C. D. *Nano Lett.* **2006**, *6*, 16. (b) He, L.; Smith, E. A.; Natan, M. J.; Keating, C. D. *J. Phys. Chem. B* **2004**, *108*, 10973.

17. Wang, G. R.; Wang, L. Y.; Rendeng, Q.; Wang, J.; Luo, J.; Zhong, C. J. *J. Mater. Chem.* **2007**, *17*, 457.

18. Papavassiliou, G. C. *Prog. Solid State Chem.* **1979**, *12*, 185.

19. Kim, S. H.; Ock, K. S.; Im, J. H.; Kim, J. H.; Koh, K. N.; Kang, S. W. *Dyes Pigments* **2000**, *46*, 55.

20. Alejandro-Arellano, M.; Ung, T.; Blanco, A .; Mulvaney, P.; Liz-Marzan L. M. *Pure Appl. Chem.* **2000**,*72*, 257.

21. Jensen, T.; Kelly, L.; Lazarides, A.; Schatz, G. C. *J. Cluster Sci.* **1999**, *10*, 295.

22. Yang, K.; Fan, H. Y.; Malloy, K. J.; Brinker, C. J.; Sigmon, T. W. *Thin Solid Films* **2005**, *491*, 38.

23. Kooij, E. S.; Wormeester, H.; Brouwer, E. A. M.; van Vroonhoven, E.; van Silfhout, A.; Poelsema, B. *Langmuir* **2002**, *18*, 4401.

24. Palik, E. D. *Handbook of Optical Constants of Solids*; Academic Press: New York, 1985; p 294.

Appendix A: Data for ZnO thin films analyzed in this study

A1: ZnO on Silicon

GM30a

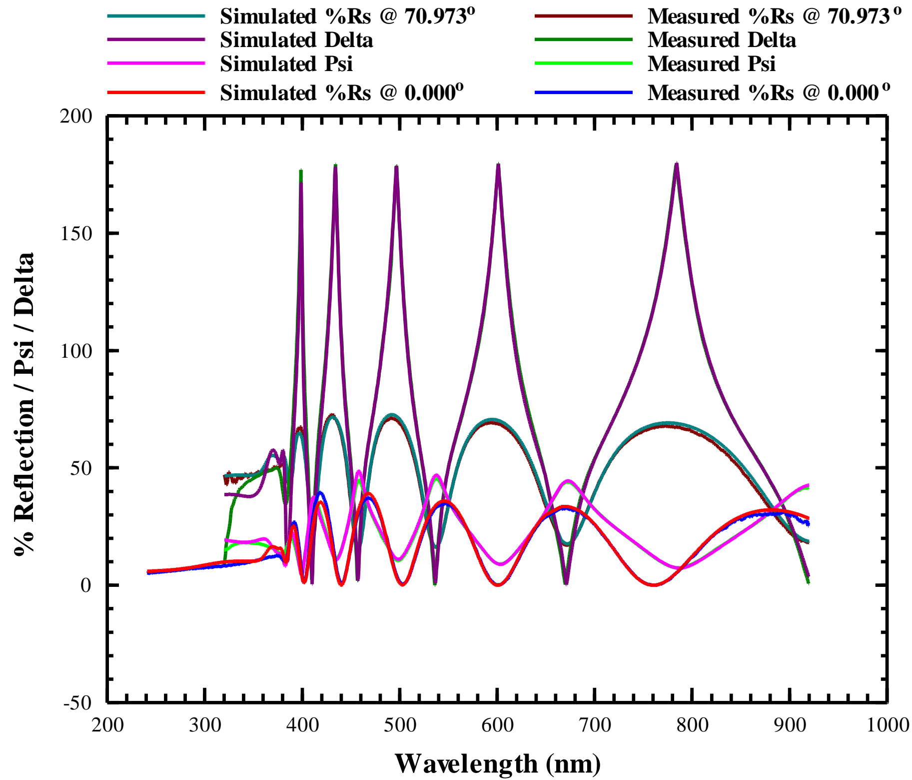

Obtained Data	
Thickness Layer 1	671.46 nm
Thickness Layer 2	16.94 nm
Index @ 632 nm	1.98328
Extinction coefficient @ 632 nm	0.0000
RMSE	1.277

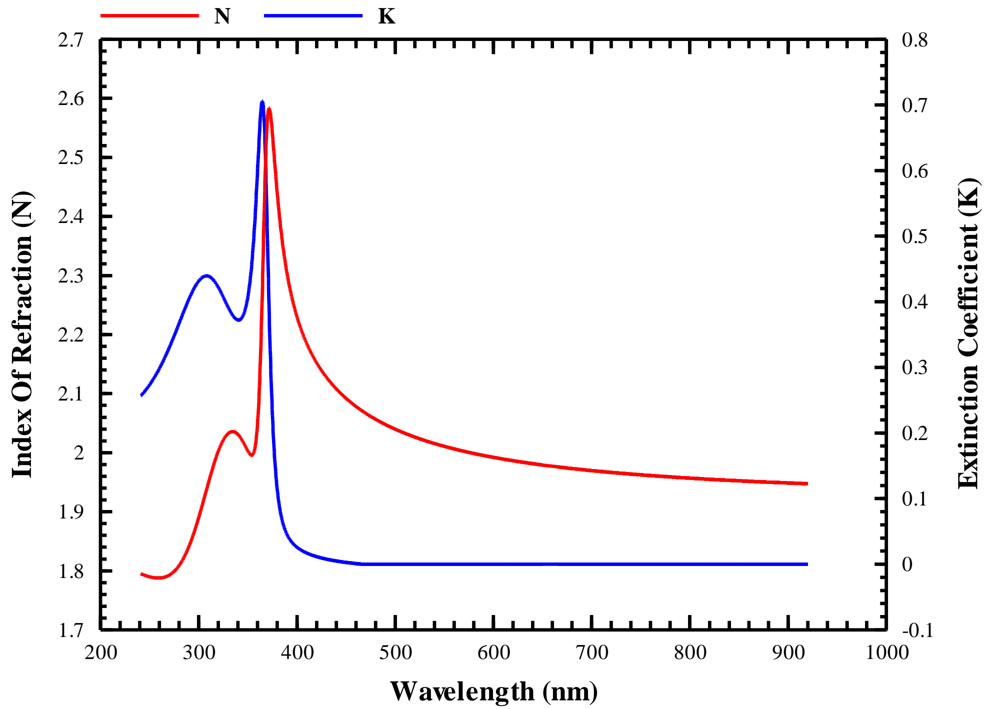

Layer #1 Material Coefficient Table	Layer #2 Material Coefficient Table
Number of Oscillators = 3	EMA Screening = 0.3333
HF Diel. Const. = 1.000000	EMA Type = Bruggeman
Damping Coef. = 0.954095	Number Materials = 2
Amplitude(1) = 16.362087	% Same As Layer #1 = 50.0000
C. Energy(1) = 10.951798	% VOID = 50.0000
Vib. Freq.(1) = 19.150711	
Amplitude(2) = 1.085015	
C. Energy(2) = 3.370704	
Vib. Freq.(2) = 0.135818	
Amplitude(3) = 2.313886	
C. Energy(3) = 3.873573	
Vib. Freq.(3) = 1.109269	

GM13-g

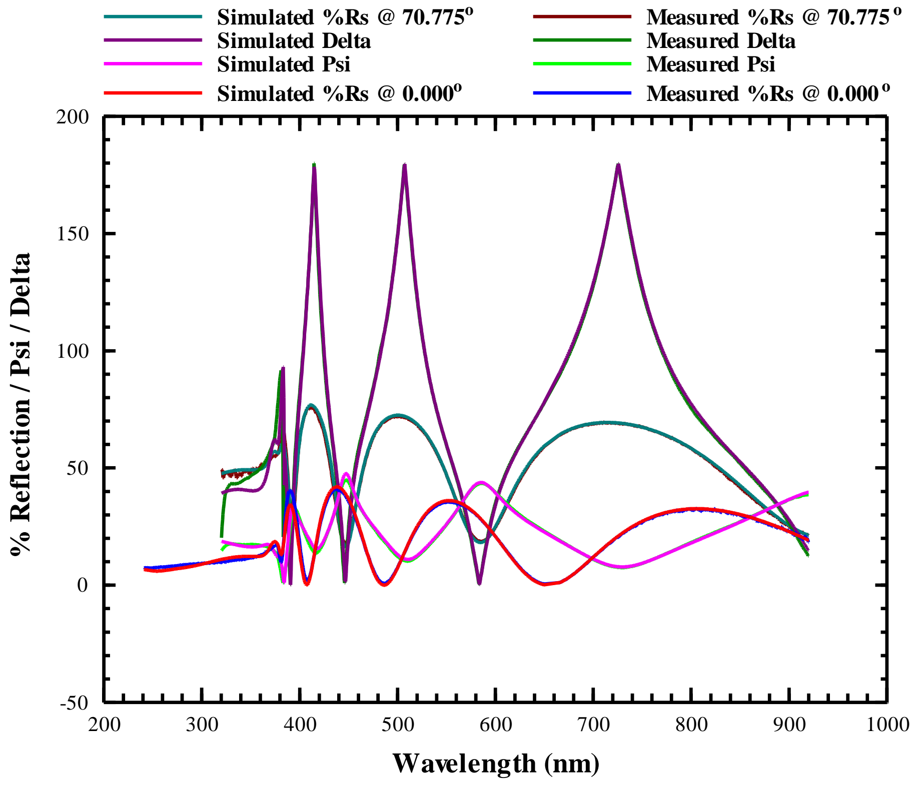

Data Obtained	
Thickness Layer 1	402.28 nm
Thickness Layer 2	12.93 nm
Index @ 632 nm	2.01218
Extinction coefficient @ 632 nm	0.0000
RMSE	0.974

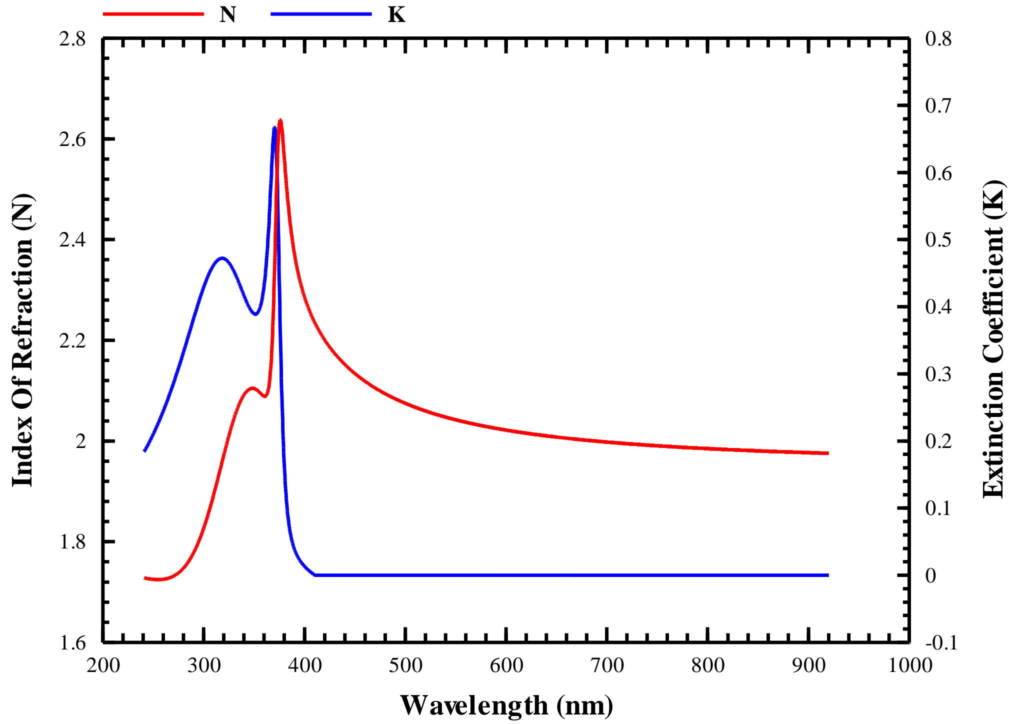

Layer #1 Material Coefficient Table	Layer #2 Material Coefficient Table
Number of Oscillators = 2	EMA Screening = 0.3333
HF Diel. Const. = 3.262404	EMA Type = Bruggeman
Damping Coef. = 2.469199	Number Materials = 2
Amplitude(1) = 0.505850	% Same As Layer #1 = 50.0000
C. Energy(1) = 3.323064	% VOID = 50.0000
Vib. Freq.(1) = 0.106183	
Amplitude(2) = 1.416225	
C. Energy(2) = 3.726166	
Vib. Freq.(2) = 1.097415	

GM29_3

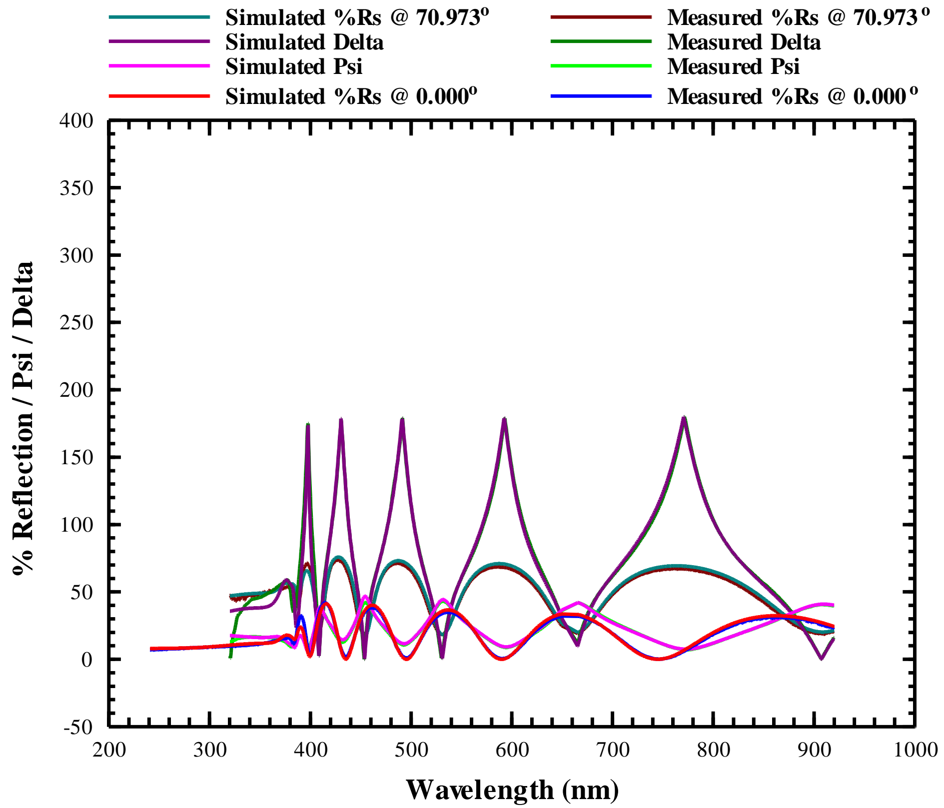

Data Obtained	
Thickness Layer 1	646.95 nm
Thickness Layer 2	12.47 nm
Index @ 632 nm	2.02177
Extinction coefficient @ 632 nm	0.0000
RMSE	1.449

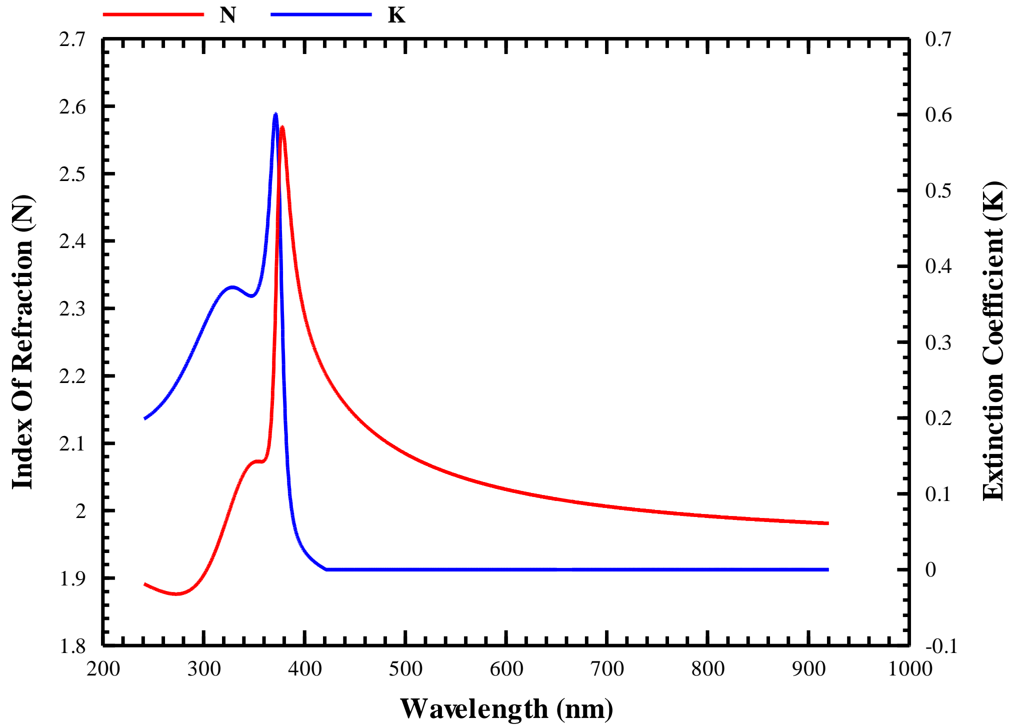

Layer #1 Material Coefficient Table	Layer #2 Material Coefficient Table
Number of Oscillators = 3	EMA Screening = 0.3333
HF Diel. Const. = 1.000000	EMA Type = Bruggeman
Damping Coef. = 1.057440	Number Materials = 2
Amplitude(1) = 16.563117	% Same As Layer #1 = 50.0000
C. Energy(1) = 10.702755	% VOID = 50.0000
Vib. Freq.(1) = 20.340449	
Amplitude(2) = 0.916047	
C. Energy(2) = 3.309807	
Vib. Freq.(2) = 0.125150	
Amplitude(3) = 2.116560	
C. Energy(3) = 3.649127	
Vib. Freq.(3) = 1.111367	

GM17’a

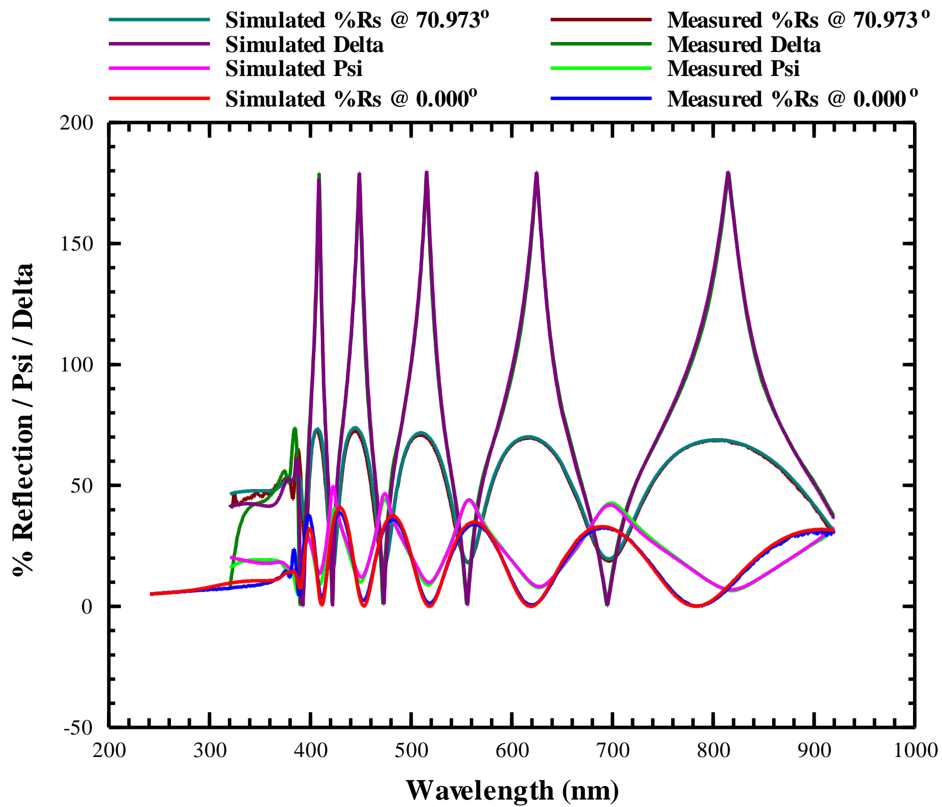

Obtained Data	
Thickness Layer 1	675.18 nm
Thickness Layer 2	20.57 nm
Index @ 632 nm	2.03348
Extinction coefficient @ 632 nm	0.0000
RMSE	1.590

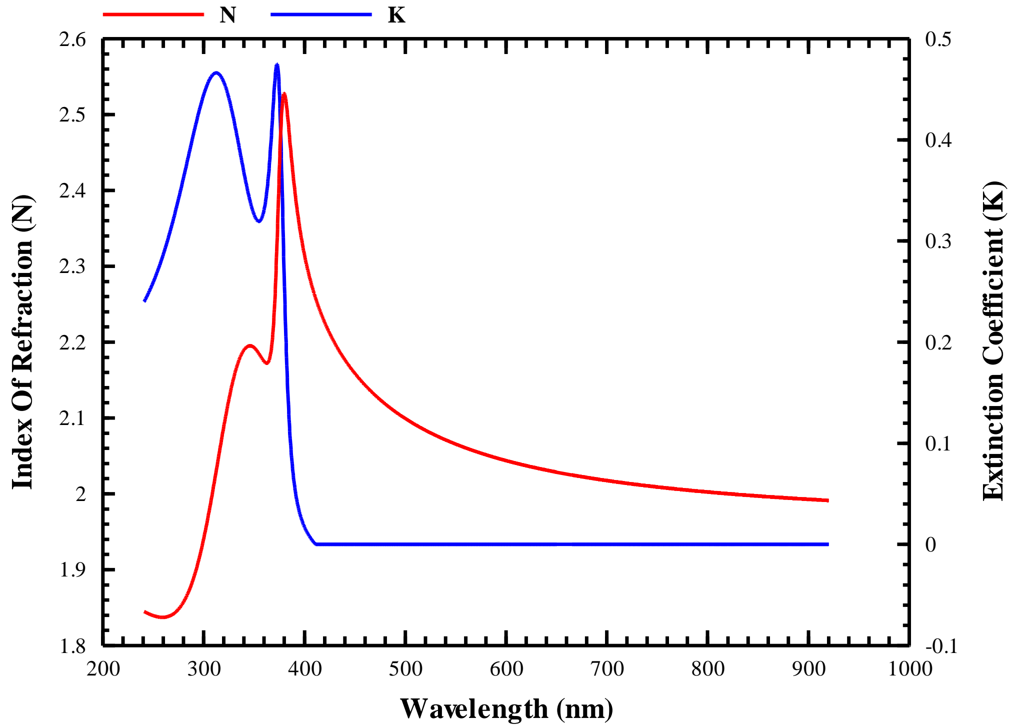

Layer #1 Material Coefficient Table	Layer #2 Material Coefficient Table
Number of Oscillators = 2	EMA Screening = 0.3333
HF Diel. Const. = 1.000000	EMA Type = Bruggeman
Damping Coef. = 1.049688	Number Materials = 2
Amplitude(1) = 17.492652	% Same As Layer #1 = 50.0000
C. Energy(1) = 11.452615	% VOID = 50.0000
Vib. Freq.(1) = 22.392184	
Amplitude(2) = 0.853285	
C. Energy(2) = 3.297137	
Vib. Freq.(2) = 0.136982	

GM25_2

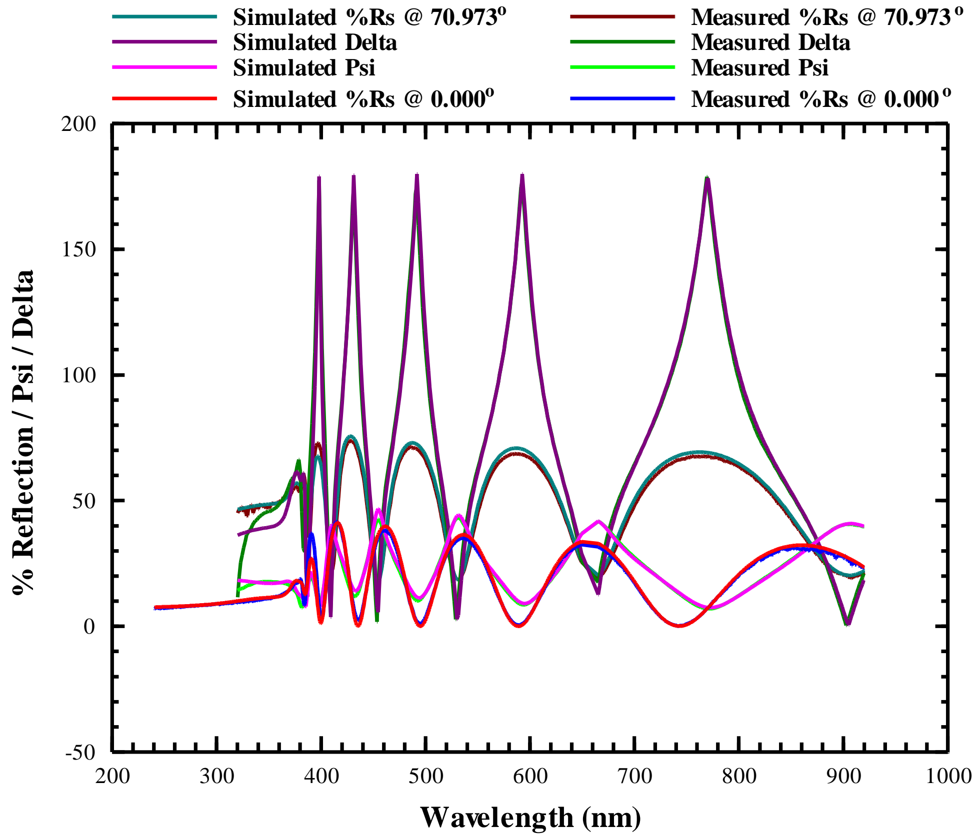

Data Obtained	
Thickness Layer 1	643.34 nm
Thickness Layer 2	14.61 nm
Index @ 632 nm	2.03629
Extinction coefficient @ 632 nm	0.0000
RMSE	1.473

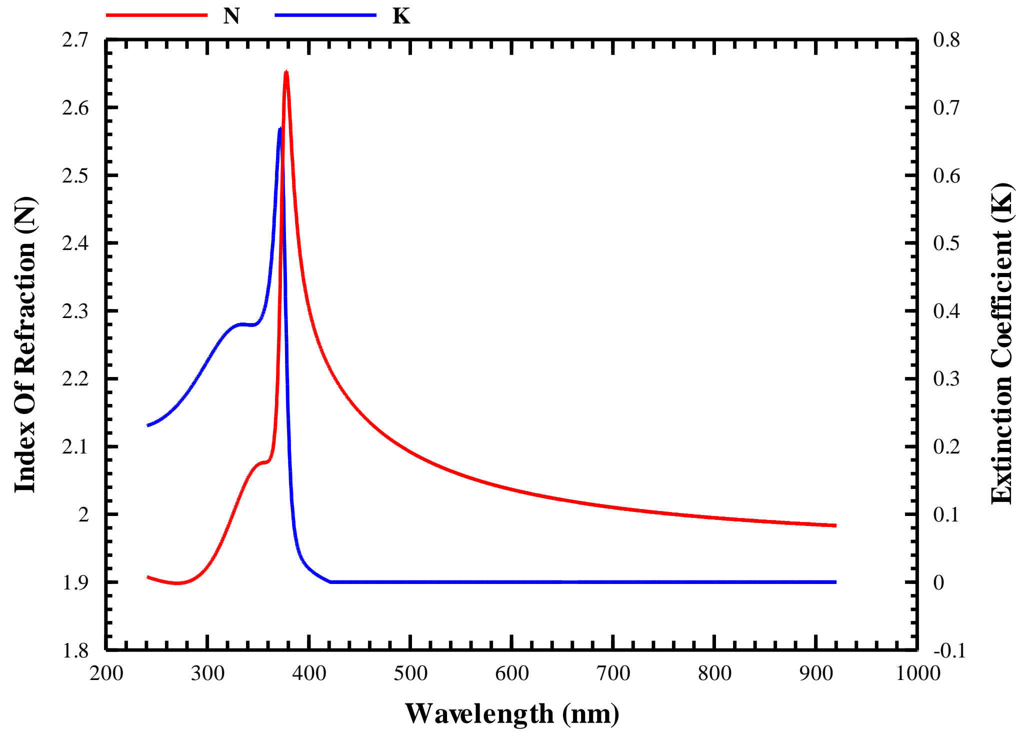

Layer #1 Material Coefficient Table	Layer #2 Material Coefficient Table
Number of Oscillators = 2	
HF Diel. Const. = 1.000000	EMA Screening = 0.3333
Damping Coef. = 1.045453	EMA Type = Bruggeman
Amplitude(1) = 14.727527	Number Materials = 2
C. Energy(1) = 9.477580	% Same As Layer #1 = 50.0000
Vib. Freq.(1) = 18.706533	% VOID = 50.0000
Amplitude(2) = 0.904183	
C. Energy(2) = 3.304946	
Vib. Freq.(2) = 0.109156	

A2: ZnO on Platinum

GM30a_100C

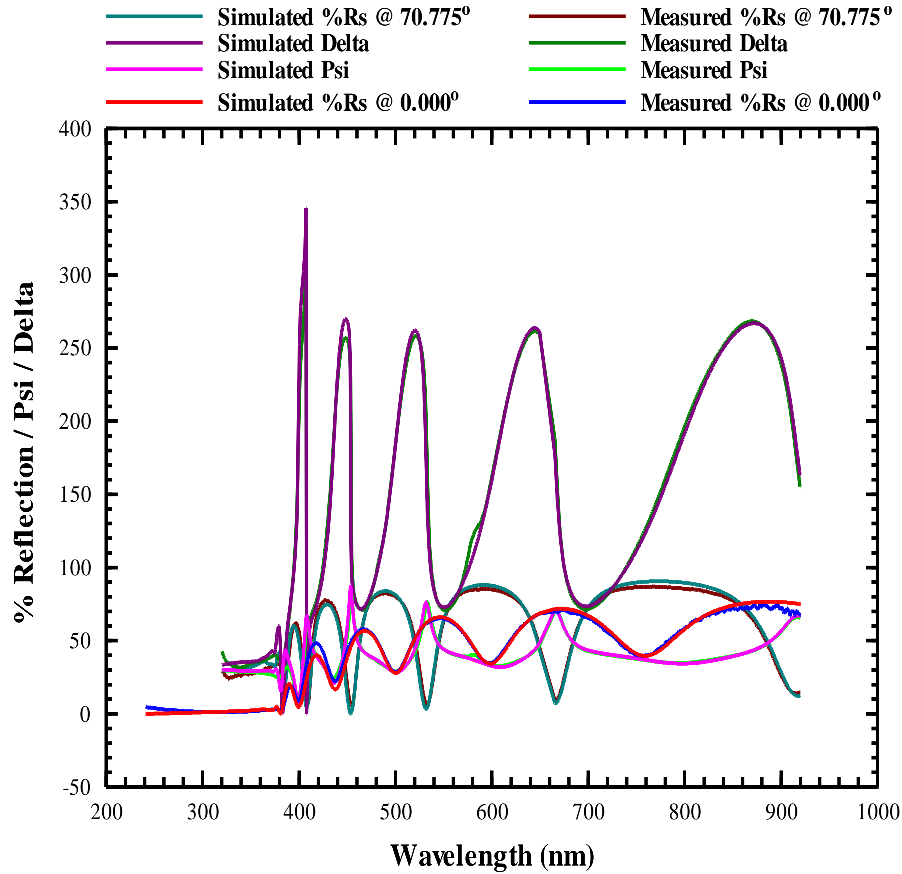

Data Obtained
Thickness Layer 1 = 653.46 nm
Thickness Layer 2 = 61.69 nm
Index @ 632 nm = 1.92540
Extinction coefficient @ 632 nm =0.0028
RMSE = 2.828

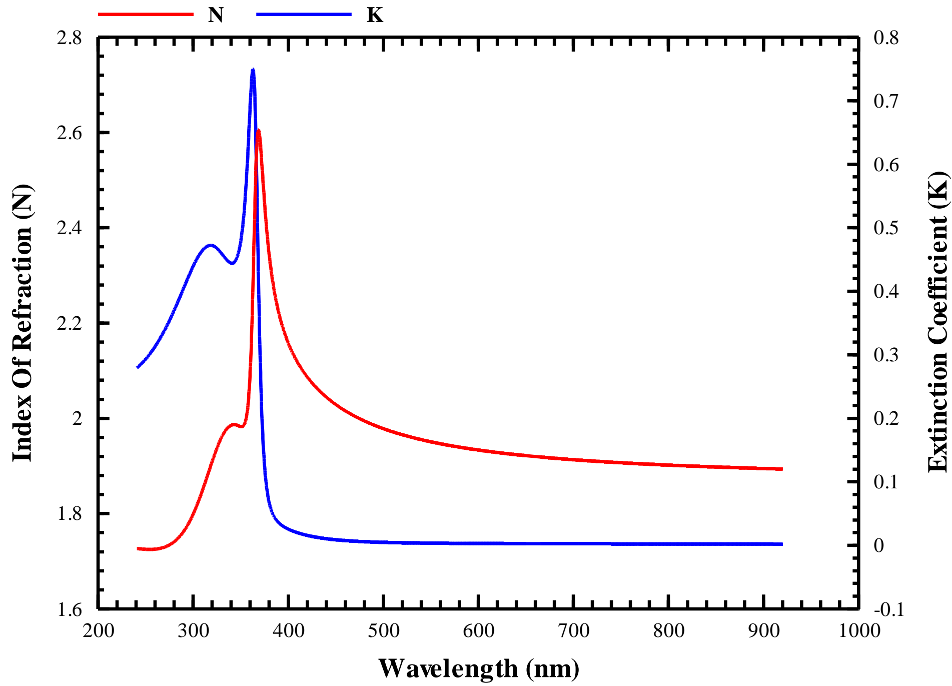

Layer #1 Material Coefficient Table	Layer #2 Material Coefficient Table
Number of Oscillators = 3	EMA Screening = 0.3333
HF Diel. Const. = 1.000000	EMA Type = Landau-Lifshitz
Damping Coef. = 0.889855	Number Nodes = 3
Amplitude(1) = 14.372933	HOST MATERIAL = Same As Layer #1
C. Energy(1) = 9.909784	Material #2
Vib. Freq.(1) = 21.899235	% POSITION NODE #1 = 0.00
Amplitude(2) = 0.987505	% POSITION NODE #2 = 50.00
C. Energy(2) = 3.386970	% POSITION NODE #3 = 100.00
Vib. Freq.(2) = 0.114473	% FRACTION VOID NODE #1 = 0.0000
Amplitude(3) = 2.096450	% FRACTION VOID NODE #2 = 66.4196
C. Energy(3) = 3.739206	% FRACTION VOID NODE #3 = 67.0000
Vib. Freq.(3) = 1.024441	

GM11b_400

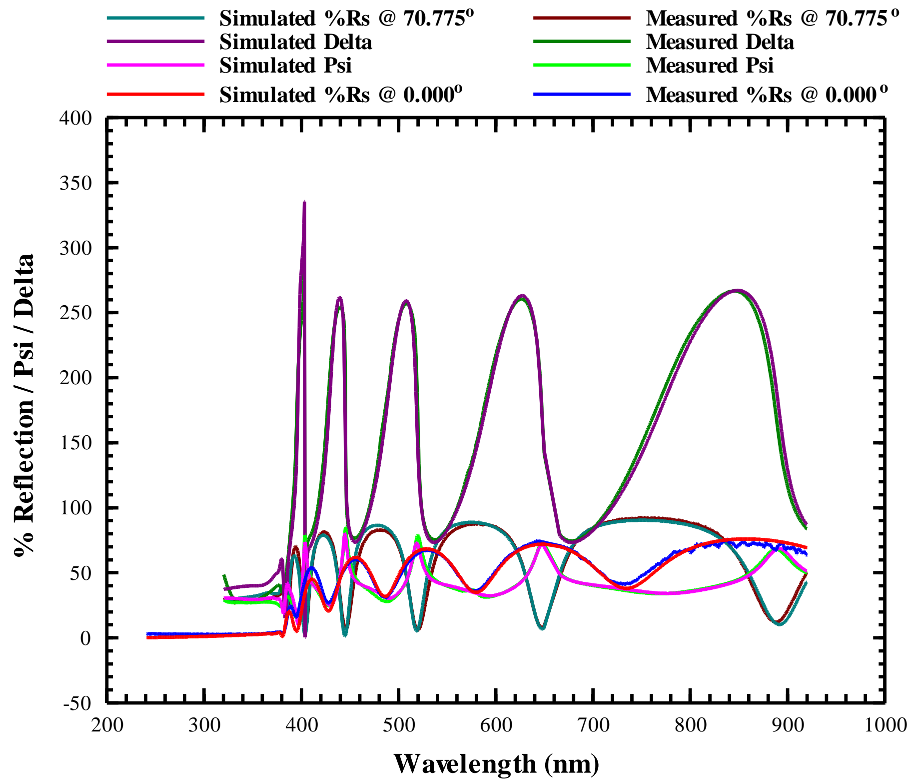

Data Obtained
Thickness Layer 1 = 623.67 nm
Thickness Layer 2 = 62.66 nm
Index @ 632 nm = 1.95369
Extinction coefficient @ 632 nm =0.0021
RMSE = 3.463

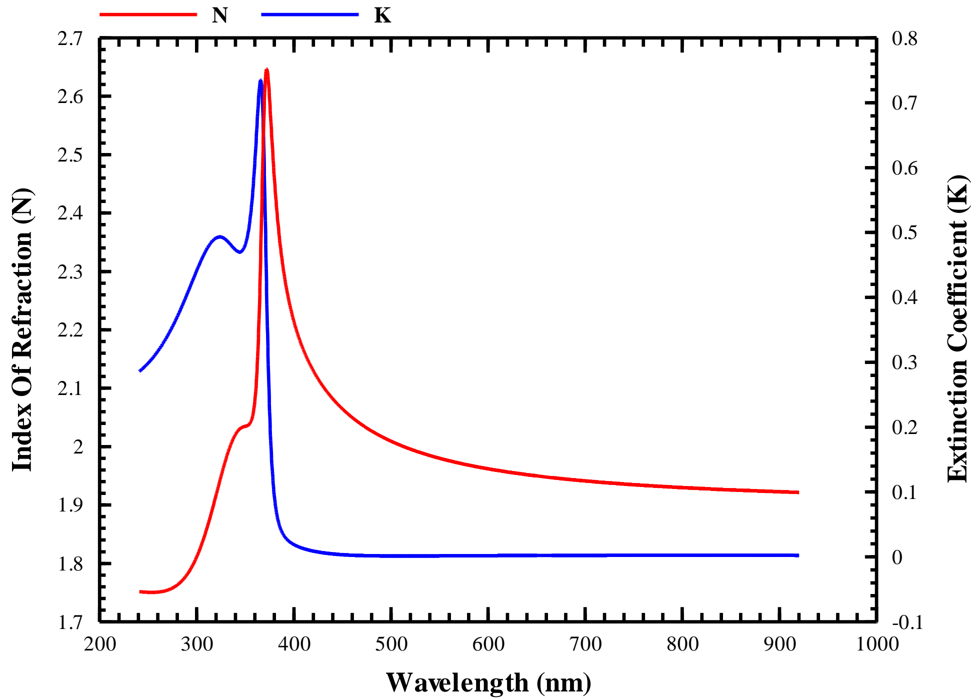

Layer #1 Material Coefficient Table	Layer #2 Material Coefficient Table
Number of Oscillators = 3	EMA Screening = 0.3333
HF Diel. Const. = 1.000000	EMA Type = Landau-Lifshitz
Damping Coef. = 0.887599	Number Nodes = 3
Amplitude(1) = 14.205568	HOST MATERIAL = Same As Layer #1
C. Energy(1) = 9.546816	Material #2 = VOID
Vib. Freq.(1) = 22.725153	% POSITION NODE #1 = 0.00
Amplitude(2) = 0.988639	% POSITION NODE #2 = 50.00
C. Energy(2) = 3.356816	% POSITION NODE #3 = 100.00
Vib. Freq.(2) = 0.119618	% FRACTION VOID NODE #1 = 0.0000
Amplitude(3) = 2.045019	% FRACTION VOID NODE #2 = 80.0660
C. Energy(3) = 3.676850	% FRACTION VOID NODE #3 = 67.0000
Vib. Freq.(3) = 0.972141	EMA Screening = 0.3333

GM17a_550

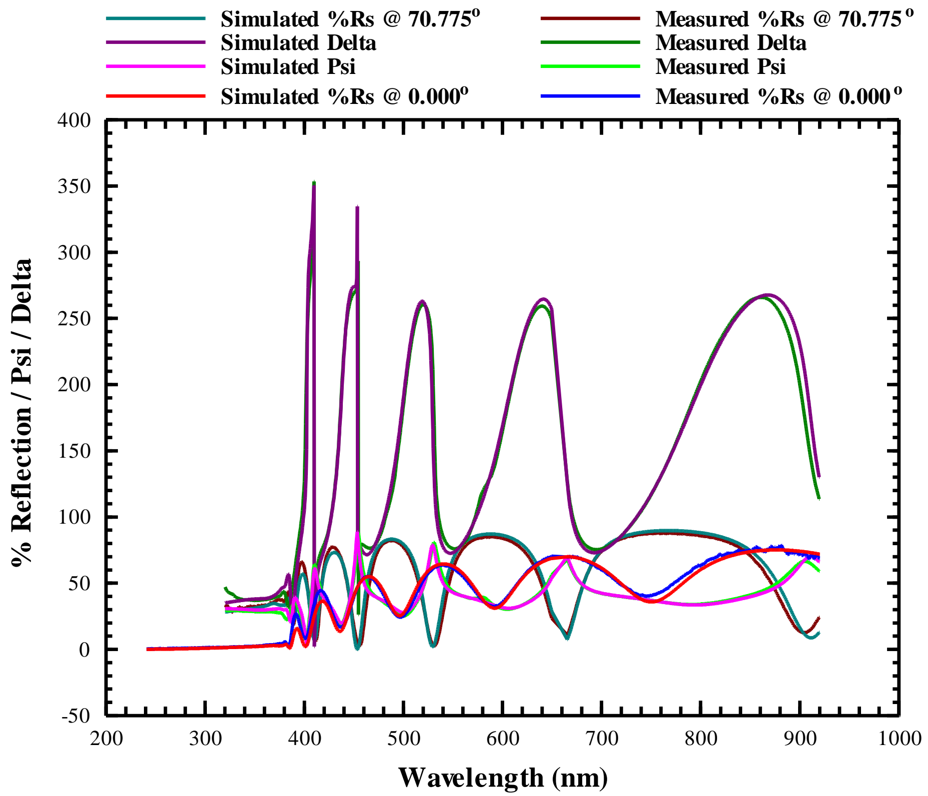

Data Obtained
Thickness Layer 1 = 636.24 nm
Thickness Layer 2 = 63.21 nm
Index @ 632 nm = 1.95735
Extinction coefficient @ 632 nm =0.0044
RMSE = 3.726

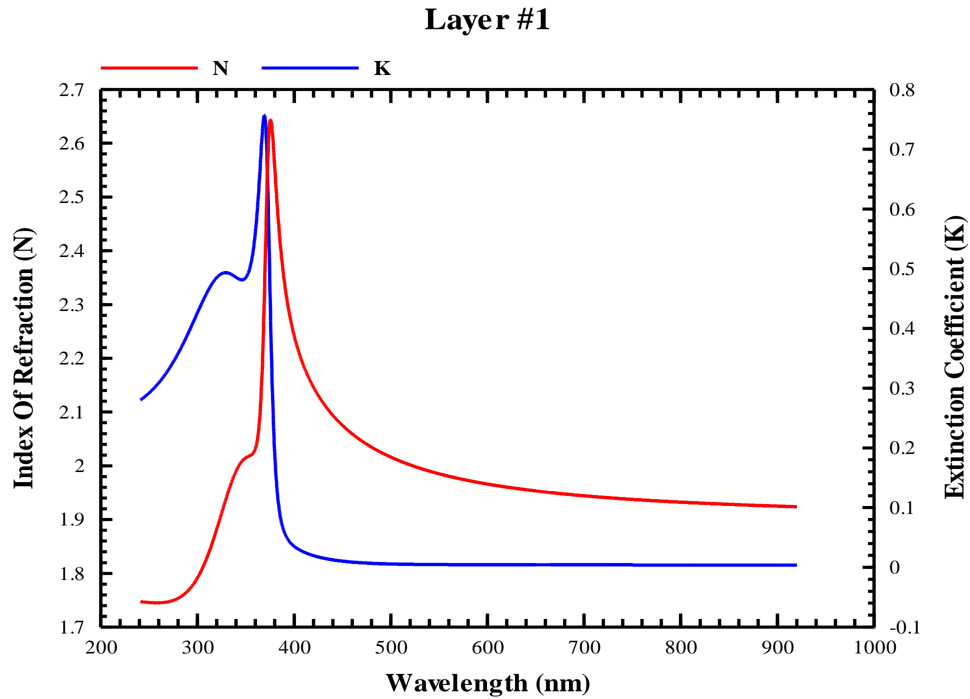

Layer #1 Material Coefficient Table	Layer #2 Material Coefficient Table
Number of Oscillators = 3	EMA Screening = 0.3333
HF Diel. Const. = 1.000000	EMA Type = Landau-Lifshitz
Damping Coef. = 0.880208	Number Nodes = 3
Amplitude(1) = 14.400938	HOST MATERIAL = Same As Layer #1
C. Energy(1) = 9.690060	Material #2 = VOID
Vib. Freq.(1) = 22.909271	% POSITION NODE #1 = 0.00
Amplitude(2) = 0.989562	% POSITION NODE #2 = 50.00
C. Energy(2) = 3.325974	% POSITION NODE #3 = 100.00
Vib. Freq.(2) = 0.118612	% FRACTION VOID NODE #1 = 0.0000
Amplitude(3) = 2.051128	% FRACTION VOID NODE #2 = 75.5817
C. Energy(3) = 3.630214	% FRACTION VOID NODE #3 = 66.3206
Vib. Freq.(3) = 0.989979	EMA Screening = 0.3333

GM19c_650

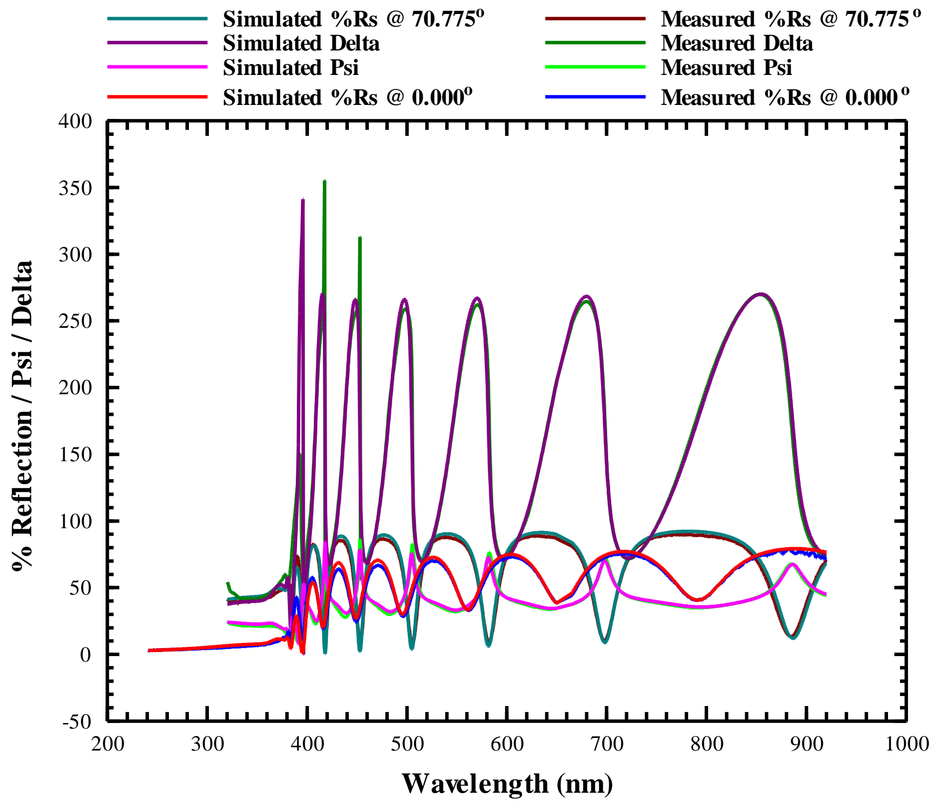

Data Obtained
Thickness Layer 1 = 875.80 nm
Thickness Layer 2 = 35.31 nm
Index @ 632 nm = 1.97995
Extinction coefficient @ 632 nm =0.0000
RMSE = 4.063

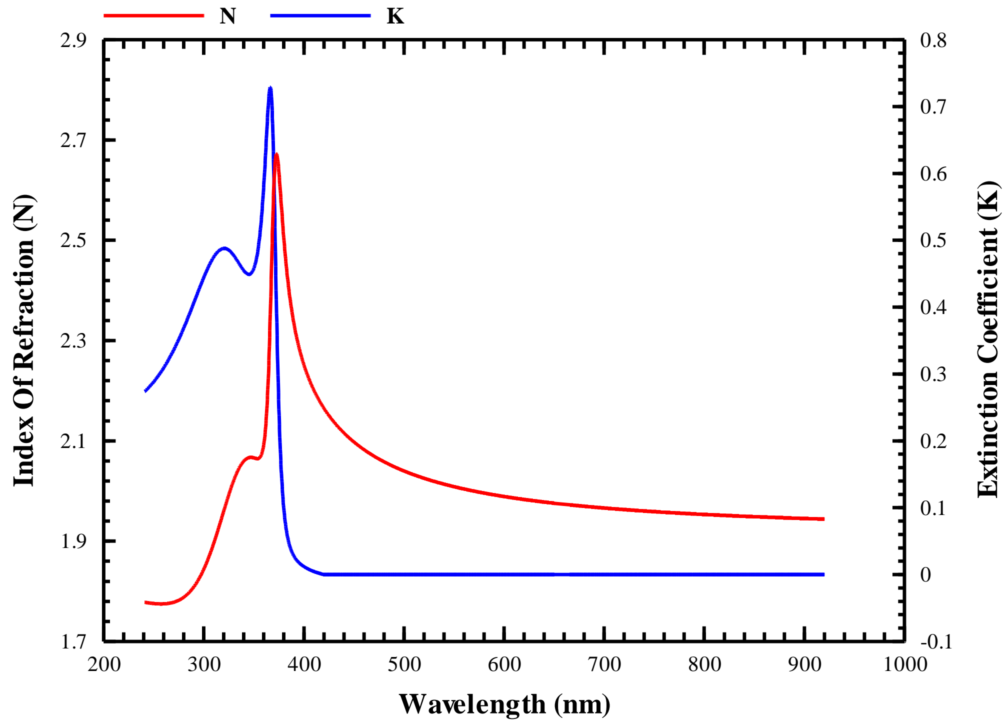

Layer #1 Material Coefficient Table	Layer #2 Material Coefficient Table
Number of Oscillators = 3	EMA Screening = 0.3333
HF Diel. Const. = 1.000000	EMA Type = Landau-Lifshitz
Damping Coef. = 0.928057	Number Nodes = 3
Amplitude(1) = 15.362420	HOST MATERIAL = Same As Layer #1
C. Energy(1) = 10.247146	Material #2 = VOID
Vib. Freq.(1) = 23.515086	% POSITION NODE #1 = 0.00
Amplitude(2) = 1.005339	% POSITION NODE #2 = 50.00
C. Energy(2) = 3.352816	% POSITION NODE #3 = 100.00
Vib. Freq.(2) = 0.119669	% FRACTION VOID NODE #1 = 0.0000
Amplitude(3) = 2.176737	% FRACTION VOID NODE #2 = 59.0790
C. Energy(3) = 3.706540	% FRACTION VOID NODE #3 = 57.7415
Vib. Freq.(3) = 1.004253	EMA Screening = 0.3333

GM20r_700

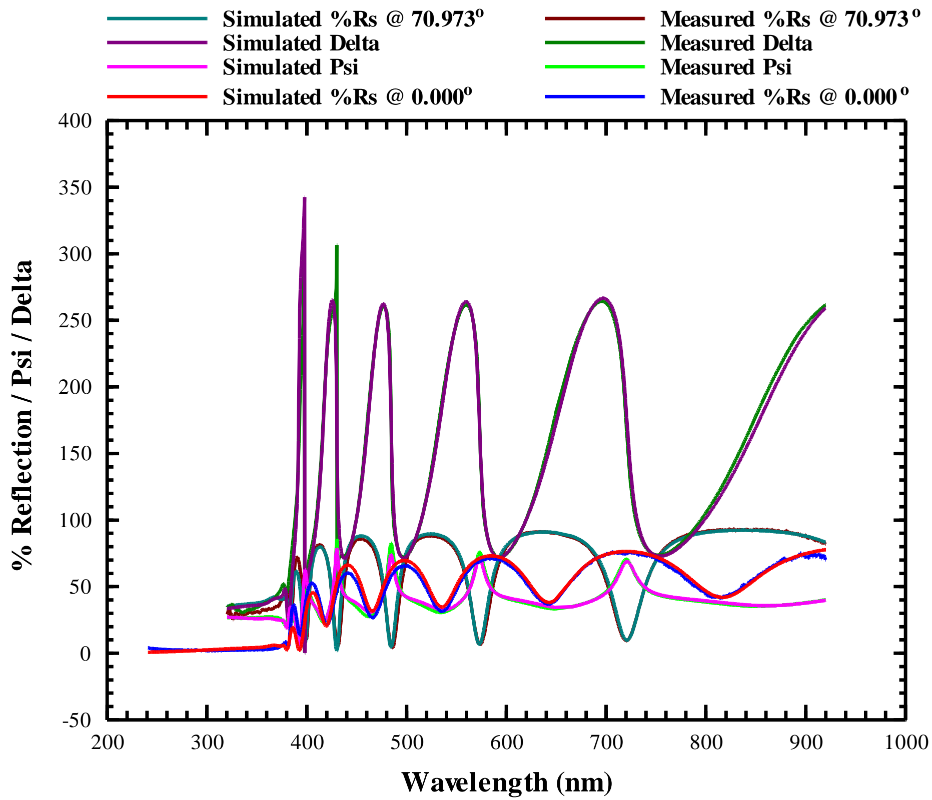

Data Obtained
Thickness Layer 1 = 685.61 nm
Thickness Layer 2 = 49.44 nm
Index @ 632 nm = 1.99080
Extinction coefficient @ 632 nm =0.0000
RMSE = 3.908

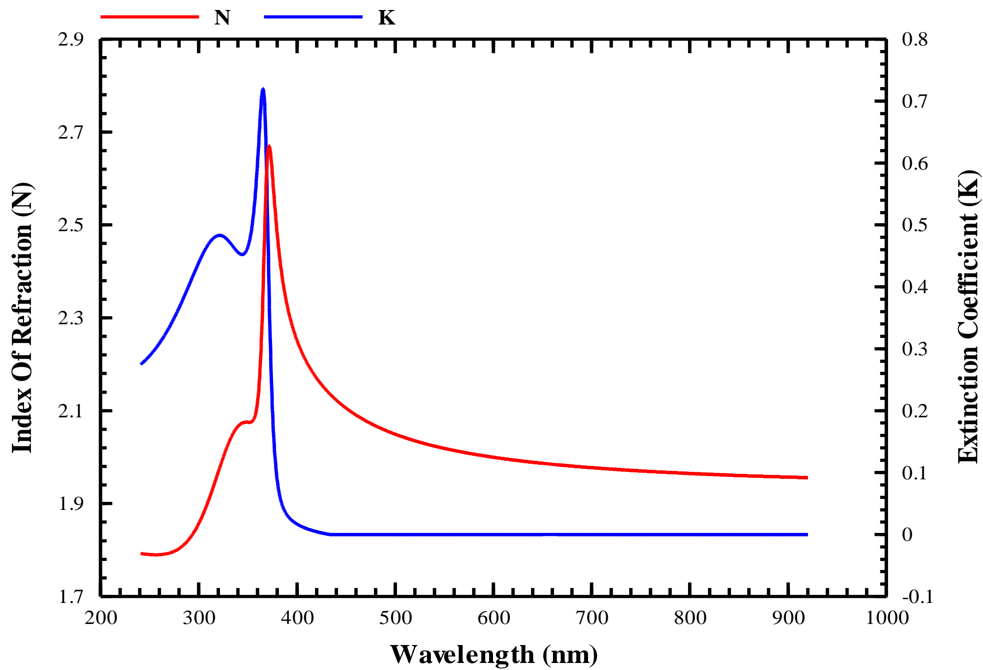

GM20r

Layer #1 Material Coefficient Table	Layer #2 Material Coefficient Table
Number of Oscillators = 3	EMA Screening = 0.3333
HF Diel. Const. = 1.000000	EMA Type = Landau-Lifshitz
Damping Coef. = 0.922374	Number Nodes = 3
Amplitude(1) = 15.472256	HOST MATERIAL = Same As Layer #1
C. Energy(1) = 10.196619	Material #2 = VOID
Vib. Freq.(1) = 23.706470	% POSITION NODE #1 = 0.00
Amplitude(2) = 0.988901	% POSITION NODE #2 = 50.00
C. Energy(2) = 3.361981	% POSITION NODE #3 = 100.00
Vib. Freq.(2) = 0.118994	% FRACTION VOID NODE #1 = 0.0000
Amplitude(3) = 2.161070	% FRACTION VOID NODE #2 = 57.5258
C. Energy(3) = 3.699844	% FRACTION VOID NODE #3 = 57.1457
Vib. Freq.(3) = 1.011007	

Appendix B: Data for $SrTiO_3$ (STO) thin films analyzed in this study

B1: STO on Silicon

DK15_1

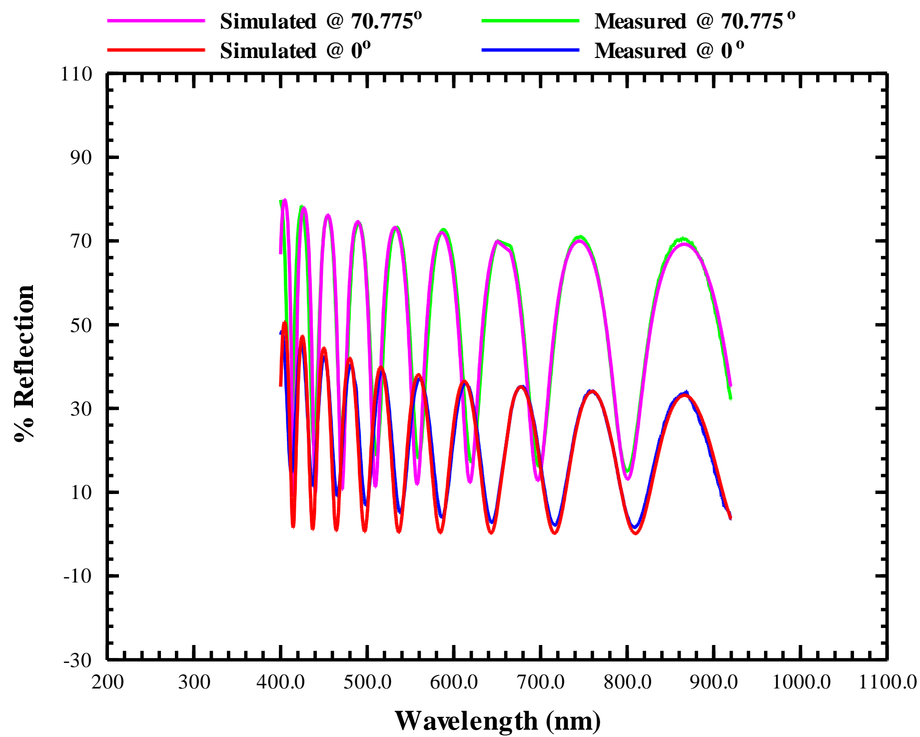

Data Obtained	
Thickness	1650.42 nm
Index @ 632 nm (max)	1.84401
Extinction coefficient @ 632 nm	0.0000
RMSE	4.962

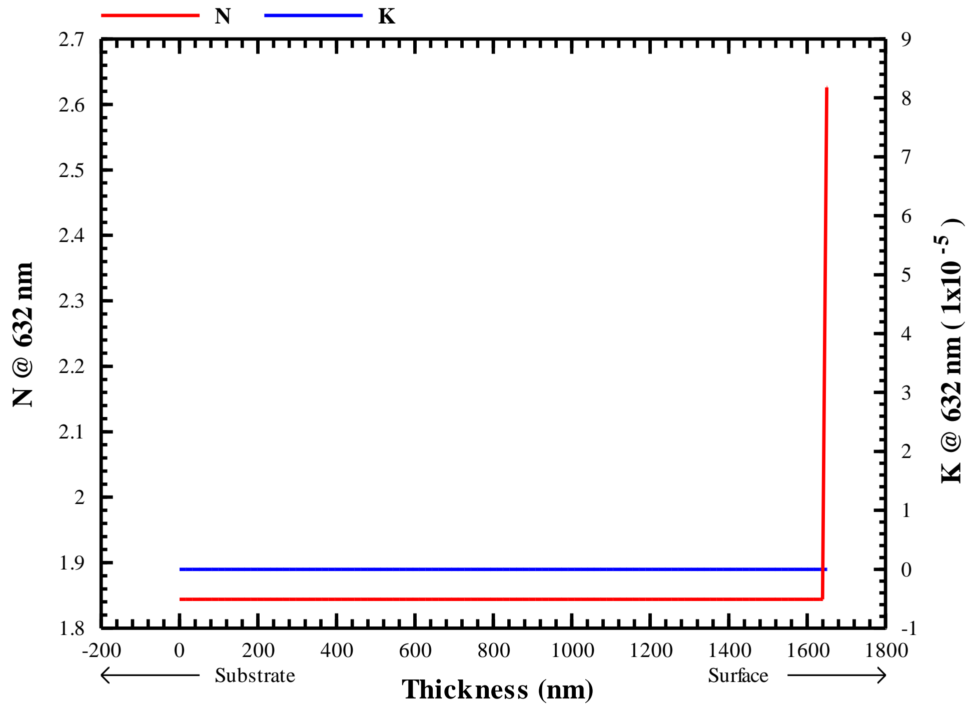

Layer #1 Material Coefficient Table	
EMA Screening	0.3333
EMA Type	Landau-Lifshitz
Number Nodes	3
HOST MATERIAL	Same As Layer #2
Material #2	Same As Layer #3
% POSITION NODE #1	0.00
% POSITION NODE #2	99.13
% POSITION NODE #3	100.00
% FRACTION Same As Layer #3 NODE #1	0.0000
% FRACTION Same As Layer #3 NODE #2	0.0000
% FRACTION Same As Layer #3 NODE #3	100.0000

DK17_2

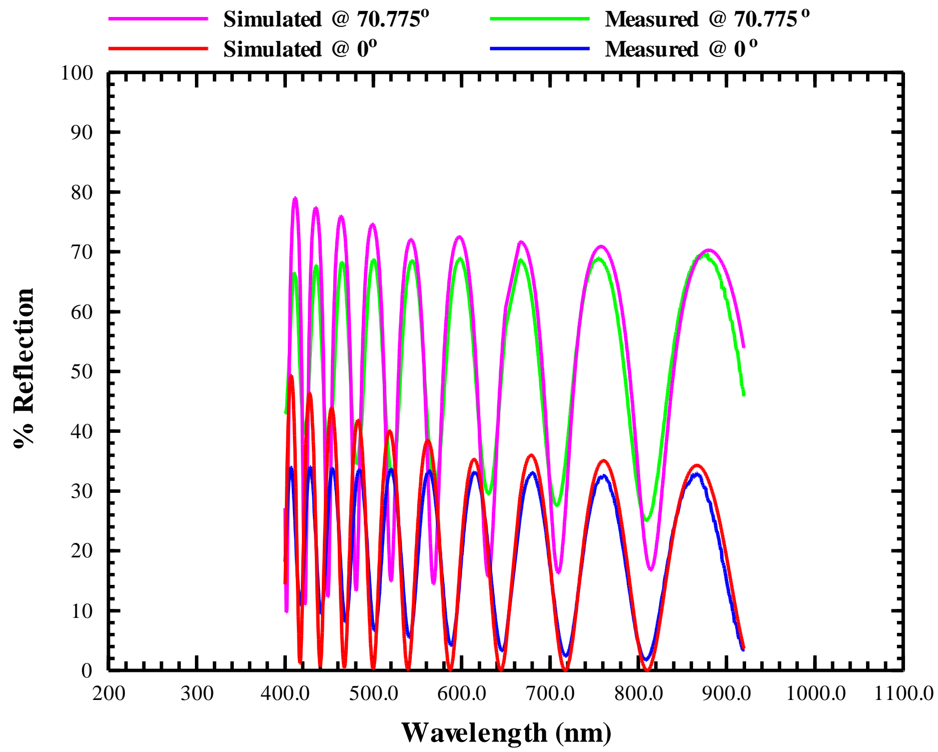

Data Obtained	
Thickness	1579.94 nm
Index @ 632 nm (max)	1.98940
Extinction coefficient @ 632 nm	0.0000
RMSE	6.415

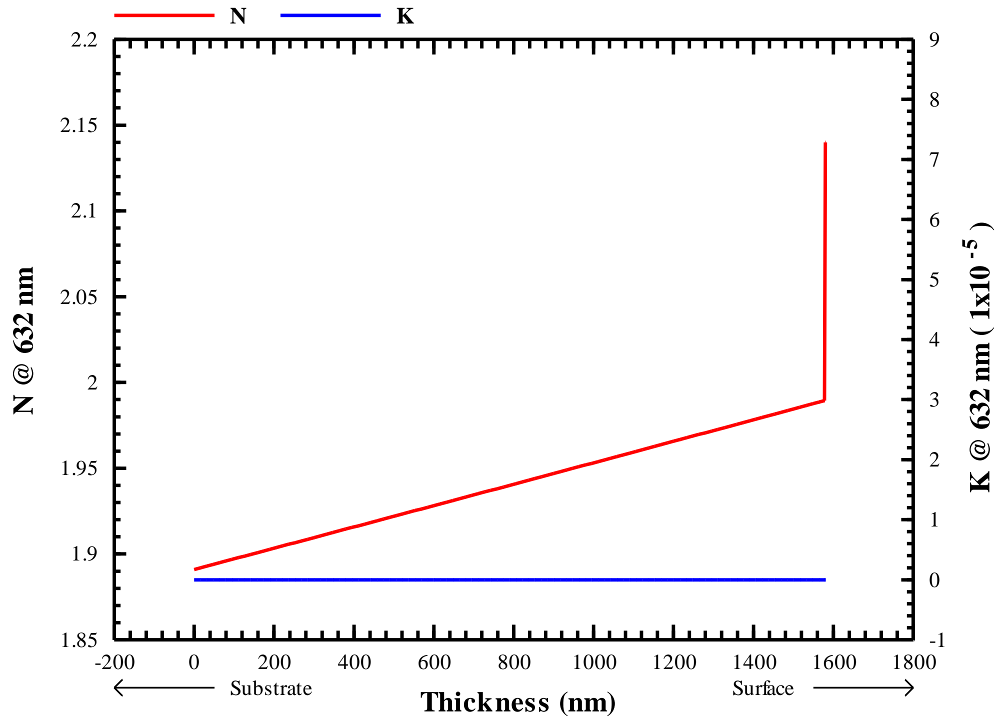

Layer #1 Material Coefficient Table	
EMA Screening	0.3333
EMA Type	Landau-Lifshitz
Number Nodes	3
HOST MATERIAL	Same As Layer #2
Material #2	Same As Layer #3
% POSITION NODE #1	0.00
% POSITION NODE #2	78.38
% POSITION NODE #3	100.00
% FRACTION Same As Layer #3 NODE #1	0.0000
% FRACTION Same As Layer #3 NODE #2	40.0223
% FRACTION Same As Layer #3 NODE #3	100.0000

DK19_1

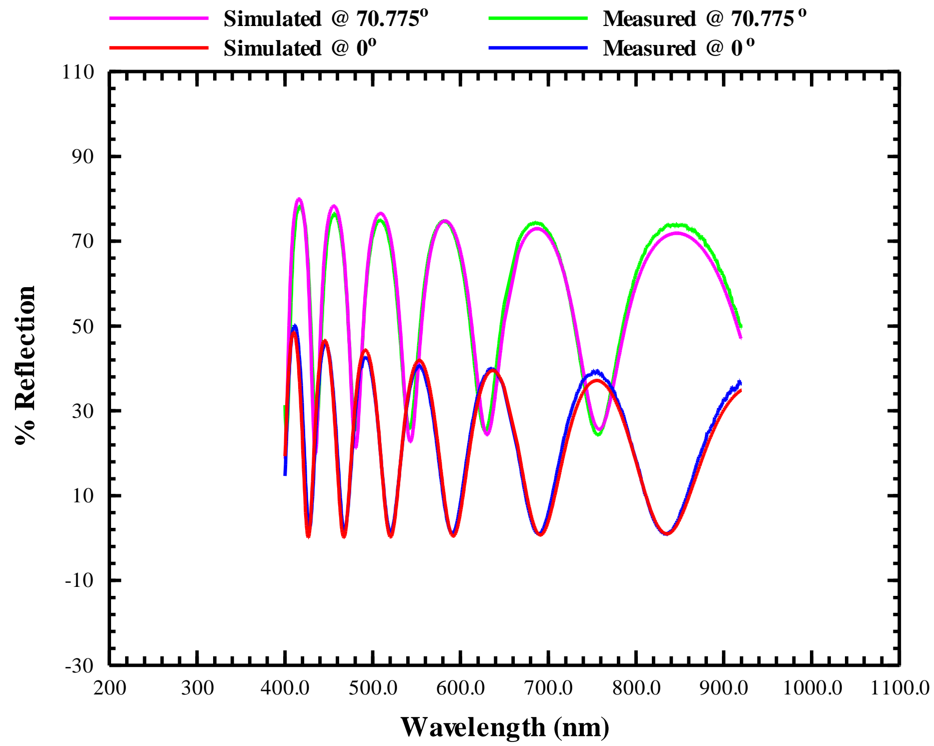

Data Obtained	
Thickness	858.24 nm
Index @ 632 nm (max)	2.27359
Extinction coefficient @ 632 nm	0.0000
RMSE	2.325

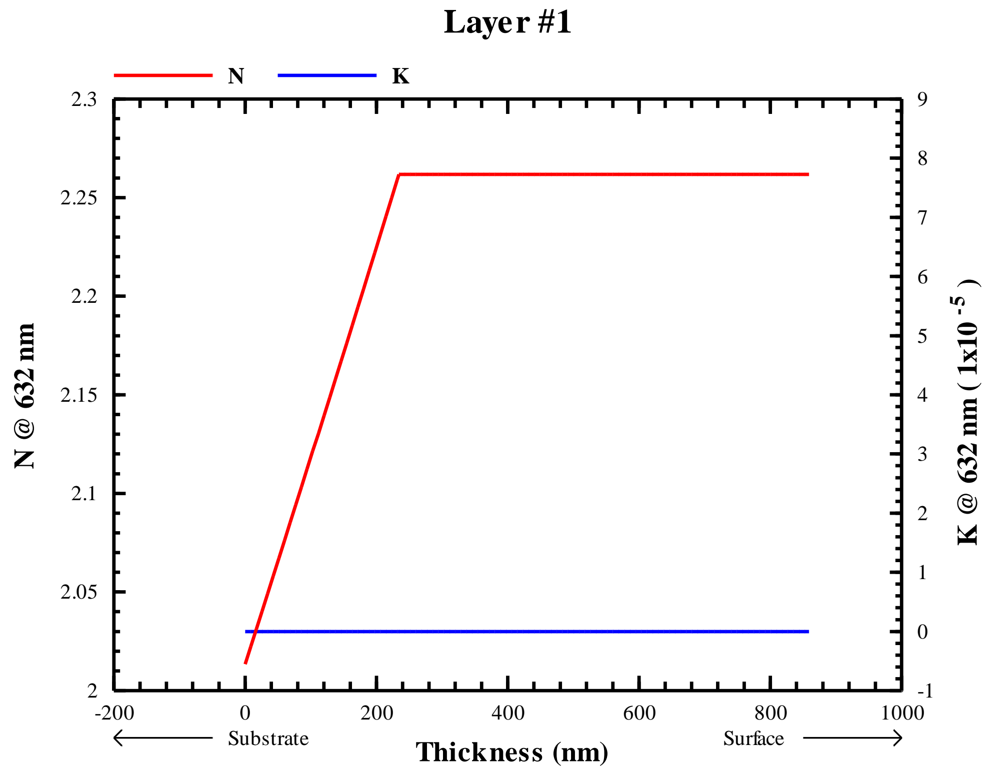

Layer #1 Material Coefficient Table	
EMA Screening	0.3333
EMA Type	Landau-Lifshitz
Number Nodes	3
HOST MATERIAL	Same As Layer #2
Material #2	Same As Layer #3
% POSITION NODE #1	0.00
% POSITION NODE #2	27.30
% POSITION NODE #3	100.00
% FRACTION Same As Layer #3 NODE #1	0.0000
% FRACTION Same As Layer #3 NODE #2	100.0000
% FRACTION Same As Layer #3 NODE #3	100.0000

DK14_1

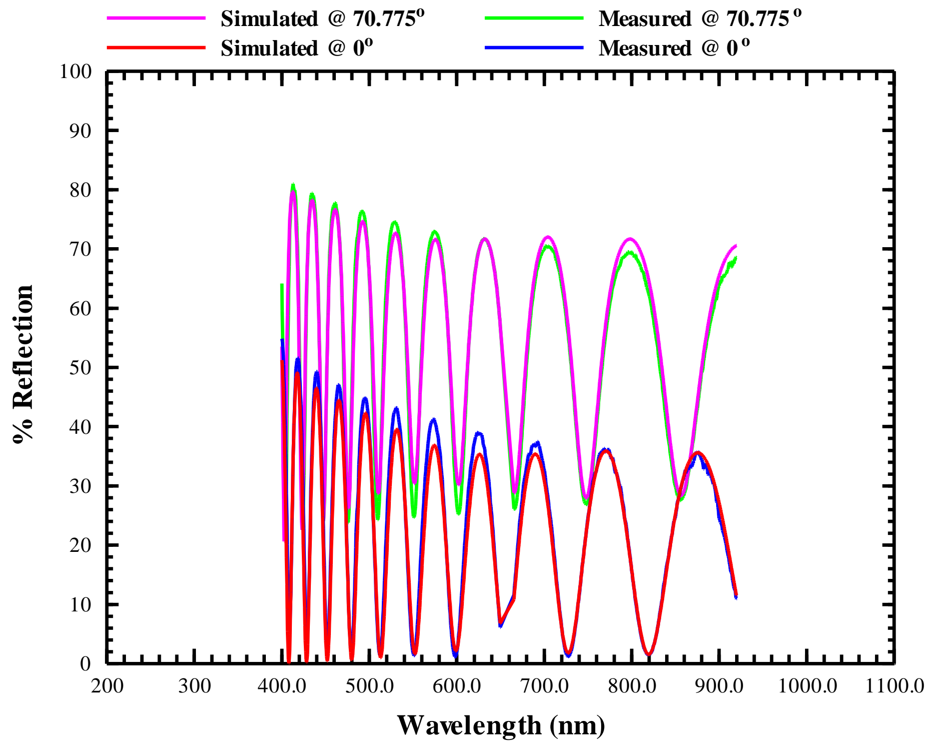

Data Obtained	
Thickness	1370.12 nm
Index @ 632 nm (max)	2.30412
Extinction coefficient @ 632 nm	0.0000
RMSE	2.553

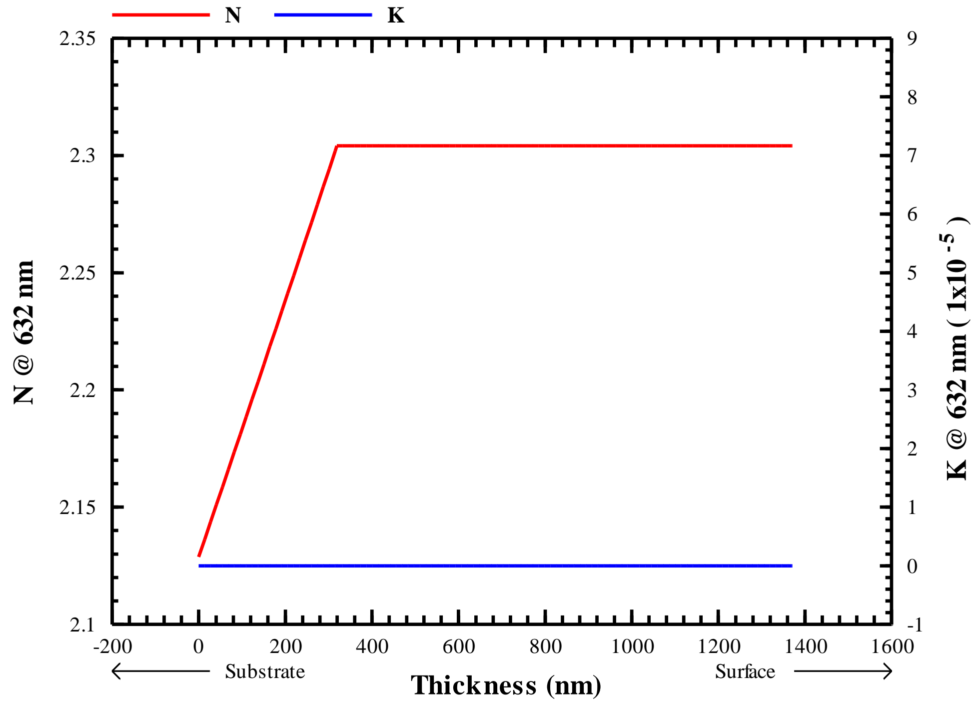

Layer #1 Material Coefficient Table	
EMA Screening	0.3333
EMA Type	Landau-Lifshitz
Number Nodes	3
HOST MATERIAL	Same As Layer #2
Material #2	Same As Layer #3
% POSITION NODE #1	0.00
% POSITION NODE #2	25.22
% POSITION NODE #3	100.00
% FRACTION Same As Layer #3 NODE #1	0.0000
% FRACTION Same As Layer #3 NODE #2	100.0000
% FRACTION Same As Layer #3 NODE #3	100.0000

DN64_1

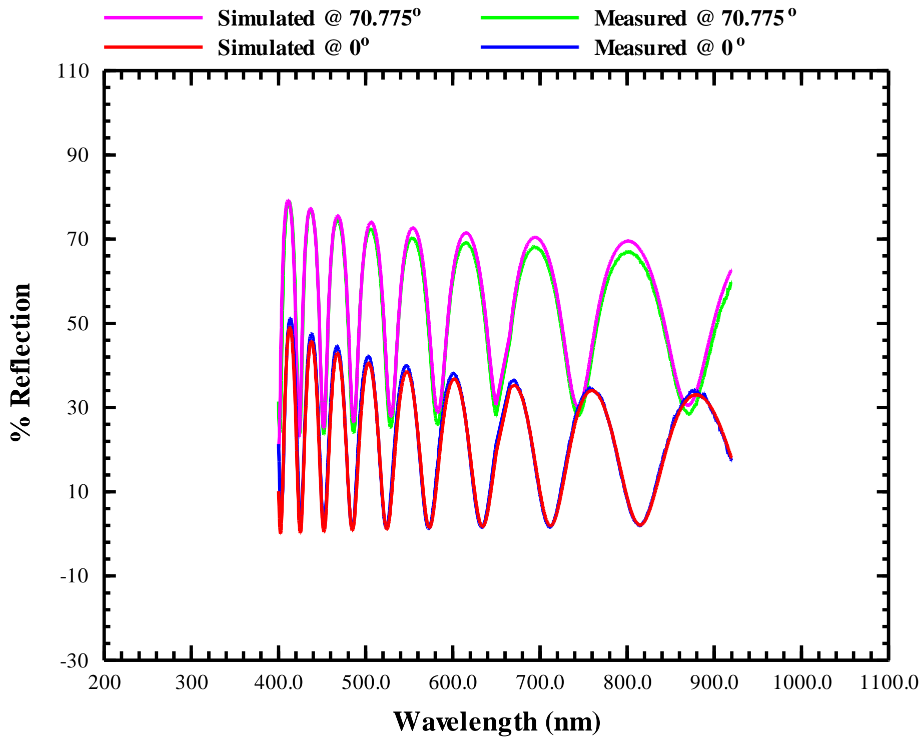

Data Obtained	
Thickness	1180.97 nm
Index @ 632 nm (max)	2.28078
Extinction coefficient @ 632 nm	0.0000
RMSE	2.003

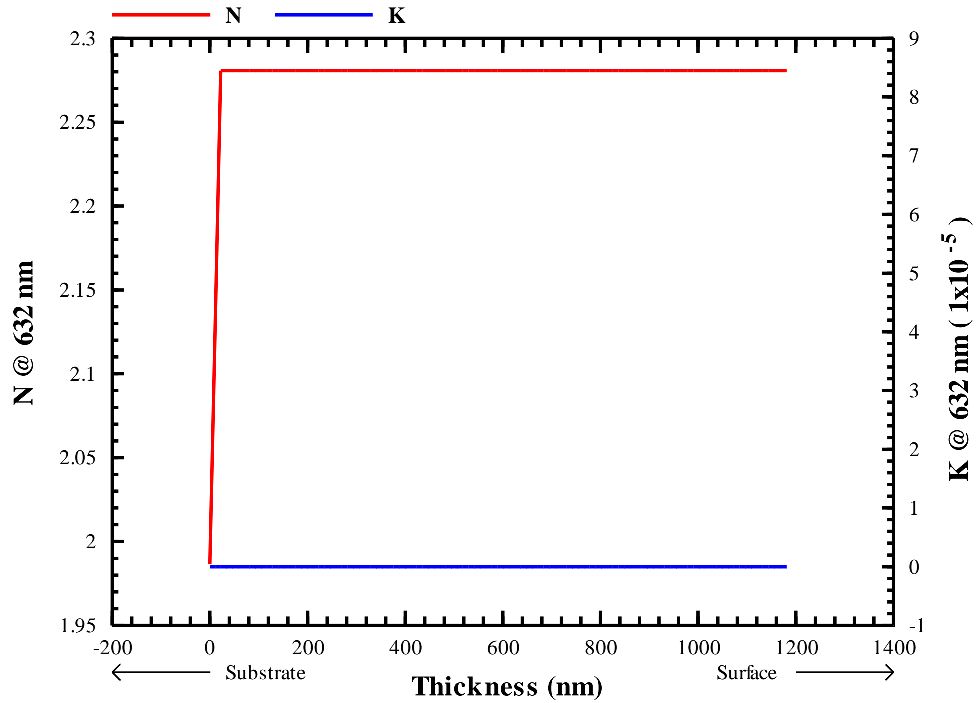

Layer #1 Material Coefficient Table	
EMA Screening	0.3333
EMA Type	Landau-Lifshitz
Number Nodes	3
HOST MATERIAL	Same As Layer #2
Material #2	Same As Layer #3
% POSITION NODE #1	0.00
% POSITION NODE #2	1.85
% POSITION NODE #3	100.00
% FRACTION Same As Layer #3 NODE #1	0.0000
% FRACTION Same As Layer #3 NODE #2	99.9994
% FRACTION Same As Layer #3 NODE #3	100.0000

DN66_1

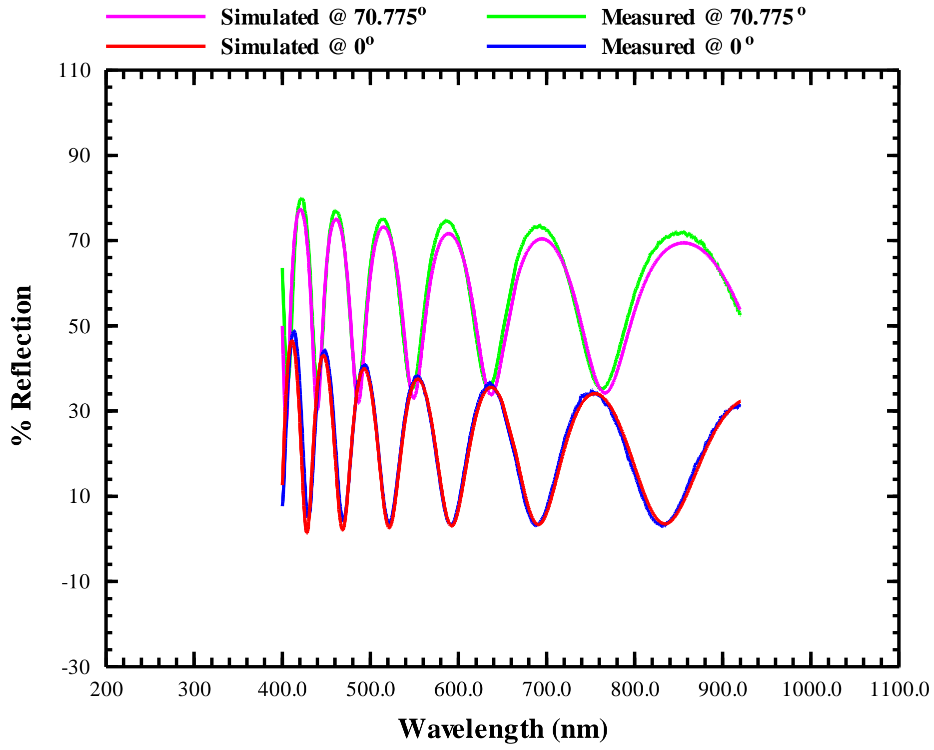

Data Obtained	
Thickness	810.12 nm
Index @ 632 nm (max)	2.36684
Extinction coefficient @ 632 nm	0.0000
RMSE	2.618

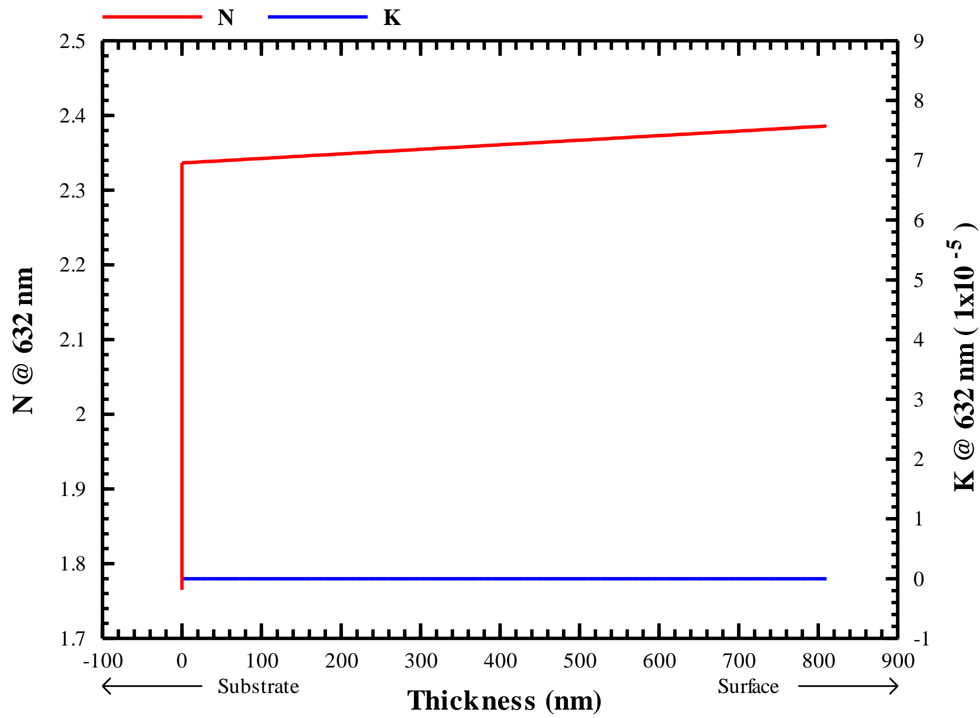

Layer #1 Material Coefficient Table	
EMA Screening	0.3333
EMA Type	Landau-Lifshitz
Number Nodes	3
HOST MATERIAL	Same As Layer #2
Material #2	Same As Layer #3
% POSITION NODE #1	0.00
% POSITION NODE #2	0.00
% POSITION NODE #3	100.00
% FRACTION Same As Layer #3 NODE #1	0.0000
% FRACTION Same As Layer #3 NODE #2	92.3816
% FRACTION Same As Layer #3 NODE #3	100.0000

DN63_1

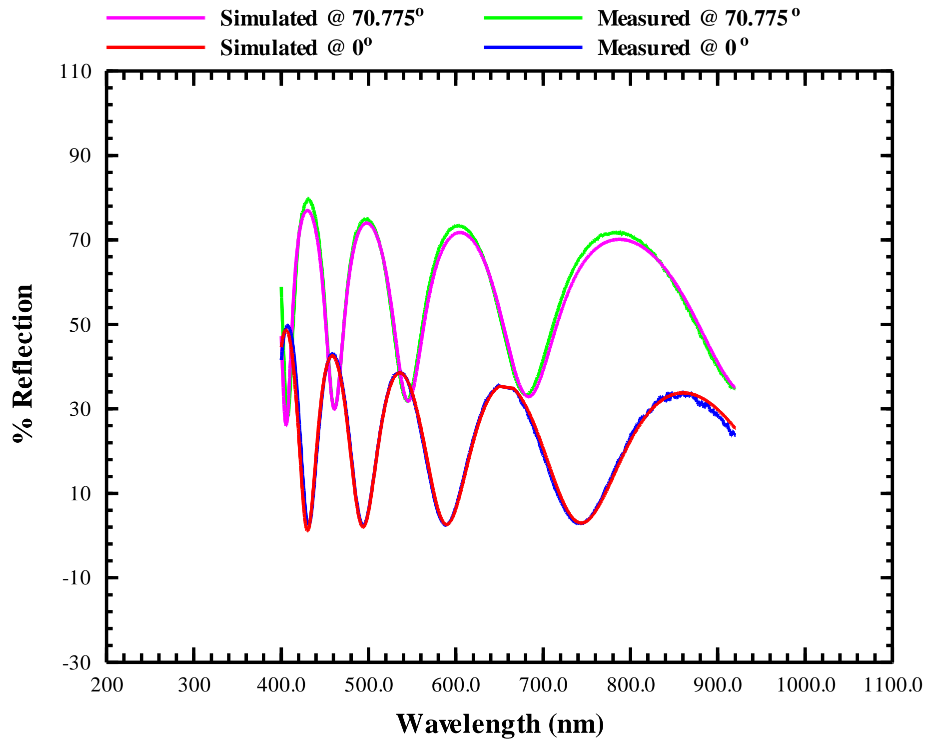

Data Obtained	
Thickness	564.88 nm
Index @ 632 nm (max)	2.32958
Extinction coefficient @ 632 nm	0.0000
RMSE	1.638

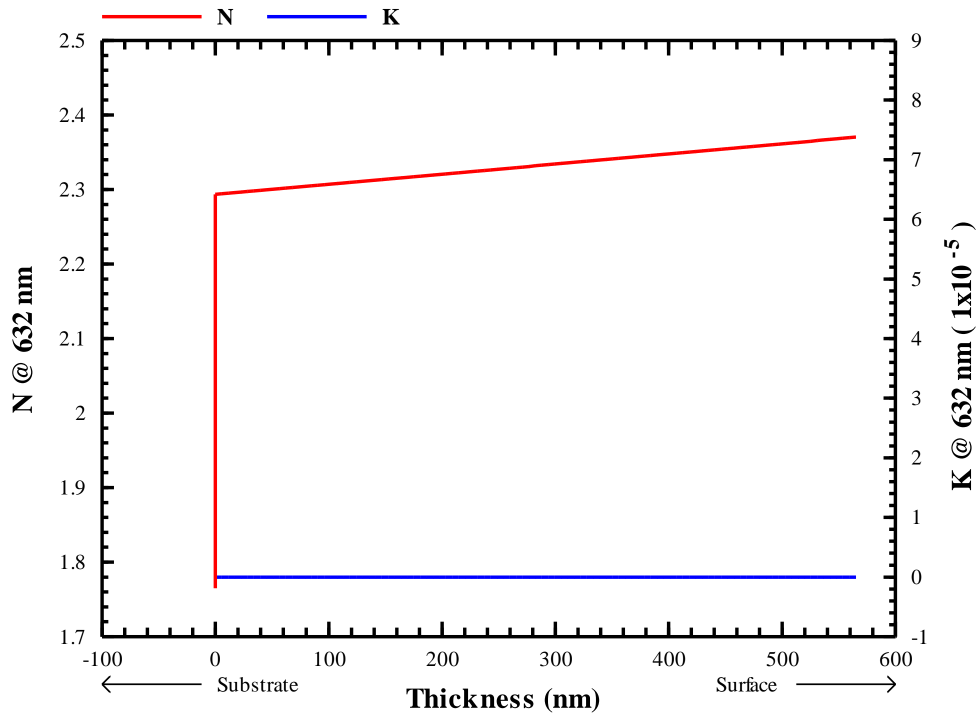

Layer #1 Material Coefficient Table	
EMA Screening	0.3333
EMA Type	Landau-Lifshitz
Number Nodes	3
HOST MATERIAL	Same As Layer #2
Material #2	Same As Layer #3
% POSITION NODE #1	0.00
% POSITION NODE #2	0.00
% POSITION NODE #3	100.00
% FRACTION Same As Layer #3 NODE #1	0.0000
% FRACTION Same As Layer #3 NODE #2	87.8428
% FRACTION Same As Layer #3 NODE #3	100.0000

DN67_1

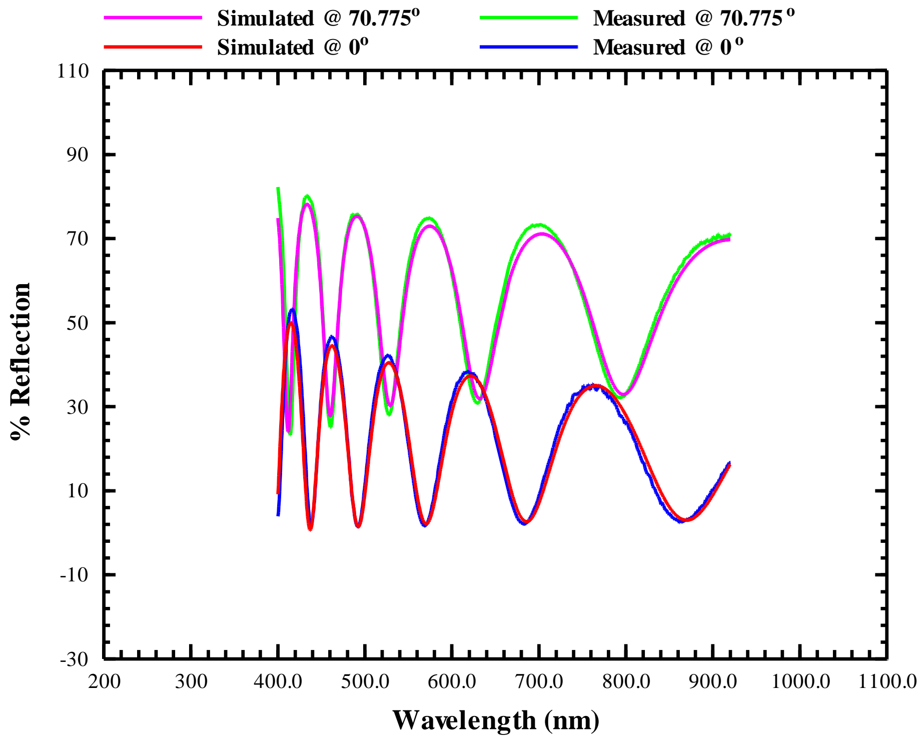

Data Obtained	
Thickness	660.52 nm
Index @ 632 nm (max)	2.38458
Extinction coefficient @ 632 nm	0.0000
RMSE	2.561

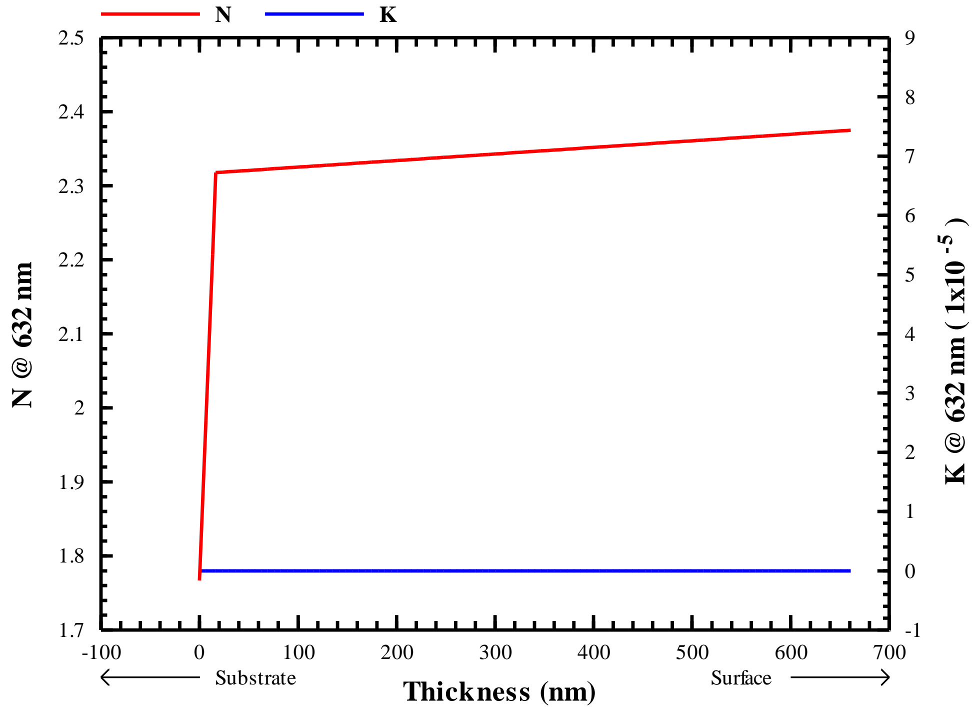

Layer #1 Material Coefficient Table	
EMA Screening	0.3333
EMA Type	Landau-Lifshitz
Number Nodes	3
HOST MATERIAL	Same As Layer #2
Material #2	Same As Layer #3
% POSITION NODE #1	0.00
% POSITION NODE #2	0.00
% POSITION NODE #3	100.00
% FRACTION Same As Layer #3 NODE #1	0.0000
% FRACTION Same As Layer #3 NODE #2	90.9855
% FRACTION Same As Layer #3 NODE #3	100.0000

B2: STO on Platinum

DK17_1

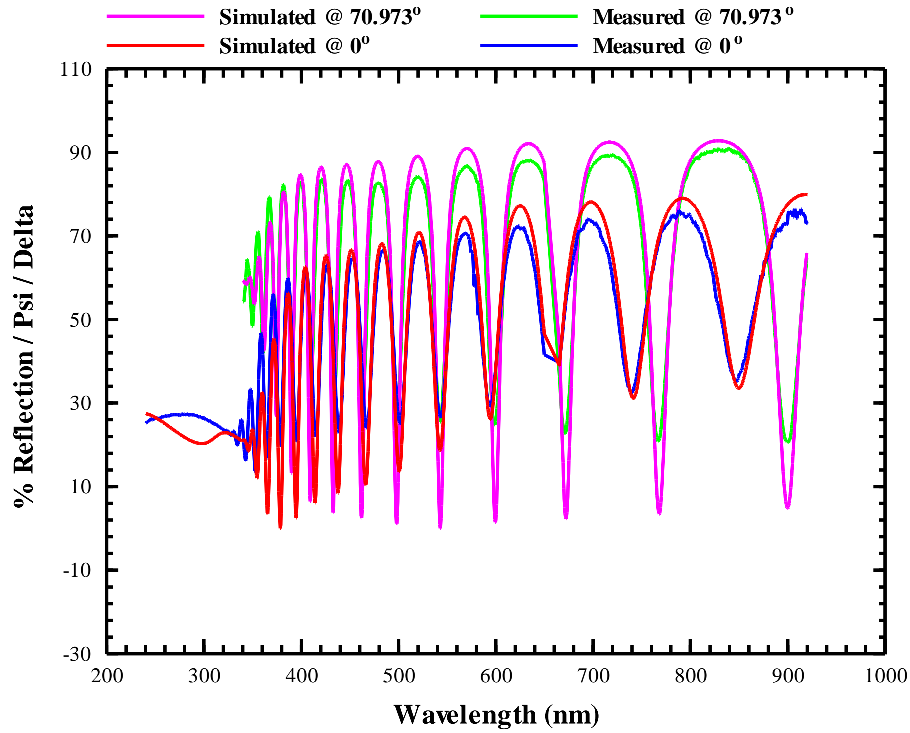

Data Obtained	
Thickness Layer 1	1263.73 nm
Index @ 632 nm	2.19165
Extinction coefficient @ 632 nm	0.0000
RMSE	6.286

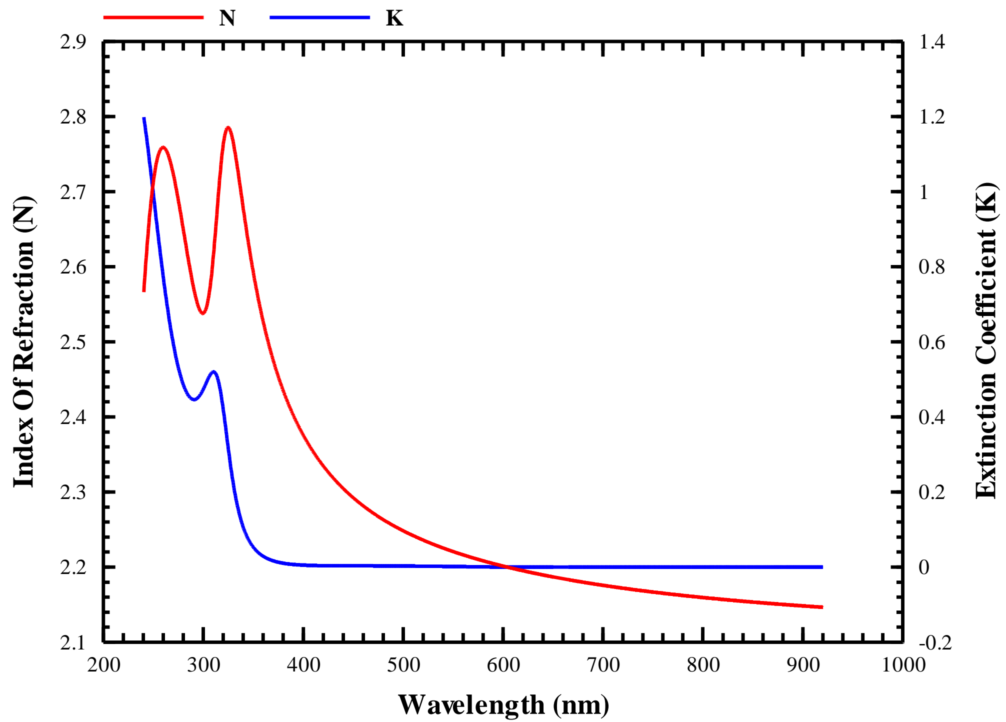

Layer #1 Material Coefficient Table	
Number of Oscillators	3
HF Diel. Const.	1.870243
Damping Coef.	1.416726
Amplitude(1)	1.340045
C. Energy(1)	3.899847
Vib. Freq.(1)	0.432933
Amplitude(2)	4.633465
C. Energy(2)	5.062884
Vib. Freq.(2)	1.565297
Amplitude(3)	2.316636
C. Energy(3)	3.593737
Vib. Freq.(3)	4.462680

DK19_1

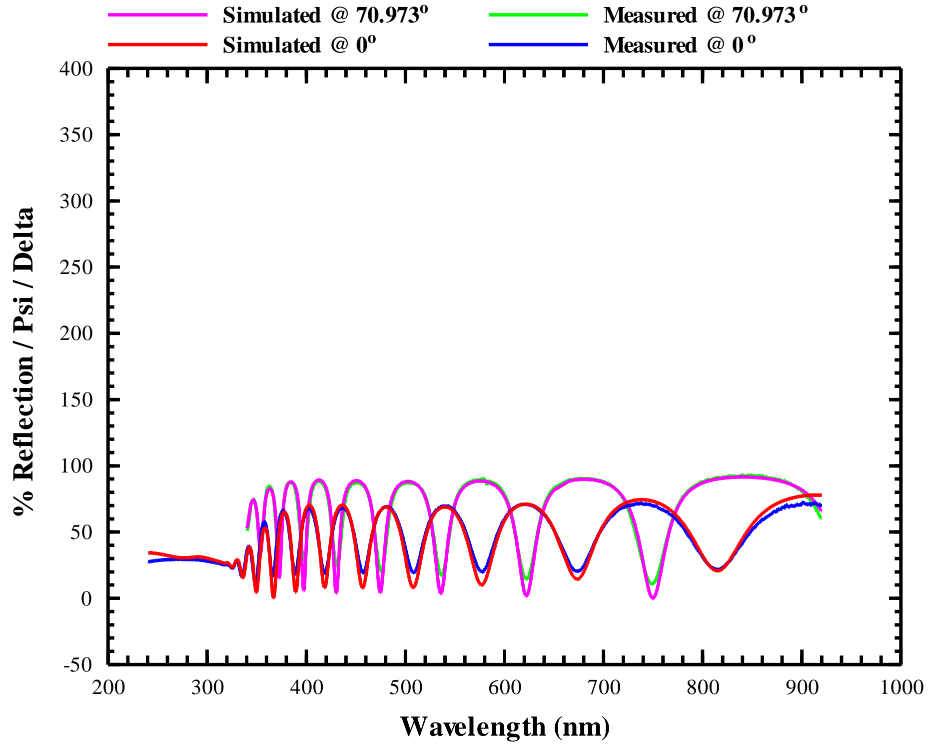

Data Obtained	
Thickness Layer 1	761.95 nm
Index @ 632 nm	2.38630
Extinction coefficient @ 632 nm	0.0068
RMSE	4.272

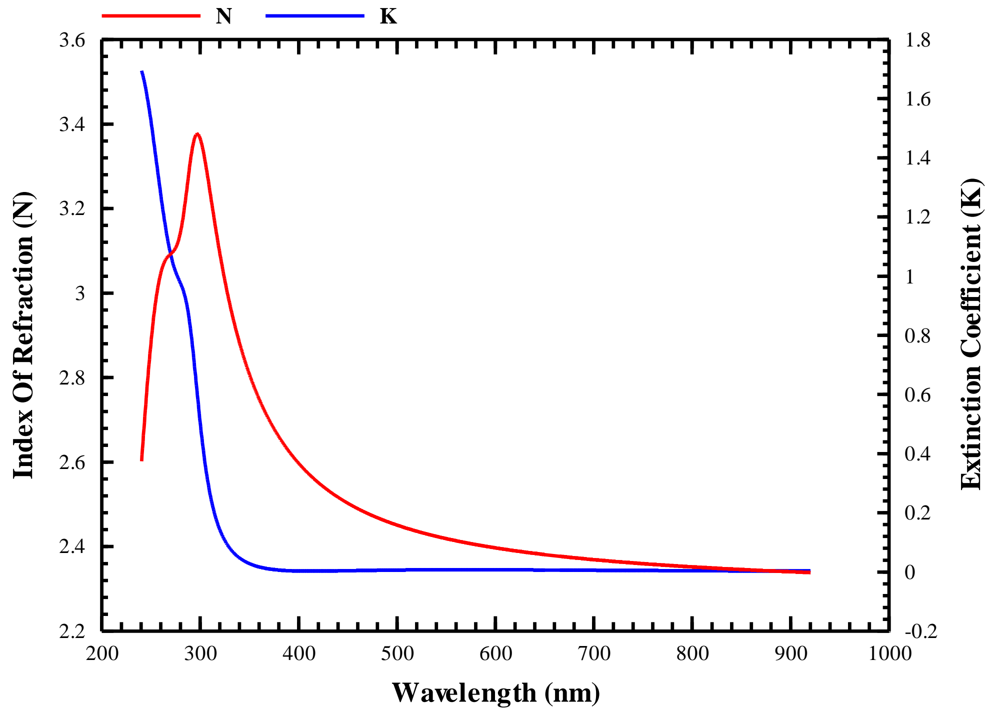

Layer #1 Material Coefficient Table	
Number of Oscillators	3
HF Diel. Const.	2.085630
Damping Coef.	1.311789
Amplitude(1)	1.838130
C. Energy(1)	4.251272
Vib. Freq.(1)	0.506801
Amplitude(2)	4.740899
C. Energy(2)	4.926421
Vib. Freq.(2)	1.342757
Amplitude(3)	2.310264
C. Energy(3)	3.571693
Vib. Freq.(3)	4.742648

DK29_2

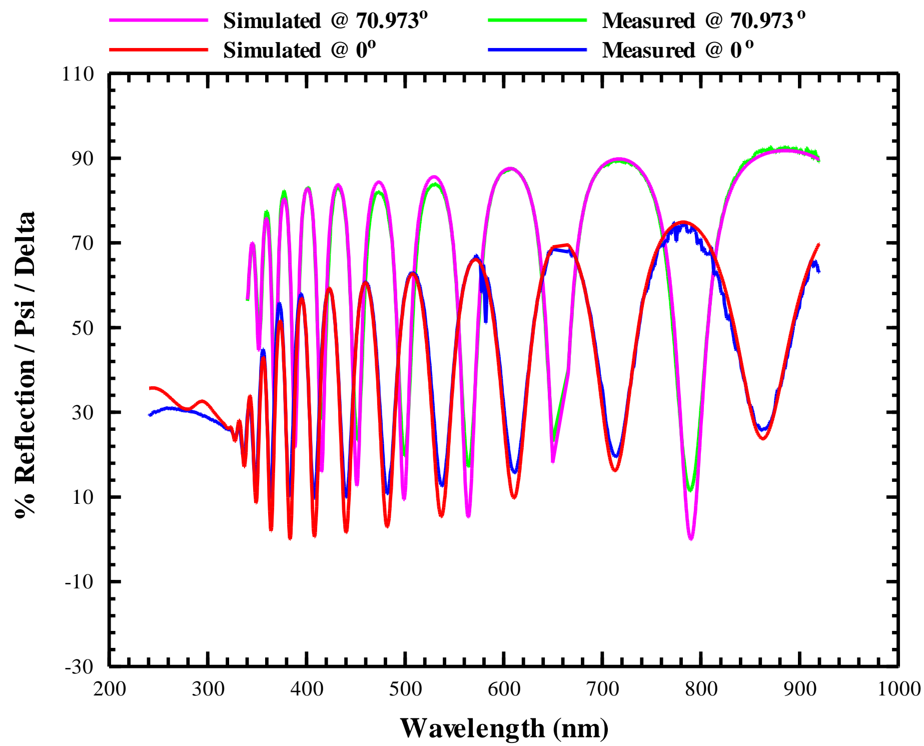

Obtained Data	
Thickness Layer 1	830.07 nm
Index @ 632 nm	2.33335
Extinction coefficient @ 632 nm	0.0082
RMSE	3.082

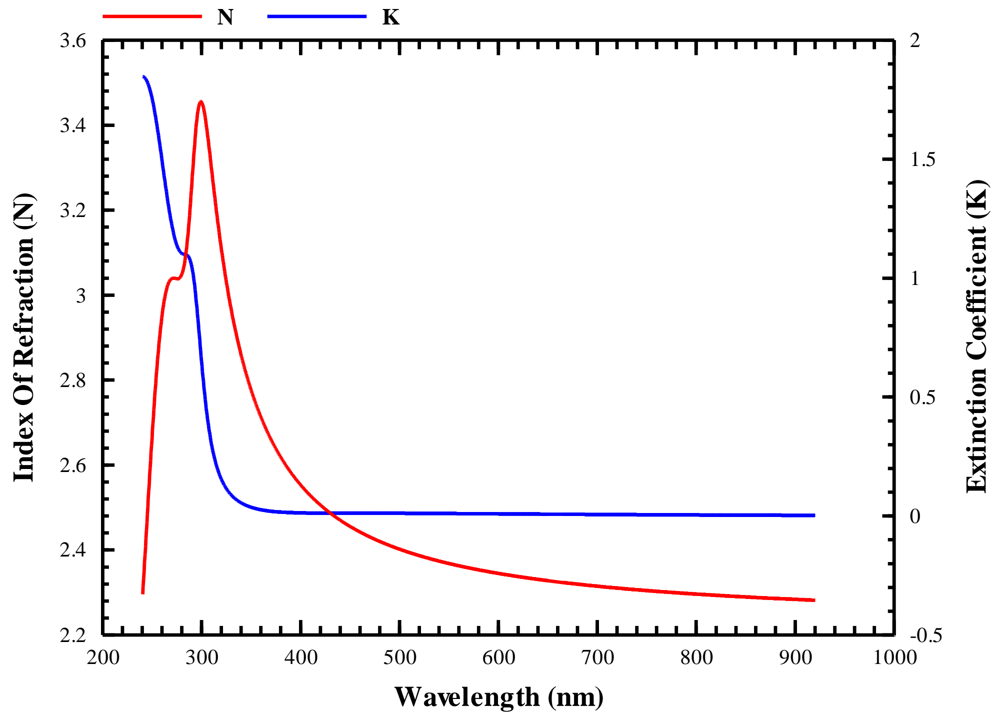

Layer #1 Material Coefficient Table	
Number of Oscillators	3
HF Diel. Const.	2.046745
Damping Coef.	1.246549
Amplitude(1)	1.860763
C. Energy(1)	4.215465
Vib. Freq.(1)	0.396009
Amplitude(2)	4.479463
C. Energy(2)	4.831295
Vib. Freq.(2)	1.123487
Amplitude(3)	2.350674
C. Energy(3)	3.748690
Vib. Freq.(3)	4.680787

DN66_2

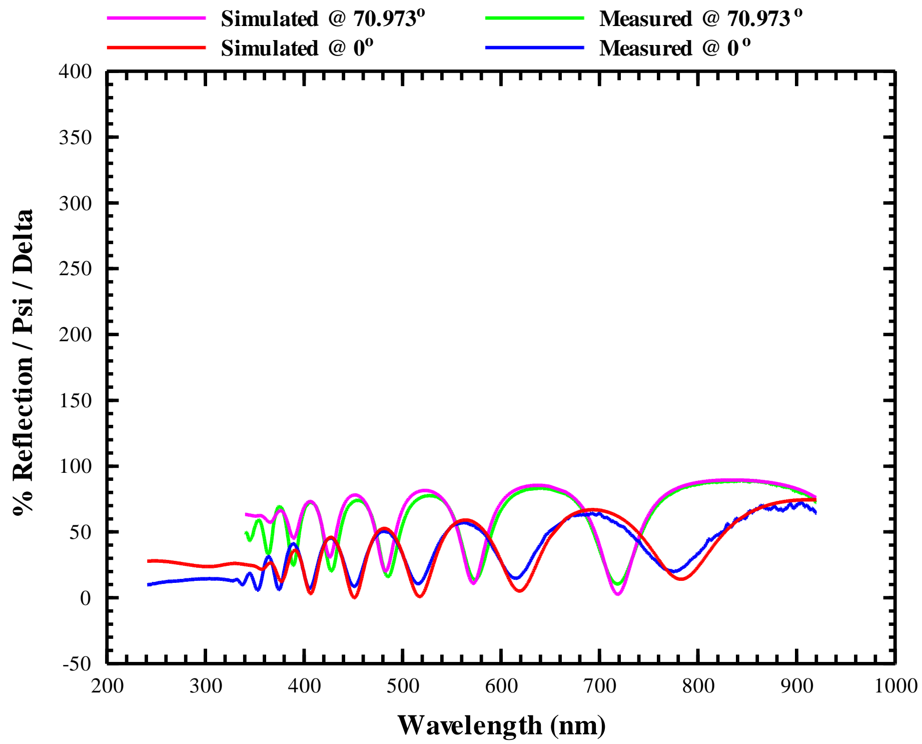

Data Obtained	
Thickness Layer 1	578.01 nm
Index @ 632 nm	2.33400
Extinction coefficient @ 632 nm	0.0204
RMSE	6.727

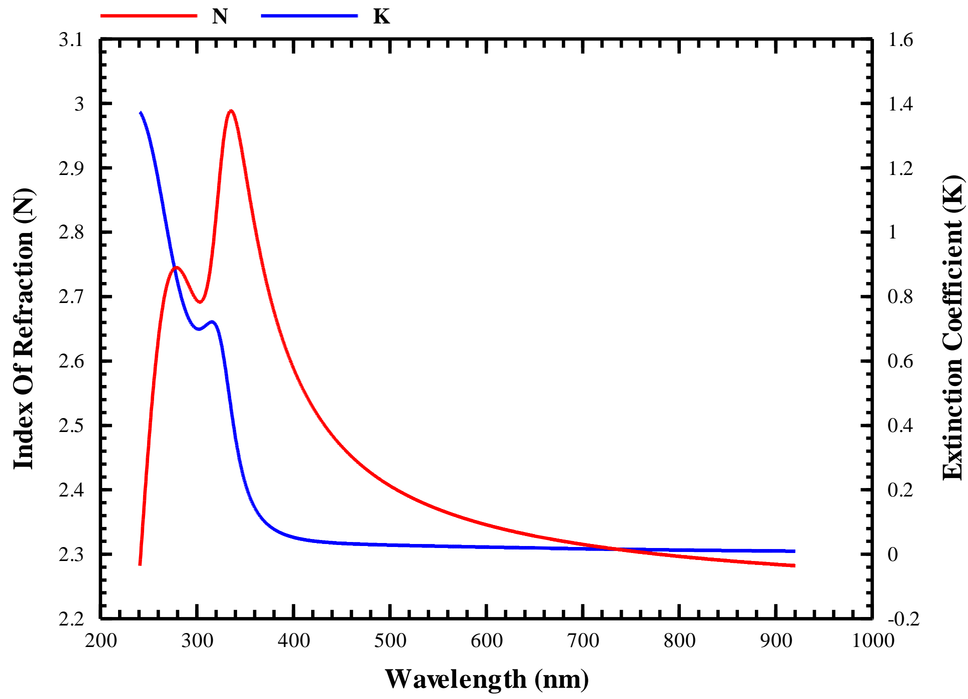

Layer #1 Material Coefficient Table	
Number of Oscillators	3
HF Diel. Const.	2.017232
Damping Coef.	1.246507
Amplitude(1)	1.534128
C. Energy(1)	3.791492
Vib. Freq.(1)	0.492150
Amplitude(2)	4.555559
C. Energy(2)	4.788460
Vib. Freq.(2)	1.691983
Amplitude(3)	2.163097
C. Energy(3)	3.365806
Vib. Freq.(3)	4.404778

BIBLIOGRAPHY

CHAPTER 1 REFERENCES

1. Young, H. D.; Freedman, R. A., *University Physics*. 9th Ed. ed.; Addison-Wesley Publishing Company: 1996; Vol. Vol. 2.

2. Kerker, M., *The scattering of light and other electromagnetic radiation*. Academic, New York: 1969.

3. Hulst, H. C. v. d., *Light Scattering by Small Particles*. Dover Publications, New York: 1981.

4. Tompkins, H. G.; McGahan, W. A., *Spectroscopic Ellipsometry and Reflectometry: A User's Guide*. John Wiley and Sons, Inc.: 1999.

5. Hecht, E., *Optics*. 2nd Ed. ed.; Addison-Wesley: 1987.

6. Hummel, R. E., *Electronic Properties of Materials*. 3 ed.; Springer-Verlag: 2001.

7. Azaroff, L. V., *Introduction to Solids*. Tata McGraw-Hill Publishing Company Limited: 1977; p 460.

8. West, A. R., *Solid State Chemistry and its Applications*. John Wiley and Sons: 1984.

9. Chopra, K. L., *Thin Film Phenomena*. McGraw-Hill: 1969.

10. Heavens, O. S., *Optical Properties of Thin Solid Films*. Dover Publications Inc.: 1991.

CHAPTER 2 REFERENCES

1. Heavens, O. S., *Optical Properties of Thin Solid Films*. Dover Publications Inc.: 1991.

2. Chopra, K. L., *Thin Film Phenomena*. McGraw-Hill: 1969.

2. Chopra, K. L.; Kaur, I., *Thin Film Device Applications*. Plenum Press: 1983.

CHAPTER 3 REFERENCES

1. Fujiwara, H., *Spectroscopic Ellipsometry Principles and Applications*. John Wiley and Sons, Ltd.: 2007.

2. Tompkins, H. G.; McGahan, W. A., *Spectroscopic Ellipsometry and Reflectometry: A User's Guide*. John Wiley and Sons, Inc.: 1999.

3. Vedam, K., Spectroscopic Ellipsometry: a Historical Overview. *Thin Solid Films* **1998,** 313-314, 1 - 9.

4. Aspnes, D. E., Expanding Horizons: New Developments in Ellipsometry and Polarimetry. *Thin Solid Films* **2004,** 455-456, 3-13.

5. Hilfiker, J. N.; Hale, J. S.; Johs, B. D.; Tiwald, T. E.; Synowicki, R. A.; Bungay, C. L.; Woolam, J. A., Spectroscopic Ellipsometry in Optical Coatings Manufacturing. *Society of Vacuum Coaters* **2001,** 505, 295-300.

6. Azzam, R. M. A.; Bashara, N. M., *Ellipsometry and Polarized Light*. 2nd ed.; North Holland Press, Amsterdam: 1987.

7. SCI, *FilmTek (TM) 3000SE Operations Manual*. Scientific Computing International: 2006.

CHAPTER 4 REFERENCES

1. Kowach, G. R.; Mirica, E.; Jones, C. D. W.; Dennis, B. S.; Pinczuk, A.; Safar, H.; Kleiman, R. N.; Kammlott, G. W., Properties of Radio Frequency (RF) Sputtered Zinc Oxide Thin Films for Piezoelectric Applications. *Lucent Technologies Technical Memorandum* **1999**.

2. Bagnall, D. M.; Chen, Y. F.; Zhu, Z.; Yao, T.; Koyama, S.; Shen, M. Y.; Goto, T., Optically pumped lasing of ZnO at room temperature. *Applied Physics Letters* **1997,** 70, (17), 2230-2232.

3. Tang, Z. K.; Wong, G. K. L.; Yu, P.; Kawasaki, M.; Ohtomo, A.; Koinuma, H.; Segawa, Y., Room-temperature ultraviolet laser emission from self-assembled ZnO microcrystallite thin films. *Applied Physics Letters* **1998,** 72, (25), 3270-3272.

4. Washington, P. L.; Ong, H. C.; Dai, J. Y.; Chang, R. P. H., Determination of the optical constants of zinc oxide thin films by spectroscopic ellipsometry. *Applied Physics Letters* **1998,** 72, (25), 3261-3263.

4. Hu, W. S.; Liu, Z. G.; Sun, J.; Zhu, S. N.; Xu, Q. Q.; Feng, D.; Ji, Z. M., Optical Properties of Pulsed Laser Deposited ZnO Thin Films. *Journal of Physics and Chemistry of Solids* **1997,** 58, (6), 853-857.

5. Liu, Y. C.; Hsieh, J. H.; Tung, S. K., Extraction of optical constants of zinc oxide thin films by ellipsometry with various models. *Thin Solid Films* **2006,** 510, 32-38.

6. Dumont, E.; Dugnoille, B.; Bienfait, S., Simultaneous determination of the optical properties and of the structure of r.f.-sputtered ZnO thin films. *Thin Solid Films* **1999,** 353, (1-2), 93-99.

7. G. E. Jellison, J.; Boatner, L. A., Optical Functions of Uniaxial ZnO determined by Generalized Ellipsometry. *Physical Review B* **1998,** 58, (7), 3586-3589.

8. Liang, W. Y.; Yoffe, A. D., Transmission Spectra of ZnO Single Crystals. *Physical Review Letters* **1968,** 20, (2), 59.

10. Matz, R.; Lüth, H., Ellipsometric spectroscopy of the ZnO nonpolar surface. *Applied Physics A: Materials Science & Processing* **1979,** 18, (2), 123-130.

11. Rebien, M.; Henrion, W.; Bar, M.; Fischer, C.-H., Optical properties of ZnO thin films: Ion layer gas reaction compared to sputter deposition. *Applied Physics Letters* **2002,** 80, (19), 3518-3520.

12. Kang, S. J.; Joung, Y. H., Influence of substrate temperature on the optical and piezoelectric properties of ZnO thin films deposited by RF magnetron sputtering. *Applied Surface Science* **2007,** 253, (17), 7330-7335.

13. Cetinorgu, E.; Goldsmith, S.; Zhitomirsky, V. N.; Boxman, R. L.; Bungay, C. L., Optical characterization of filtered vacuum arc deposited zinc oxide thin films. *Semiconductor Science and Technology* **2006,** 21, (9), 1303-1310.

14. Tompkins, H. G.; McGahan, W. A., *Spectroscopic Ellipsometry and Reflectometry: A User's Guide*. John Wiley and Sons, Inc.: 1999.

15. Chopra, K. L., *Thin Film Phenomena*. McGraw-Hill: 1969.

16. Mirica, E.; Kowach, G.; Evans, P.; Du, H., Morphological Evolution of ZnO Thin Films Deposited by Reactive Sputtering. *Crystal Growth and Design* **2004,** 4, (1), 147-156.

17. SCI, *FilmTek (TM) 3000SE Operations Manual*. Scientific Computing International: 2006.

18. Cetinorgu, E.; Goldsmith, S.; Boxman, R. L., The effect of substrate temperature on filtered vacuum arc deposited zinc oxide and tin oxide thin films. *Journal of Crystal Growth* **2007,** 299, (2), 259-267.

19. Heitsch, S.; Bundesmann, C.; Wagner, G.; Zimmermann, G.; Rahm, A.; Hochmuth, H.; Benndorf, G.; Schmidt, H.; Schubert, M.; Lorenz, M.; Grundmann, M., Low temperature photoluminescence and infrared dielectric functions of pulsed laser deposited ZnO thin films on silicon. *Thin Solid Films* **2006,** 496, (2), 234-239.

20. Kim, K.-S.; Kim, H. W.; Lee, C. M., Effect of growth temperature on ZnO thin film deposited on SiO2 substrate. *Materials Science and Engineering B* **2003,** 98, (2), 135-139.

21. Singh, S.; Srinivasa, R. S.; Major, S. S., Effect of substrate temperature on the structure and optical properties of ZnO thin films deposited by reactive rf magnetron sputtering. *Thin Solid Films* **2007,** 515, (24), 8718-8722.

22. Bond, W. L., Measurement of the Refractive Indices of Several Crystals. *Journal of Applied Physics* **1965,** 36, (5), 1674-1677.

23. Park, Y. S.; Schneider, J. R., Index of Refraction of ZnO. *Journal of Applied Physics* **1968,** 39, (7), 3049-3052.

24. Inukai, T.; Matsuoka, M.; Ono, K., Characteristics of zinc oxide thin films prepared by r.f. magnetron-mode electron cyclotron resonance sputtering. *Thin Solid Films* **1995,** 257, (1), 22-27.

25. Gupta, V.; Mansingh, A., Influence of postdeposition annealing on the structural and optical properties of sputtered zinc oxide film. *Journal of Applied Physics* **1996,** 80, 1063.

26. Sun, X. W., Optical properties of epitaxially grown zinc oxide films on sapphire by pulsed laser deposition. *Journal of Applied Physics* **1999,** 86, (1), 408.

27. Zayer, N. K.; Greef, R.; Rogers, K.; Grellier, A. J. C.; Pannell, C. N., In situ monitoring of sputtered zinc oxide films for piezoelectric transducers. *Thin Solid Films* **1999,** 352, (1-2), 179-184.

28. Postava, K.; Sueki, H.; Aoyama, M.; Yamaguchi, T.; Ch, I.; Igasaki, Y.; Horie, M., Spectroscopic ellipsometry of epitaxial ZnO layer on sapphire substrate. *Journal of Applied Physics* **2000,** 87, (11), 7820-7824.

29. Moustaghfir, A.; Tomasella, E.; Ben Amor, S.; Jacquet, M.; Cellier, J.; Sauvage, T., Structural and optical studies of ZnO thin films deposited by r.f. magnetron sputtering: influence of annealing. *Surface and Coatings Technology* **2003,** 174-175, 193-196.

30. Ondo-Ndong, R.; Ferblantier, G.; Al Kalfioui, M.; Boyer, A.; Foucaran, A., Properties of RF magnetron sputtered zinc oxide thin films. *Journal of Crystal Growth* **2003,** 255, (1-2), 130-135.

31. Ondo-Ndong, R.; Pascal-Delannoy, F.; Boyer, A.; Giani, A.; Foucaran, A., Structural properties of zinc oxide thin films prepared by r.f. magnetron sputtering. *Materials Science and Engineering B* **2003,** 97, (1), 68-73.

32. Mehan, N.; Gupta, V.; Sreenivas, K.; Mansingh, A., Effect of annealing on refractive indices of radio-frequency magnetron sputtered waveguiding zinc oxide films on glass. *Journal of Applied Physics* **2004,** 96, (6), 3134-3139.

33. Shan, F. K.; Liu, G. X.; Lee, W. J.; Lee, G. H.; Kim, I. S.; Shin, B. C.; Kim, Y. C., Transparent conductive ZnO thin films on glass substrates deposited by pulsed laser deposition. *Journal of Crystal Growth* **2005,** 277, (1-4), 284-292.

34. Liu, Y. C.; Tung, S. K.; Hsieh, J. H., Influence of annealing on optical properties and surface structure of ZnO thin films. *Journal of Crystal Growth* **2006,** 287, (1), 105-111.

35. Senadim, E.; Eker, S.; Kavak, H.; Esen, R., Optical and structural parameters of the ZnO thin film grown by pulsed filtered cathodic vacuum arc deposition. *Solid State Communications* **2006,** 139, (9), 479-484.

36. Cetinorgu, E., Characteristics of filtered vacuum arc deposited ZnO-SnO2 thin films on room temperature substrates. *Optics Communications* **2007,** 280, (1), 114-119.

37. Gioffre, M.; Angeloni, M.; Gagliardi, M.; Iodice, M.; Coppola, G.; Aruta, C.; Della Corte, F. G., The influence of oxygen on the optical properties of RF-sputtered zinc oxide thin films. *Superlattices and Microstructures* **2007,** 42, (1-6), 85-88.

38. Kang, S.; Joung, Y.; Chang, D.; Kim, K., Piezoelectric and optical properties of ZnO thin films deposited using various O2/(Ar+O2) gas ratios. *Journal of Materials Science: Materials in Electronics* **2007,** 18, (6), 647-653.

39. Khoshman, J. M.; Kordesch, M. E., Optical constants and band edge of amorphous zinc oxide thin films. *Thin Solid Films* **2007,** 515, (18), 7393-7399.

40. Khandelwal, R.; Singh, A. P.; Kapoor, A.; Grigorescu, S.; Miglietta, P.; Stankova, N. E.; Perrone, A., Effects of deposition temperature on the structural and morphological properties of thin ZnO films fabricated by pulsed laser deposition. *Optics & Laser Technology* **2008,** 40, (2), 247-251.

41. Azaroff, L. V., *Introduction to Solids*. Tata McGraw-Hill Publishing Company Limited: 1977; p 460.

42. Moulson, A. J.; Herbert, J. M., *Electroceramics: Materials, Properties, Applications*. Chapman and Hall: 1990.

43. Fujiwara, H., *Spectroscopic Ellipsometry Principles and Applications*. John Wiley and Sons, Ltd.: 2007.

44. Aspnes, D. E., Approximate Solution of Ellipsometric Equations for Optically Biaxial Crystals. *Journal of the Optical Society of America* **1980,** 70, (10), 1275-1277.

45. Nikogosyan, D. N., *Properties of Optical and Laser-Related Materials: A Handbook*. John Wiley and Sons: 1997.

CHAPTER 5 REFERENCES

1. Hubert, T.; Beck, U.; Kleinke, H., Amorphous and nanocrystalline $SrTiO_3$ thin films. *Journal of Non-Crystalline Solids* **1996,** 196, 150-154.

2. Taylor, T. R.; Hansen, P. J.; Pervez, N.; Acikel, B.; York, R. A.; Speck, J. S., Influence of stoichiometry on the dielectric properties of sputtered strontium titanate thin films. *Journal of Applied Physics* **2003,** 94, (5), 3390.

3. Du, Y.; Zhang, M.-S.; Wu, J.; Kang, L.; Yang, S.; Wu, P.; Yin, Z., Optical properties of $SrTiO_3$ thin films by pulsed laser deposition. *Applied Physics A: Materials Science & Processing* **2003,** 76, (7), 1105.

4. Goncharova, L. V.; Starodub, D. G.; Garfunkel, E.; Gustafsson, T.; Vaithyanathan, V.; Lettieri, J.; Schlom, D. G., Interface structure and thermal stability of epitaxial $SrTiO_3$ thin films on Si (001). *Journal of Applied Physics* **2006,** 100, (1), 014912.

5. Ma, J. H.; Huang, Z. M.; Meng, X. J.; Liu, S. J.; Zhang, X. D.; Sun, J. L.; Xue, J. Q.; Chu, J. H., Optical Properties of $SrTiO_3$ thin films deposited by radio-frequency magnetron sputtering at various substrate temperatures. *Journal of Applied Physics* **2006,** 99, 033515 - 03315-5.

6. Palik, E. D., *Handbook of Optical Constants of Solids II*. Academic Press, Inc.: 1991.

7. Jian-Hua, M.; Xiang-Jian, M.; Tie, L.; Shi-Jian, L.; Xiao-Dong, Z.; Jing-Lan, S.; Jun-Hao, C., Structural and electrical properties of SrTiO<SUB>3 thin films as insulator of metal-ferroelectric-insulator-semiconductor (MFIS) structures. *Chinese Physics* **2005,** 14, 2352-2359.

8. SCI, *FilmTek (TM) 3000SE Operations Manual*. Scientific Computing International: 2006.

9. Yu, P. Y.; Cardona, M., *Fundamentals of Semiconductors*. Springer, Berlin: 1996.

10. Zollner, S.; Demkov, A. A.; Liu, R.; Fejes, P. L.; Gregory, R. B.; Alluri, P.; Curless, J. A.; Yu, Z.; Ramdani, J.; Droopad, R.; Tiwald, T. E.; Hilfiker, J. N.; Woolam, J. A., Optical properties of bulk and thin-film $SrTiO_3$ on Si and Pt. *J. Vac. Sci. Technol. B* **2000,** 18, (4), 2242 - 2254.

11. Deng, Y.; Du, Y. L.; Zhang, M. S.; Han, J. H.; Yin, Z., Nonlinear optical properties in $SrTiO_3$ thin films by pulsed laser deposition. *Solid State Communications* **2005,** 135, (4), 221-225.

12. Gaidi, M.; Stafford, L.; Amassian, A.; Chaker, M.; Margot, J.; Martinu, L.; Kulishov, M., Influence of the microstructure on the optical characteristics of $SrTiO_3$ thin films. *Journal of Materials Research* **2005,** 20, 68 - 74.

13. Zollner, S.; Demkov, A. A.; Liu, R.; Curless, J. A.; Yu, Z.; Ramdani, J.; Droopad, R., Optical Properties of Thin Film $SrTiO_3$ on Si Grown by MBE. *Material Research*

Society Symposium Proceedings - Recent Developments in Oxide and Metal Epitaxy: Theory and Experiment **2000,** 619, 161-171.

CHAPTER 6 REFERENCES

1. (a) Daniel, M. C.; Astruc, D. *Chem. Re*V. **2004**, *104*, 293. (b) Rosi, N. L.; Mirkin, C. A. *Chem. Re*V. **2005**, *105*, 1547. (c) Penn, S. G.; He, L.; Natan, M. J. *Curr. Opin. Chem. Biol.* **2003**, *7*, 609. (d) Katz, E.; Willner, I. *Angew. Chem. Int. Ed.* **2004**, *43*, 6042. (e) Haes, A. J.; Stuart, D. A.; Nie, S. M.; Van, Duyne, R. P. *J. Fluoresc.* **2004**, *14*, 355. (f) Nicewarner-Pena, S. R.; Freeman, R. G.; Reiss, B. D.; He, L.; Pena, D. J.; Walton, I. D.; Cromer, R.; Keating, C. D.; Natan, M. J. *Science* **2001**, *294*, 137.

2. (a) Han, L.; Maye, M. M.; Leibowitz, F. L.; Ly, N. K.; Zhong, C. J. *J. Mater. Chem.* **2001**, *11*, 1258. (b) Luo, J.; Jones, V. W.; Han, L.; Maye, M. M.; Kariuki, N.; Zhong, C. J. *J. Phys. Chem.* **2004**, *108*, 9669. (c) Han, L.; Luo, J.; Kariuki, N.; Maye, M. M.; Jones, V. W.; Zhong, C. J. *Chem. Mater.* **2003**, *15*, 29.

3. (a) Maye, M. M.; Zheng, W. X.; Leibowitz, F. L.; Ly, N. K.; Zhong, C. J. *Langmuir* **2000**, *16*, 490. (b) Maye, M. M.; Zhong, C. J. *J. Mater. Chem.* **2000**, *10*, 1895. (c) Schadt, M. J.; Cheung, W.; Luo, J.; Zhong, C. J. *Chem. Mater.* **2006**, *18*, 5147.

4. (a) Leibowitz, F. L.; Zheng, W. X.; Maye, M. M.; Zhong, C. J. *Anal. Chem.* **1999**, *71*, 5076. (b) Kariuki, N. N.; Luo, J.; Hassan, S. A.; Lim, I.-Im S.; Wang, L. Y.; Zhong, C. J. *Chem. Mater.* **2006**, *18*, 123.

5. (a) Keating, C. D.; Musick, M. D.; Lyon, L. A.; Brown, K. R.; Baker, B. E.; Pena, D. J.; Feldheim, D. L.; Mallouk, T. E.; Natan, M. J. *ACS Symp. Ser.* **1997**, *679*, 7. (b) Musick, M. D.; Keating, C. D.; Lyon, L. A.; Botsko, S. L.; Pena, D. J.; Holliway, W. D.; McEvoy, T. M.; Richardson, J. N.; Natan, M. J. *Chem. Mater.* **2000**, *12*, 2869. (c) Mulvaney, S. P.; He, L.; Natan, M. J.; Keating, C. D. *J. Raman Spectrosc.* **2003**, *34*, 163.

6. Andres, R. P.; Bielefeld, J. D.; Henderson, J. I.; Janes, D. B.; Kolagunta, V. R.; Kubiak, C. P.; Mahoney, W. J.; Osifchin, R. G. *Science* **1996**, *273*, 1690.

7. (a) Brust, M.; Bethell, D.; Kiely, C. J.; Schiffrin, D. J. *Langmuir* **1998**, *14*, 5425.(b) Brust, M.; Bethell, D.; Schiffrin, D. J.; Kiely, C. J. *Adv. Mater.* **1995**, *7*, 795. (c)

Bethell, D.; Brust, M.; Schiffrin, D. J.; Kiely, C. *J. Electroanal. Chem.* **1996**, *409*, 137. (d) Brust, M.; Kiely, C. J.; Bethell, D.; Schiffrin, D. J. *J. Am. Chem. Soc*. **1998**, *120*, 12367.(e) Baum, T.; Bethell, D.; Brust, M.; Schiffrin, D. J. *Langmuir* **1999**, *15*, 866. (f) Horswell, S. L.; O'Neil, I. A.; Schiffrin, D. J. *J. Phys. Chem. B*. **2001**, *105*, 941. (g) Gittins, D. I.; Bethell, D.; Schiffrin, D. J.; Nichols, R. J. *Nature* **2000**, *408*, 67.

8. (a) Zamborini, F. P.; Hicks, J. F.; Murray, R. W. *J. Am. Chem. Soc.* **2000**, *122*, 4514. (b) Templeton, A. C.; Zamborini, F. P.; Wuelfing, W. P.; Murray, R. W. *Langmuir* **2000**, *16*, 6682. (c) Ibanez, F. J.; Gowrishetty, U.; Crain, M. M.; Walsh, K. M.; Zamborini, F. P. *Anal. Chem.* **2006**, *78*, 753. (d) Leopold, M. C.; Donkers, R. L.; Georganopoulou, D.; Fisher, M.; Zamborini, F. P.; Murray, R. W. *Faraday Discuss.* **2004**, *125*, 63.

9. Krasteva, N.; Fogel, Y.; Bauer, R. E.; Muellen, K.; Joseph, Y.; Matsuzawa, N.; Yasuda, A.; Vossmeyer, T. *Ad*V. *Funct. Mater*. **2007**, *17*, 881.

10. (a) Han, L.; Daniel, D. R.; Maye, M. M.; Zhong, C. J. *Anal. Chem.* **2001**, *73*, 4441. (b) Wang, L. Y.; Kariuki, N. N.; Schadt, M.; Mott, D.; Luo, J.; Zhong, C. J.; Shi, X. J.; Zhang, C.; Hao, W. B.; Lu, S.; Kim, N.; Wang, J.-Q. *Sensors* **2006**, *6*, 667. (c) Wang, L. Y.; Shi, X.; Kariuki, N. N.; Schadt, M.; Wang, G. R.; Rendeng, Q.; Choi, J.; Luo, J.; Lu, S.; Zhong, C. J. *J. Am. Chem. Soc.* **2007**, *129*, 2161.

11. Hostetler, M. J.; Templeton, A. C.; Murray, R. W. *Langmuir* **1999**, *15*, 3782.

12. Abeles, B.; Cheng, P.; Coutts, M. D.; Arie, Y. *Ad*V. *Phys.* **1975**, *24*, 407.

13. (a) Mie, G. *Ann. Phys.* **1908**, *25*, 377. (b) Link, S.; El-Sayed, M. A. *Int. Rev. Phys. Chem.* **2000**, *19*, 409. (c) Wang, H.; Brandl, D. W.; Nordlander, P.; Halas, N. J. *Acc. Chem. Res.* **2007**, *40*, 53.

14. Kelly, K. L.; Coronado, E.; Zhao, L. L.; Schatz, G. C. *J. Phys. Chem. B* **2003**, *107*, 668.

15. (a) Mirkin, C. A.; Letsinger, R. L.; Mucic, R. C.; Storhoff, J. J. *Nature* **1996**, *382*, 607. (b) Elghanian, R.; Storhoff, J. J.; Mucic, R. C.; Letsinger, R. L.; Mirkin, C. A. *Science* **1997**, *277*, 1078. (c) Rosi, N. L.; Giljohann, D. A.; Thaxton, C. S.; Lytton-

Jean, A. K. R.; Han, M. S.; Mirkin, C. *Science* **2006**, *312*, 1027. (d) Stoeva, S. I.; Lee, J. S.; Thaxton, C. S.; Mirkin, C. A. *Angew. Chem. Int. Ed.* **2006**, *45*, 3303.

16. (a) Dillenback, L. M.; Goodrich, G. P.; Keating, C. D. *Nano Lett.* **2006**, *6*, 16. (b) He, L.; Smith, E. A.; Natan, M. J.; Keating, C. D. *J. Phys. Chem. B* **2004**, *108*, 10973.

17. Wang, G. R.; Wang, L. Y.; Rendeng, Q.; Wang, J.; Luo, J.; Zhong, C. J. *J. Mater. Chem.* **2007**, *17*, 457.

18. Papavassiliou, G. C. *Prog. Solid State Chem.* **1979**, *12*, 185.

19. Kim, S. H.; Ock, K. S.; Im, J. H.; Kim, J. H.; Koh, K. N.; Kang, S. W. *Dyes Pigments* **2000**, *46*, 55.

20. Alejandro-Arellano, M.; Ung, T.; Blanco, A .; Mulvaney, P.; Liz-Marzan L. M. *Pure Appl. Chem.* **2000**,*72*, 257.

21. Jensen, T.; Kelly, L.; Lazarides, A.; Schatz, G. C. *J. Cluster Sci.* **1999**, *10*, 295.

22. Yang, K.; Fan, H. Y.; Malloy, K. J.; Brinker, C. J.; Sigmon, T. W. *Thin Solid Films* **2005**, *491*, 38.

23. Kooij, E. S.; Wormeester, H.; Brouwer, E. A. M.; van Vroonhoven, E.; van Silfhout, A.; Poelsema, B. *Langmuir* **2002**, *18*, 4401.

24. Palik, E. D. *Handbook of Optical Constants of Solids*; Academic Press: New York, 1985; p 294.